NTNU
Norwegian University of
Science and Technology

Small-signal modelling and stability analysis of a traditional generation unit and a virtual synchronous machine in grid-connected operation

Oscar Saborio Romano

Wind Energy
Submission date: October 2015
Supervisor: Elisabetta Tedeschi, ELKRAFT
Co-supervisor: Jon Are Suul, ELKRAFT
Pavol Bauer, TU Delft

Norwegian University of Science and Technology
Department of Electric Power Engineering

Master of Science Thesis

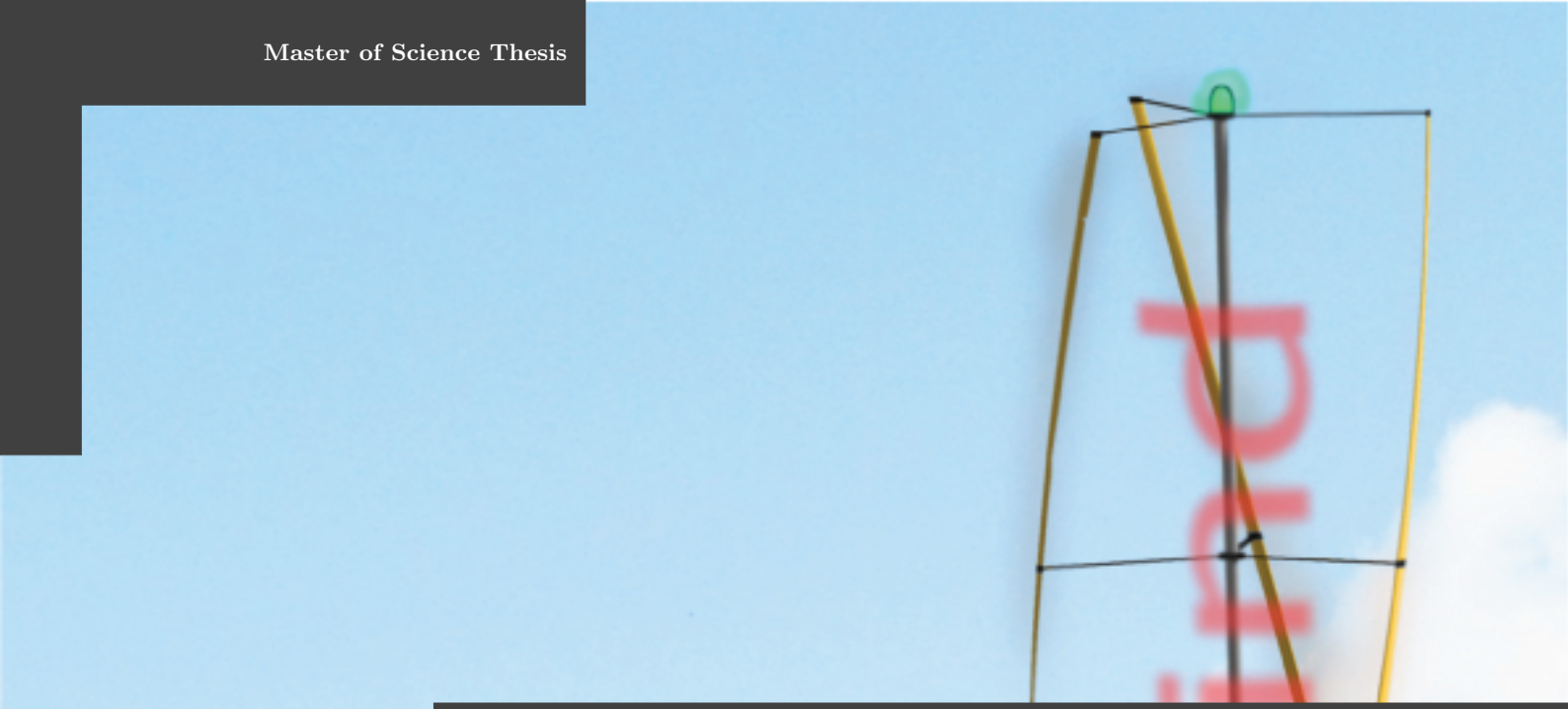

Small-signal modelling and stability analysis of a traditional generation unit and a virtual synchronous machine in grid-connected operation

Oscar Saborío-Romano

26th October, 2015

European Wind Energy Master - EWEM - Electric Power Systems Track

Small-signal modelling and stability analysis of a traditional generation unit and a virtual synchronous machine in grid-connected operation

Master of Science Thesis

For obtaining the degree of Master of Science in Electrical Engineering at Delft University of Technology and in Technology-Wind Energy at Norwegian University of Science and Technology.

Oscar Saborío-Romano

26th October, 2015

European Wind Energy Master - EWEM
Norwegian University of Science and Technology
Delft University of Technology

European Wind Energy Master - EWEM
Electric Power Systems Track

The undersigned hereby certify that they have read and recommend to the European Wind Energy Master - EWEM for acceptance a thesis entitled **"Small-signal modelling and stability analysis of a traditional generation unit and a virtual synchronous machine in grid-connected operation"** by **Oscar Saborío-Romano** in partial fulfillment of the requirements for the degree of **Master of Science**.

Dated: 26th October, 2015

Supervisor:

Elisabetta Tedeschi, PhD
Norwegian University of Science and Technology

Co-supervisor:

Jon Are Suul, PhD
Norwegian University of Science and Technology

Co-supervisor:

Pavol Bauer, PhD
Delft University of Technology

Summary

The virtual synchronous machine (VSM) concept has emerged as an approach to provide flexible distributed control of power electronic converters interfacing distributed energy resources with the grid. It supports power system operation by providing ancillary services, and facilitates a seamless transition between grid-connected and islanded operation. In this work, previous small-signal modelling and analysis carried out for a VSM implementation has been adapted and expanded to include a synchronous machine (SM) with a control scheme similar to those of traditional generation units and to the one used in the VSM implementation.

A nonlinear state-space analytical model has been developed for a traditional power generation unit in grid-connected mode (SM system). The model allows the study of the SM system in similar conditions/context as the grid-connected VSM implementation (VSM system), and facilitates their comparison. Moreover, it can represent the most relevant dynamic characteristics of a round or salient-pole rotor SM, including the amortisseur circuits or the representation of the corresponding damping torque in the swing equation of a reduced-order version of the model. The developed model has been linearised analytically, to obtain the respective small-signal model.

The eigenvalue analysis of the modelled systems has indicated that most of the SM system eigenvalues (modes) are slower or not as well damped as the VSM system ones. Moreover, most SM system modes have shown to be relatively fixed and determined mainly by non-tunable parameters. The modelled exciter has presented little capability of increasing the damping of oscillations, and its integral gain, $k_{i,ex}$, has demonstrated to be the tunable parameter that can most easily cause instability in the SM system. The location of the 4 slowest and least damped SM system eigenvalues has shown to be limited by non-tunable parameters, indicating that the performance or robustness of such system cannot be significantly improved. A trade-off has been observed in the placement of the VSM system critical modes: increasing the virtual inductance, l_v, improves the damping of oscillations, while making the system response slower. However, parametric sweep analysis has indicated that a good compromise between performance and robustness could be achieved by decreasing l_v and increasing the phase lock loop proportional gain, $k_{p,PLL}$.

Acknowledgements

I would like to extend my gratitude to Elisabetta Tedeschi and Jon Are Suul for their guidance, comments and support throughout this project. I would also like to thank my parents and Costa Rica's CONAPE, MICITT and CONICIT for their support throughout my studies.

Trondheim, Norway
26^{th} October, 2015

Oscar Saborío-Romano

Contents

List of Figures

List of Tables

Nomenclature

$\mathbf{A}_{SM}$	SM small-signal state-space model state (system, dynamic) matrix
$\mathbf{A}_{SMg}$	SMg small-signal state-space model state (system, dynamic) matrix
$\mathbf{A}_{VSM}$	VSM small-signal state-space model state (system, dynamic) matrix
AC	alternating current(s)
APC	active power control (controller)
AVR	automatic voltage regulator
$\mathbf{B}_{SM}$	SM small-signal state-space model input matrix
$\mathbf{B}_{SMg}$	SMg small-signal state-space model input matrix
$\mathbf{B}_{VSM}$	VSM small-signal state-space model input matrix
C_f	VSM filter capacitance
c_f	VSM pu filter capacitance
C_{mg}	SMg coupling capacitance
c_{mg}	SMg pu coupling capacitance
CC	current control (controller, controllers)
CSV	complex space vector
d-axis	direct axis
DC	direct current(s)
DER	distributed energy resource(s)
DG	distributed (energy) generation
DR	demand response
DS	distributed (energy) storage
$\delta\omega_{PLL}(t)$	VSM pu PLL angular speed deviation

$\delta\omega_{SM}(t)$	SM pu rotor angular speed deviation
$\delta\omega_{VSM}(t)$	VSM pu virtual rotor angular speed deviation
$\delta\theta_{PLL}(t)$	VSM PLL phase (angle) difference (displacement)
$\delta\theta_{SM}(t)$	SM rotor (phase) angle difference (displacement)
$\delta\theta_{VSM}(t)$	VSM virtual internal voltage phase (angle) difference (displacement)
$\mathbf{\Delta u}_{SM}(t)$	SM small-signal state-space model input vector
$\mathbf{\Delta u}_{SMg}(t)$	SMg small-signal state-space model input vector
$\mathbf{\Delta u}_{VSM}(t)$	VSM small-signal state-space model input vector
$\mathbf{\Delta x}_{SM}(t)$	SM small-signal state-space model state vector
$\mathbf{\Delta x}_{SMg}(t)$	SMg small-signal state-space model state vector
$\mathbf{\Delta x}_{VSM}(t)$	VSM small-signal state-space model state vector
$\varepsilon_{PLL}(t)$	VSM pu PLL PI controller integrator state
$\boldsymbol{\gamma}(t)$	VSM pu CC PI controllers integrators states
$\mathbf{i}_{cv}(t)$	VSM pu filter inductors current CSV
$\mathbf{i}^{*}_{cv}(t)$	VSM pu VSC current CSV reference (VC output signals)
$i_{fd}(t)$	SM pu field circuit current
$i_{kd}(t)$	SM pu k-th d-axis amortisseur circuit current
$i_{kq}(t)$	SM pu k-th q-axis amortisseur circuit current
$\mathbf{i}_{o}(t)$	VSM pu CSV of the currents flowing from the PCC into the grid equivalent
$I_{o,SM}(t)$	SMg currents flowing from the PCC into the grid equivalent
$\mathbf{i}_{o,SM}(t)$	SMg pu CSV of the currents flowing from the PCC into the grid equivalent
$i_{SM}(t)$	SM pu armature currents
$\mathbf{i}_{SM}(t)$	SM pu armature current CSV
$\overline{\mathbf{i}_{SM}}(t)$	SM pu complex conjugate of the armature current CSV
$i_{SM,d}(t)$	SM pu armature currents d-axis component
$i_{SM,q}(t)$	SM pu armature currents q-axis component
k_{AD}	VSM active damping gain
k_{d}	VSM damping factor (coefficient)
$k_{d,SM}$	SM damping factor (coefficient)
k_{ffc}	VSM VC current feed-forward gain
k_{ffv}	VSM CC voltage feed-forward gain
k_{ic}	VSM CC PI controllers integral gain
$k_{i,ex}$	SM exciter/AVR PI controller integral gain
$k_{i,PLL}$	VSM PLL PI controller integral gain

k_{iv}	VSM VC PI controllers integral gain
k_{pc}	VSM CC PI controllers proportional gain
$k_{p,ex}$	SM exciter/AVR PI controller proportional gain
$k_{p,PLL}$	VSM PLL PI controller proportional gain
k_{pv}	VSM VC PI controllers proportional gain
k_q	VSM reactive power-voltage droop gain (constant)
$k_{q,SM}$	SM reactive power-voltage droop gain (constant)
k_ω	VSM active power-frequency droop gain (constant)
$k_{\omega,SM}$	SM active power-frequency droop gain (constant)
l_{ad}	SM pu armature d-axis (unsaturated) mutual inductance
l_{aq}	SM pu armature q-axis (unsaturated) mutual inductance
l_f	VSM pu filter inductors inductance
l_{fd}	SM pu field circuit (unsaturated) leakage inductance
l_{ffd}	SM pu field circuit (unsaturated) self-inductance
l_{fkd}	SM pu (unsaturated) mutual inductance between the field and k-th d-axis amortisseur circuits
l_g	VSM pu grid equivalent inductance
l_{kd}	SM pu k-th d-axis amortisseur circuit (unsaturated) leakage inductance
l_{kkd}	SM pu k-th d-axis amortisseur circuit (unsaturated) self-inductance
l_{kkq}	SM pu k-th q-axis amortisseur circuit (unsaturated) self-inductance
l_{kq}	SM pu k-th q-axis amortisseur circuit (unsaturated) leakage inductance
l_l	SM pu armature (unsaturated) leakage inductance
l_{mg}	SMg pu grid equivalent inductance
l_v	VSM pu virtual inductance
λ_i	i-th eigenvalue (mode)
$\mathbf{m}(t)$	VSM VSC modulation index (ratio) CSV
$\omega^*(t)$	VSM pu (external) angular frequency/speed reference (set-point)
ω_{AD}	VSM active damping low-pass filters cut-off angular frequency
ω_b	angular frequency/speed base value
ω_f	VSM reactive power measurement low-pass filter cut-off angular frequency
$\omega_{f,SM}$	SM reactive power measurement low-pass filter cut-off angular frequency
$\omega_g(t)$	pu grid angular frequency
ω_i	imaginary part of the i-th eigenvalue (mode)
$\omega_{LP,PLL}$	VSM PLL low-pass filters cut-off angular frequency

$\omega_{PLL}(t)$	VSM pu estimated grid angular frequency (PLL output signal)
$\omega_{SM}(t)$	SM pu rotor angular speed
$\omega^*_{SM}(t)$	SM pu (external) angular frequency/speed reference (set-point)
$\omega_{VSM}(t)$	VSM pu virtual rotor angular speed
$p(t)$	VSM pu active power (measurement)
$p^*(t)$	VSM pu (external) active power set-point (reference)
$p^{r^*}(t)$	VSM pu virtual mechanical input power (APC output signal)
$p_{m,SM}(t)$	SM pu mechanical input power
$p^*_{m,SM}(t)$	SM pu mechanical input power reference (APC output signal)
$p_{SM}(t)$	SM pu active power (measurement)
$p^*_{SM}(t)$	SM pu (external) active power set-point (reference)
PCC	point of common coupling
PI	proportional-integral (controller)
PLL	phase lock (phase-locked) loop
PSS	power system stabiliser
pu	per unit
PWM	pulse-width modulation
$\boldsymbol{\varphi}(t)$	VSM pu low-pass filtered $\mathbf{v}_o(t)$ measurement CSV
$\psi_d(t)$	SM pu armature flux linkages d-axis component
$\psi_{fd}(t)$	SM pu field circuit flux linkage
$\psi_{kd}(t)$	SM pu k-th d-axis amortisseur circuit flux linkage
$\psi_{kq}(t)$	SM pu k-th q-axis amortisseur circuit flux linkage
$\psi_q(t)$	SM pu armature flux linkages q-axis component
$q(t)$	VSM pu reactive power (measurement)
$q^*(t)$	VSM pu (external) reactive power set-point (reference)
$q_m(t)$	VSM pu low-pass filtered reactive power measurement
$q_{m,SM}(t)$	SM pu low-pass filtered reactive power measurement
$q_{SM}(t)$	SM pu reactive power (measurement)
$q^*_{SM}(t)$	SM pu (external) reactive power set-point (reference)
q-axis	quadrature axis
r_a	SM pu armature resistance
r_f	VSM pu filter inductors equivalent resistance
r_{fd}	SM pu field circuit resistance
r_g	VSM pu grid equivalent resistance

r_{kd}	SM pu k-th d-axis amortisseur circuit resistance
r_{kq}	SM pu k-th q-axis amortisseur circuit resistance
r_{mg}	SMg pu grid equivalent resistance
r_v	VSM pu virtual resistance
RES	renewable energy sources
RPC	reactive power control (controller)
RRF	rotating reference frame
S_{rated}	rated (apparent) power
SM	synchronous machine
SMg	SM system plus grid equivalent impedance
σ_i	real part of the i-th eigenvalue (mode)
t	time variable
T_a	VSM virtual inertia time constant (mechanical starting time)
T_{ex}	SM exciter time constant
T_{gt}	SM governor-turbine time constant
T_{SM}	SM inertia time constant (mechanical starting time)
$\tau_{e,SM}(t)$	SM pu electromagnetic (air-gap) torque
$\tau_{m,SM}(t)$	SM pu mechanical input torque
$\theta_{PLL}(t)$	VSM PLL phase angle
$\theta_{SM}(t)$	SM rotor (phase) angle
$\theta_{VSM}(t)$	VSM virtual internal voltage phase angle
$\mathbf{u}_{SM}(t)$	SM state-space model input vector
$\mathbf{u}_{SMg}(t)$	SMg state-space model input vector
$\mathbf{u}_{VSM}(t)$	SM state-space model input vector
UPS	uninterruptible power supply (systems)
$\hat{v}^*(t)$	VSM pu (external) voltage amplitude set-point (reference)
$\hat{v}^{r^*}(t)$	VSM pu virtual internal voltage amplitude reference (RPC output signal)
$\mathbf{v}^*_{AD}(t)$	VSM pu CC active damping term
$\mathbf{v}_{cv}(t)$	VSM pu VSC (output) voltage CSV
$\mathbf{v}^*_{cv}(t)$	VSM pu VSC (output) voltage CSV reference (CC output signals)
$v_{DC}(t)$	VSM pu measured DC link voltage
$v_{fd}(t)$	SM pu field circuit voltage
$v^*_{fd}(t)$	SM pu field circuit voltage reference (AVR output signal)
$V_g(t)$	grid voltages

$\hat{v}_g(t)$	pu grid voltage amplitude
$\mathbf{v}_g(t)$	pu grid voltage CSV
$\mathbf{v}_g^{SM}(t)$	pu grid voltage CSV in the SM RRF
$\mathbf{v}_g^{VSM}(t)$	pu grid voltage CSV in the VSM RRF
$\hat{v}_o(t)$	VSM pu PCC (filter capacitors) voltage amplitude
$\mathbf{v}_o(t)$	VSM pu PCC (filter capacitors) voltage CSV
$\mathbf{v}_o^*(t)$	VSM pu PCC (filter capacitors) voltage CSV reference
$\mathbf{v}_o^{PLL}(t)$	VSM pu PCC (filter capacitors) voltage CSV in the PLL RRF
$\mathbf{v}_o^{VSM}(t)$	VSM pu PCC (filter capacitors) voltage CSV in the VSM RRF
$\mathbf{v}_{PLL}(t)$	VSM pu filtered PCC voltage (PLL RRF) CSV
$v_{PLL,d}(t)$	VSM pu filtered PCC voltage (PLL RRF) CSV d-axis component
$v_{PLL,q}(t)$	VSM pu filtered PCC voltage (PLL RRF) CSV q-axis component
V_{rated}	rated voltage
$v_{SM}(t)$	SM pu armature (PCC) voltages
$\hat{v}_{SM}(t)$	SM pu armature (PCC) voltage amplitude
$\hat{v}_{SM}^*(t)$	SM pu (external) voltage amplitude set-point (reference)
$\hat{v}_{SM}^{r^*}(t)$	SM pu armature (PCC) voltage amplitude reference (RPC output signal)
$\mathbf{v}_{SM}(t)$	SM pu armature voltage CSV
$v_{SM,d}(t)$	SM pu armature (PCC) voltages d-axis component
$v_{SM,q}(t)$	SM pu armature (PCC) voltages q-axis component
VC	voltage control (controller, controllers)
VI	virtual impedance
VPP	virtual power plant
VSC	voltage source converter
VSM	virtual synchronous machine
$\mathbf{x}_{SM}(t)$	SM state-space model state vector
$\mathbf{x}_{SMg}(t)$	SMg state-space model state vector
$\mathbf{x}_{VSM}(t)$	VSM state-space model state vector
$\boldsymbol{\xi}(t)$	VSM pu VC PI controllers integrators states CSV
Z_f	VSM filter equivalent series impedance
Z_g	VSM grid equivalent impedance
Z_{mg}	SMg grid equivalent impedance
$\zeta(t)$	SM pu exciter/AVR PI controller integrator state

Chapter 1

Introduction

1.1 Motivation

Planning, development and operation of electric power systems is expected to face considerable challenges with the proliferation of distributed generation (DG) from intermittent renewable energy sources (RES), such as photovoltaics and wind [7]. As some traditional synchronous generators will be replaced by such generation, power electronic converters, commonly used in these applications to interface the grid, can be expected to have a more significant impact on large-scale power systems. Under such conditions, the decrease of the systems' physical inertia and its stabilising effects can become a problem [9]. However, the advantage of generation interfaced by power electronics is its controllability [38].

Traditional power generation units support power system operation in different ways. They provide damping of power oscillations through their large rotating inertias, primary frequency regulation through their governor's droop characteristic, and local control of voltage or reactive power flow through their excitation control. These are not intrinsic to conventional control of RES power electronics interfaces, which depend on the synchronisation to a stable grid frequency [7, 13]. However, an emerging approach to the control of power electronic converters has been the emulation of essential properties of traditional power generation units, in order to gain the equivalent functionality [1, 2, 5, 6, 9, 11, 14, 15, 16, 19, 26, 29, 31, 35, 37, 40, 41, 42]. In this approach, some of the proposed control structures have been explicitly conceived to replicate the dynamic response of a synchronous machine (SM) . Such schemes can be classified as *virtual synchronous machines* (VSMs) [13].

Most VSM control studies have introduced specific implementations. These have mainly been tested independently, from the control system point of view, by time-domain simulations and/or laboratory experiments. Detailed modelling and small-signal stability analysis of a particular VSM implementation were first included in the study presented

in [11], mainly for the purpose of tuning the power electronic converter control loops. Detailed models and small-signal stability analyses of VSM implementations also considering the primary active power-frequency control and the dynamics of the grid frequency detection have been presented in [12, 13]. However, the small-signal stability characteristics of a VSM implementation still need to be compared with those of a traditional generation unit.

1.2 Scope and Limitations

This work has focused on the comparison of the small-signal stability properties of a particular VSM implementation with those of a traditional generation unit with a SM.Component-level considerations e.g., design, sizing, manufacturing, detailed modelling and tuning, have been excluded, and only grid-connected operation has been considered at first. Fast changes in the grid frequency have been excluded from the modelling under the assumption that protections prevent them from happening. For simplicity, load dynamics have not been considered and balanced three-phase conditions have been assumed.

The SM stator windings have been assumed to be distributed sinusoidally along the airgap. Magnetic hysteresis and variations of the rotor inductances with rotor position caused by the stator slots have been neglected. Magnetic saturation effects have also been neglected, so that all circuits have been assumed to be linearly coupled (linear flux-current relationships) [24]. Damping of the rotor motion by mechanical losses has been neglected [30]. The estimation of the damping factor (coefficient) for the swing equation of the reduced-order SM model and its dependence on the machine loading have been excluded. For simplicity, the dynamics of the governor, turbine and exciter have been represented with simple models. The modelling of the exciter has included a simple model for the automatic voltage regulator (AVR), and the power system stabiliser (PSS) has been excluded.

In modelling the power electronic conversion, the switching frequency has been assumed to be high enough for the switching action not to affect the progression of the states [23]. Thus, the switching effects and any delay due to the implementation of the pulse-width modulation (PWM) have been neglected, and an ideal average model has been assumed [13]. Moreover, the PWM has been assumed to be done in the linear range. Limitations, controlled output saturations and anti-windup functions, required for the safe operation of the power electronic converter, have been excluded from the modelling under the assumption that they don't influence the control scheme dynamics in the normal operating range [13].

No application-specific constraints have been considered for the direct current (DC) side of the power electronic converter and, thus, modelling and control of the energy resource(s) on the DC side has been excluded. Furthermore, the power requested from the AC side has been assumed to be available at the DC side [13].

1.3 Research goals

1.3.1 Main goal

To study the small-signal stability characteristics of a traditional power generation unit with a SM and compare them with those of the reference VSM implementation.

1.3.2 Specific goals

- To create and implement routines and (nonlinear) dynamic models in MATLAB/ Simulink to simulate and analyse the behaviour of the reference VSM implementation in grid-connected mode (VSM system).
- To develop, following the conventions used in the modelling of the reference VSM implementation, a nonlinear state-space analytical model of a traditional power generation unit directly connected to the grid, with a general model of a SM and currents (instead of fluxes) as state variables, to be used as the reference SM implementation in grid-connected mode (SM system).
- To create routines and dynamic models in MATLAB/Simulink to simulate and analyse the behaviour of the SM system.
- To develop, for any set of inputs and parameter values and any operating (linearisation) point, a general small-signal model of the SM system by analytically/ symbolically linearising the corresponding nonlinear state-space model.
- To validate the small-signal models by comparing their dynamic responses to those of the corresponding (nonlinear) dynamic models.
- To derive, for any set of inputs and parameter values and any operating point, expressions for the solution of the SM system nonlinear model equations in steady-state conditions.
- To create and implement functions for calculating the steady-state conditions of the modelled systems.
- To derive expressions for the partial derivatives of the SM system small-signal model state matrix with respect to each of the system parameters.
- To develop and implement functions for analysing the small-signal stability characteristics of the modelled systems.
- To analyse and compare the small-signal stability characteristics of the modelled systems.

1.4 Problem description

Using linear techniques, small-signal analysis gives information about the power system dynamic characteristics, and helps in its design [24]. The system equations can be linear-

ised, making the right assumptions, enabling sensitivity information to be calculated and factors influencing the small-signal stability to be identified [25].

The nonlinear and linearised small-signal models of the reference VSM implementation have been studied and implemented, and the presented results have been reproduced.

A nonlinear state-space model has been developed for a grid-connected, traditional power generation unit with a SM and currents (instead of fluxes) as state variables, following the conventions used in the modelling of the reference VSM implementation e.g., the choice of per unit base values, nomenclature and Park transformation. A general SM model has been used, which can represent the most relevant dynamic characteristics of a round or salient-pole rotor SM, including the amortisseur circuits or the representation of the corresponding damping torque in the swing equation of a reduced-order version of the model. The developed analytical model has been linearised for any set of parameter values and any operating (linearisation) point, to obtain the corresponding small-signal model.

The linearised small-signal models have been validated by comparing their dynamic responses to those of the nonlinear models and verifying they accurately represent the investigated systems for small deviations around the linearisation points.

Expressions for the solution of the SM system nonlinear model equations in steady-state conditions have been derived for any set of inputs, parameter values and operating point. Functions have been created and implemented to calculate the steady-state conditions of the modelled systems by numerically solving and evaluating the corresponding expressions for the solution of the nonlinear equations in steady-state conditions.

To study the small-signal characteristics of the systems, the eigenvalues (modes) of the linearised small-signal models have been calculated, along with the corresponding eigenvectors. Using that information, participation (factors) analysis has been performed to investigate interactions between system states and modes. To determine which parameters strongly influence certain eigenvalues, the sensitivity of the modes to changes in system parameters has been studied, which has required calculating the partial derivatives of the state matrices with respect to each of the system parameters. The analyses have focused on the the slowest and least damped eigenvalues.

1.5 Methodology

To reach the set goals, functions and programs have been developed in the MATLAB programming language, and models have been created in the Simulink graphical block diagramming tool, within the MATLAB numerical computing integrated environment.

Programs have been developed to simulate and analyse the behaviour of the studied systems. The time-domain simulations have been carried out in Simulink, while the execution control, algebraic matrix manipulation and small-signal analysis (by linear techniques) have been performed in MATLAB.

In order to obtain general expressions for the SM system, the Maple computer algebra

system has been extensively used to carry out the necessary analytical/symbolic manipulation of the equations. This includes:

- developing the nonlinear state-space model,
- deriving expressions for the nonlinear equation system steady-state solution,
- linearising the model,
- differentiating the resulting small-signal model state matrix with respect to the system parameters,
- evaluating the generated expressions for verification and debugging purposes, and
- formating them for their implementation in MATLAB functions and for their presentation in this report.

Using the produced analytical expressions for the SM system, functions have been created in MATLAB to calculate, for a given set of system parameters and steady-state inputs:

- the steady-state conditions,
- the (linearised) small-signal model at the steady-state operating (linearisation) point,
- the eigenvalues and eigenvectors,
- their participation factors and
- their sensitivity to changes in the system parameters.

The implemented and developed models and functions have been used to analyse and compare the small-signal stability characteristics of the studied systems.

1.6 Report outline

In *Chapter 1, Introduction,* the thesis work has been introduced. The motivation, scope and limitations, research goals, problem description and methodology have been presented.

In *Chapter 2, Background,* concepts that are relevant to this work are presented, the current state of knowledge is reviewed, and the contribution of this work is highlighted.

In *Chapter 3, Modelling,* the investigated systems are described, and corresponding (nonlinear) mathematical models are presented for each of their elements, as a basis for developing the (linearised) state-space small-signal models.

In *Chapter 4, Simulation results,* a base case is defined, and simulation results are presented and discussed. These include: dynamic responses of the base case systems to changes in their inputs (from time-step simulations); base case eigenvalues, participation factors and parametric sensitivities; and eigenvalue traces for system inputs and parameters varying around the base case values.

In *Chapter 5, Conclusions and recommendations,* concluding remarks and recommendations for further work are made.

Chapter 2

Background

After decades of experience, traditional power system analysis is well established, with standard models for each of the relevant components and frequency ranges (time horizons). Such a well established analysis does not exist yet for systems with a significant influence from generation interfaced with power electronic converters [32], which are pertinent to this work. Because of the nature of such systems, the scope of this work lies in between traditional power system analysis and control of power electronic converters. In this chapter, concepts relevant to this work are presented, the current state of knowledge is reviewed and the contribution of this work is highlighted.

An electrical power system is a highly nonlinear high-order multivariable process. It operates in constantly changing conditions, and its dynamic response is affected by a broad range of devices with different characteristics and response rates. Due to its complexity and high dimensionality, it is necessary to make simplifying assumptions and to analyse specific problems using suitable degrees of detail in its representation and the right analytical techniques [25].

2.1 Traditional power systems

In traditional power systems, generation is provided by a rather small number of large power plants, which are connected to the transmission system. In a traditional power generation unit, a prime mover (usually a turbine or a combustion engine) converts the primary source of energy into mechanical energy. The prime mover drives a synchronous machine (SM), which transforms the mechanical energy into electrical energy. A *governor* (speed controller/governor) controls the power output or the speed, based on a given active power-frequency *droop* characteristic. An *exciter* provides the field (excitation) current, necessary to create the magnetic field inside the SM. An *automatic voltage regulator* (AVR) controls the field current and, in consequence, the SM terminal voltage [30].

The stability of a traditional power system is strongly affected by its controls, which are highly distributed in a hierarchical configuration. Controllers operate directly on individual elements like boilers, prime movers, excitation systems, power (electronic) converters and transformer tap changers. The controllers of closely linked elements are coordinated by plant controllers. System controllers supervise the plant controllers at system control centres, and pool-level controllers coordinate the system controllers at pool control centres [24].

Within the distributed control structure, traditional power generation units support traditional power system operation in different ways. They participate in the system damping via their inertia, contribute in the primary frequency regulation by means of their governor droop characteristics, and take part in the local control of voltage or reactive power flow through their excitation controls. Such features are not intrinsic to the conventional control of the renewable energy sources (RES) power electronics interfaces, which depend on the synchronisation to a stable grid frequency [13].

2.2 Power system stability

Power system stability refers to the capacity of an electric power system to recover operating equilibrium after undergoing a disturbance, with most of the system remaining intact. The initial operating conditions and the nature of the disturbance influence this ability [25].

Power systems undergo a great diversity of disturbances. Load variations take place constantly, acting as small disturbances, and power systems have to operate satisfactorily while adapting to such changing conditions. They must also come through large disturbances, such as the loss of a large generator or a short circuit in a transmission line. Such disturbances can result in structural changes caused by the isolation of faulted elements or deliberate disconnections to maintain the major part of the system in operation. Interconnected power systems can also be deliberately divided into independent systems called *islands* [25].

Simplifying assumptions are made to concentrate on the aspects determining the specific kinds of stability problems. Stability in traditional power systems has been consequently classified into various categories. This facilitates the identification of essential aspects that contribute to instability and the development of methods for enhancing stability [24, 25].

2.2.1 Swing equation

The rotational inertia equations are central to power system stability analysis. The equation of motion of a SM in per unit (pu), given by (2.1), describes the effect of an unbalance between the pu electromagnetic (air-gap) torque, $\tau_{e,SM}(t)$, and the pu mechanical input torque, $\tau_{m,SM}(t)$, in a SM, with t being the time in seconds, $\delta\theta_{SM}(t)$ the (phase) angle difference (displacement) in electrical radians between the rotor angular position and the reference (phase) angle in a rotating reference frame (RRF), $k_{d,SM}$ the damping factor

(coefficient) and T_{SM} the inertia time constant (mechanical starting time) in seconds [24].

$$T_{SM}\frac{\mathrm{d}^2}{\mathrm{d}t^2}\delta\theta_{SM}(t) = \tau_{m,SM}(t) - \tau_{e,SM}(t) - k_{d,SM}\frac{\mathrm{d}}{\mathrm{d}t}\delta\theta_{SM}(t)\ , \tag{2.1}$$

T_{SM} corresponds to the time it takes rated torque to accelerate the rotor from standstill to rated speed, directly related to the combined moment of inertia of the SM and the prime mover. (2.1) is known as the *swing equation*, as it describes the the rotor angle swings during disturbances. The term $k_{d,SM}\frac{\mathrm{d}}{\mathrm{d}t}\delta\theta_{SM}(t)$ is usually included to represent a component of damping torque, proportional the to the rotor angular speed deviation (difference), $\frac{\mathrm{d}}{\mathrm{d}t}\delta\theta_{SM}(t)$, not included in the calculation of $\tau_{e,SM}(t)$ [24].

2.2.2 Rotor angle stability

For SMs to be interconnected, the frequency of their stator voltages and currents has to be the same, and, since their rotors mechanical angular speed is synchronised to that angular frequency, the rotors of all interconnected SMs need to be in *synchronism*. The stability category concerned with the capacity of the interconnected SMs of a power system to stay in synchronism after undergoing a disturbance is called *rotor angle stability*. Such ability is determined by the capacity of each SM to sustain or regain equilibrium between $\tau_{m,SM}(t)$ and $\tau_{e,SM}(t) + k_{d,SM}\frac{\mathrm{d}}{\mathrm{d}t}\delta\theta_{SM}(t)$ [24, 25].

That operating equilibrium is disrupted when the power system undergoes a disturbance, which causes the acceleration or deceleration of the rotors. When a SM spins more quickly than another one, its rotor $\delta\theta_{SM}(t)$ increases with respect to that of the slower SM. The increased relative $\delta\theta_{SM}(t)$ transfers part of the output power (load) from the slower SM to the faster one, as a result of the highly nonlinear active power-angle relationship. The consequently higher term $\tau_{e,SM}(t) + k_{d,SM}\frac{\mathrm{d}}{\mathrm{d}t}\delta\theta_{SM}(t)$ reduces the faster rotor $\frac{\mathrm{d}}{\mathrm{d}t}\delta\theta_{SM}(t)$ with respect to the slow one and thus their relative $\delta\theta_{SM}(t)$. However, due to the active power-angle relationship, an increase in the relative $\delta\theta_{SM}(t)$ past a critical point results in a decrease in the power transfer, so that the relative $\delta\theta_{SM}(t)$ increases further. If the kinetic energy from the corresponding $\frac{\mathrm{d}}{\mathrm{d}t}\delta\theta_{SM}(t)$ is subsequently not absorbed by the power system, instability arises [25].

The change in a SM electromagnetic torque, $\tau_{e,SM}(t) + k_{d,SM}\frac{\mathrm{d}}{\mathrm{d}t}\delta\theta_{SM}(t)$, resulting from a disturbance can be separated into a *synchronising torque* component, in phase with $\delta\theta_{SM}(t)$, and a *damping torque* component, in phase with $\frac{\mathrm{d}}{\mathrm{d}t}\delta\theta_{SM}(t)$. The magnitudes of both components in each SM determine system stability. *Oscillatory instability* is a consequence of insufficient damping torque, while *non-oscillatory (aperiodic) instability* is caused by a shortage of synchronising torque [25].

2.2.3 Voltage stability

The stability category concerned with the capacity of a power system to keep voltage levels within their limits at all buses after undergoing a disturbance is called *voltage stability*. Such ability is determined by the capacity to sustain or regain equilibrium between power (load) supply and demand. Corresponding instability arises as a gradual voltage drop or increase in some buses [25].

Voltage instability occurs often together with rotor angle stability. One can result in the other, and it can be difficult to differentiate them. The distinction has been made nevertheless in the traditional classification of power system stability with the purpose of comprehending the factors causing the problems, so that suitable design and operating methods can be elaborated [24].

2.2.4 Small-signal stability

This work has focused on the particular capacity of power systems to sustain synchronism and keep voltage levels within their limits at all buses under small perturbations, which is called *small-signal (small-disturbance) stability*. In the analysis of such problems, the system equations can be linearised making the right assumptions e.g., the small magnitude of all signal deviations from the steady-state operating point. This enables the use of linear techniques to calculate relevant sensitivity information, which can be used to determine factors affecting stability [25].

Rotor angle small-signal stability problems can be local or global. Local problems entail a small section of the power system. These are normally related to rotor angle oscillations of one power plant against the rest of the power system, which are called *local plant mode oscillations*. Global problems entail a group of SMs in one area swinging against another group in another area, and have widespread effects. The corresponding oscillations, called *inter-area mode oscillations*, have complex characteristics, very different from those of local plant mode oscillations [24, 25].

After a full small-signal (linear) state-space model of the power system is established, its eigenvalues (modes) can be calculated. These give the damping and frequency of the oscillatory terms, and the speed of the non-oscillatory ones, in the system (model) dynamic response. This analytical study enables further examination such as establishing the relationship between system parameters and stability. Participation (factors) analysis can then be performed to study interactions between system states and modes [4, 24, 32]. This analysis facilitates the investigation of the sensitivity of the eigenvalues to changes in system states. Moreover, the study of mode sensitivity to changes in system parameters contributes to determine which parameters strongly influence certain modes. In such studies, the influences on slow or poorly damped eigenvalues are of main interest [4, 30, 32].

2.3 Distributed energy resources

Environmental, technological and economic incentives are shifting paradigms in power systems. Traditional generation units exploiting centralised energy resources are giving way to smaller, more distributed energy resources (DER). DER include distributed storage (DS), demand response (DR) loads and distributed generation (DG), and encompass a wide range of emerging technologies, most of which have power electronics interfaces to the electrical power system. As opposed to traditional generation units, most DER are connected to distribution networks [22, 28, 39].

One of the major differences from traditional generation is that DG interfaced with power electronics cannot inherently supply the instantaneous power needs because of the absence of large rotors. Since most DG are inertia-less and respond slowly to control signals, load-tracking problems occur when operating without the presence of traditional generation. Thus, a system with groups of such DG designed to operate in that condition needs some sort of (distributed) energy storage to guarantee initial energy balance [28].

The technical challenges associated with the centralised control of a significant number of units is a fundamental problem for DER. In such a complex control system, the malfunction of a control, communication or software component could potentially cause a system collapse [28].

2.4 Microgrids

To avoid the need of redesign or re-engineering of the power system while enabling coordinated integration and high penetration of DER, system approaches have been taken to aggregate loads and DER in groups viewed as single controllable subsystems: *virtual power plants* (VPPs) [33, 36] or *microgrids* [28]. As opposed to that in microgrids, aggregation in VPPs can be virtual (software-based). Thus, while a microgrid can operate both in grid-connected and islanded mode, geographical limits often make the islanding of a whole VPP impossible [28, 39].

In ensuring the reliability of a microgrid, small-signal stability is of main interest. Small-signal stability analysis is well established for traditional power systems, but not so for microgrids based on power converters. For such microgrids, the influence of system parameters on certain oscillatory modes needs to be determined, specially for the poorly damped modes. Since the control and inertia time constants of traditional generation units are much greater than the network ones, the dynamics of the latter are usually excluded in the traditional power systems small-signal models. Most DER in microgrids are, however, interfaced with the main network by power converters with smaller time constants. Network dynamics can therefore influence the stability of such systems, and need to be included [32]. As a consequence of the relatively small size of the DER in a microgrid, most of the system dynamics in grid-connected operation are determined by the grid itself. However, such dynamics in islanded operation are dictated by the DER, their controls, the loads and the *micronetwork* itself [4, 32].

Microgrids can provide an electric service with higher power quality and reliability to the end customers, and dispatchable power and relief or deferral of grid upgrades to the power system operators [22, 27, 28]. By making use of local measurements only, they can respond independently to events. This may require, for example, a quick change in the control of the DG output power as it switches from a dispatched power mode to one in which it must control the island frequency and follow the load [28]. Although such operation is inherently feasible with traditional power generation units, it can be more complicated to realise with power converters designed to operate in large-scale power systems [13].

2.5 Virtual synchronous machines

However, an emerging approach to the control of DER power converters has been the emulation of fundamental characteristics of traditional power generation units in order to obtain the equivalent functionality. In this approach, different control schemes have been suggested for providing ancillary services such as emulation of rotating inertia, damping of oscillations and reactive power (voltage) control [1, 2, 5, 6, 9, 11, 14, 15, 16, 19, 26, 29, 31, 35, 37, 40, 41, 42]. Some of the proposed control structures have been explicitly conceived to replicate the dynamic response of a SM, and can be consequently classified as *virtual synchronous machines* (VSMs). VSMs based on the swing equation have been shown to be equivalent, under certain conditions, to the active power-frequency droop control schemes devised originally for uninterruptible power supply (UPS) systems and microgrids [9, 10], but VSM parameters can be more intuitive [13].

VSMs can help implementing flexible distributed (power) converter control structures, capable of both grid-connected and islanded operation, and capable of smoothly changing from one to the other. As opposed to conventional converter control schemes, VSMs can independently provide transient power sharing and frequency support as primary control actions, using only local information. These schemes can also track set-points given by a central controller in a hierarchical structure for optimising grid operation. Another advantage of VSMs is their conceptual simplicity, thanks to the intuitive interpretation of their responses by analogy with those of SMs. However, to represent the energy storage of the emulated rotating inertia, an adequate energy buffer is needed. Hence, the power converter current ratings and their direct current (DC) side configurations restrict the amount of virtual inertia that such schemes can provide [13].

Studies reviewing VSM implementations have been presented in [2, 9], including a classification framework proposed in [9]. These studies have stressed that some implementations do not fully capitalise on the VSM concept potential, as they depend on a phase lock (phase-locked) loop (PLL) for sensing the grid frequency, its derivative and the grid voltage phase angle, hence relying on grids with large rotating inertia. Other implementations use an internal (mathematical) SM model in the control system to directly generate the voltage references for the pulse-width modulation (PWM) of the signals driving the power electronic conversion [41]. Such direct open-loop control schemes do not allow, however, the explicit inclusion of the necessary functions to protect the converters. Such functions can be easily embedded in cascaded (closed-loop) control structures, in which the inertia emulation algorithm generates the set-point for a voltage control loop in cascade with a current control loop [8, 9, 13, 32, 34].

Most VSM control studies have introduced specific implementations. These have mainly been tested independently, from the control system point of view, by time-domain simulations and/or laboratory experiments. Detailed modelling and small-signal stability analysis of a specific implementation were first included in [11], mainly for the purpose of tuning the power electronic converter control loops. Detailed models and small-signal stability analyses of VSM implementations also considering the primary active power-frequency control and the dynamics of the grid frequency sensing have been presented in [12, 13]. The reference VSM implementation studied in this work has been proposed in [13], and is explained in Chapter 3.

In developing the necessary experience to establish reduced-order models for determined problems, the small-signal stability characteristics of systems with significant influence from generation interfaced with power electronic converters need to be further studied [32]. This work has aimed to contribute in that regard by adapting and expanding previous VSM small-signal modelling and analysis to include a SM with a control scheme similar to those of traditional generation units and to the one used in the reference VSM implementation. The comparison of their small-signal stability characteristics can help to asses the relevance and convenience of the developed and implemented models e.g., whether they provide the right degree of detail. Furthermore, applying linear analysis techniques can help tuning the corresponding controllers to obtain better performance and higher robustness of the studied systems.

Chapter 3

Modelling

In this chapter, the investigated systems are described, and corresponding (nonlinear) mathematical models are presented for each of their elements, as a basis for developing the (linearised) state-space small-signal models.

In a dual modelling approach, the reference virtual synchronous machine (VSM) implementation and a traditional generating unit with a synchronous machine (SM) have been modelled separately, and are thus introduced in a similar manner. The VSM system models are based on the ones presented in [13], while the SM system models have been developed following the same conventions e.g., the choice of per unit base values, nomenclature and Park transformation. To facilitate comparison, the SM control outer loops have been represented by models that are similar to those proposed in [13] for the VSM.

3.1 Modelling conventions

The modelling of the systems and the implementations of the control systems are based on per unit (pu) quantities, denoted by lower case letters, with the exception of time, t, expressed in seconds, angles, expressed in electrical radians, cut-off angular frequencies of the low-pass filters, expressed in electrical radians per second, and some base values, expressed in their corresponding physical values. The base values are defined from the apparent power ratings and the rated peak phase-to-neutral voltages. Physical values in the electrical circuits are represented by upper case letters [13, 24].

The modelling, analysis and control of the systems is implemented in rotating reference frames (RRFs). The transformations from the stationary reference frame into the RRFs are based on the amplitude-invariant Park transformation, with the quadrature (q) axis leading the direct (d) axis by 90°. Balanced three-phase conditions have been assumed, so no zero sequence components are included. The subindexes d and q denote the d-axis and

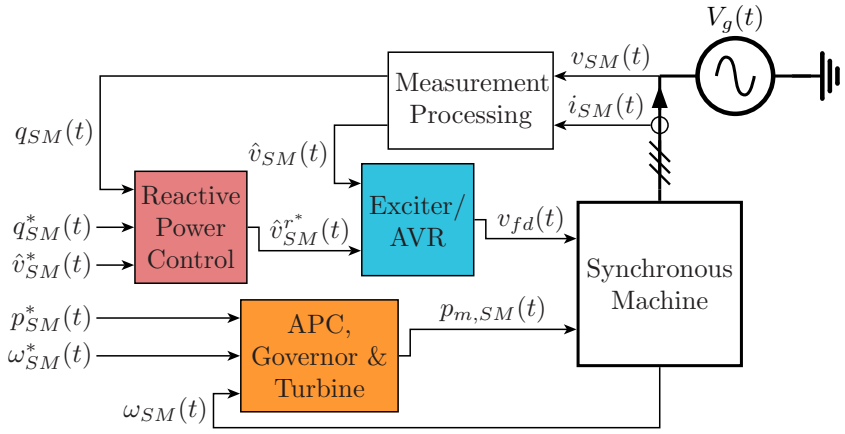

Figure 3.1: *Overview of the investigated system configuration and control structure for the synchronous machine*

q-axis components of a transformed variable, respectively. The magnitude of the current and voltage vectors is 1 pu at rated conditions [13, 24].

RRF equations are given, where possible, in complex space vector (CSV) notation as in

$$\mathbf{v}_{SM}(t) \doteq v_{SM,d}(t) + \mathrm{j}v_{SM,q}(t) \ . \tag{3.1}$$

Active and reactive powers can therefore be expressed on complex or scalar form as in (3.2), where $\overline{\mathbf{i}_{SM}}(t)$ denotes the complex conjugate of $\mathbf{i}_{SM}(t)$ [13].

$$\begin{aligned} p_{SM}(t) &= \mathrm{Re}\left[\mathbf{v}_{SM}(t)\overline{\mathbf{i}_{SM}}(t)\right] = v_{SM,d}(t)i_{SM,d}(t) + v_{SM,q}(t)i_{SM,q}(t) \\ q_{SM}(t) &= \mathrm{Im}\left[\mathbf{v}_{SM}(t)\overline{\mathbf{i}_{SM}}(t)\right] = -v_{SM,d}(t)i_{SM,q}(t) + v_{SM,q}(t)i_{SM,d}(t) \end{aligned} \tag{3.2}$$

3.2 Synchronous machine system

An overview of the investigated system configuration and control structure for the SM is shown in Figure 3.1.

In developing the mathematical model of the SM, further assumptions have been made. The stator windings have been assumed to be distributed sinusoidally along the air-gap. Magnetic hysteresis and variations of the rotor inductances with rotor position caused by the stator slots have been neglected. Magnetic saturation effects have also been neglected, so that all circuits have been assumed to be linearly coupled (linear flux-current relationships) [24]. Damping of the rotor motion by mechanical losses has been neglected [30].

The circuits used in the modelling of the SM are shown in Figure 3.2. The stator circuits comprise three-phase armature windings, a, b, c, carrying alternating currents (AC), while the rotor circuits consist of field winding and amortisseur circuits, $fd, 1d, 1q, 2q$. A direct current (DC) voltage source, $v_{fd}(t)$ is connected to the field winding [24], fd.

The currents in the amortisseur (solid rotor or damper windings) have, for modelling purposes, been assumed to flow in two sets of closed circuits: one whose flux is in line

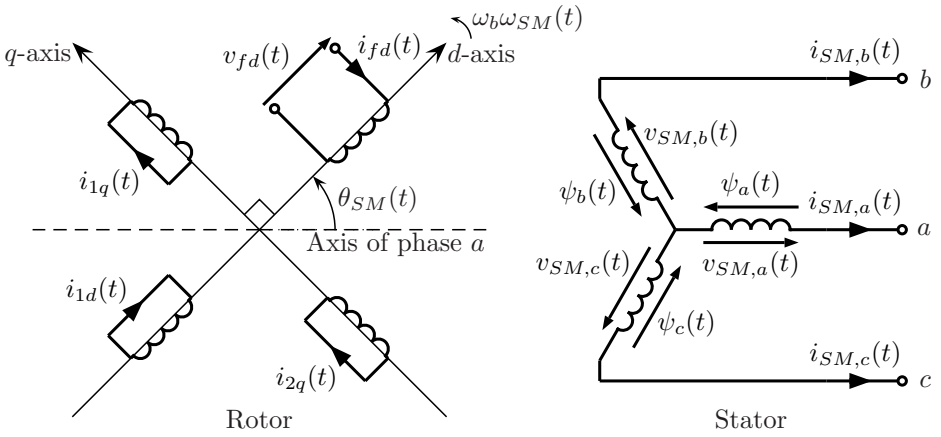

Figure 3.2: *Circuits used in the modelling of the synchronous machine*

with that of the field winding along the d-axis, $1d$, and the other whose flux is at a right angle, along the q-axis [24], $1q, 2q$.

The rotor (phase) angle, $\theta_{SM}(t)$, is the angle by which the d-axis leads the magnetic axis of phase a winding in the direction of rotation. As the rotor rotates with respect to the stator, $\theta_{SM}(t)$ increases continuously, and its relationship with the rotor angular speed, $\omega_{SM}(t)$, is given by (3.3), where ω_b is the angular speed/frequency base value in electrical radians per second and t is the time in seconds.

$$\theta_{SM}(t) = \omega_b\theta_{SM}(0) + \omega_b\int_0^t \omega_{SM}(t)\mathrm{d}t \tag{3.3}$$

The generator convention has been used for polarities: the direction of a stator winding current has been assumed to be positive when flowing out of the machine. The direction of the field and amortisseur currents has been assumed to be positive when flowing into the machine. By applying the (amplitude-invariant) Park transformation, with $\theta_{SM}(t)$ as the transformation angle, the equations associated with the stator circuits are expressed in the SM RRF: its rotor dq RRF. The equivalent circuits shown in Figure 3.3 can be used as a visual description of the machine model in the rotor dq RRF, featuring the currents as loop currents. The l_{ad}-base reciprocal pu system is used, so that the base current in any rotor circuit is defined as that which induces in each phase a pu voltage equal to the value of l_{ad} [24].

3.2.1 SM voltage equations

The stator voltage equations are given by (3.4) and (3.5), where r_a is the pu armature resistance, $v_{SM}(t), i_{SM}(t)$ are the pu armature voltages and currents, and $\psi_d(t), \psi_q(t)$ are the pu armature flux linkages d- and q-axis components, respectively.

$$v_{SM,d}(t) = \frac{1}{\omega_b}\frac{\mathrm{d}}{\mathrm{d}t}\psi_d(t) - \psi_q(t)\omega_{SM}(t) - r_a i_{SM,d}(t) \tag{3.4}$$

$$v_{SM,q}(t) = \frac{1}{\omega_b}\frac{\mathrm{d}}{\mathrm{d}t}\psi_q(t) + \psi_d(t)\omega_{SM}(t) - r_a i_{SM,q}(t) \tag{3.5}$$

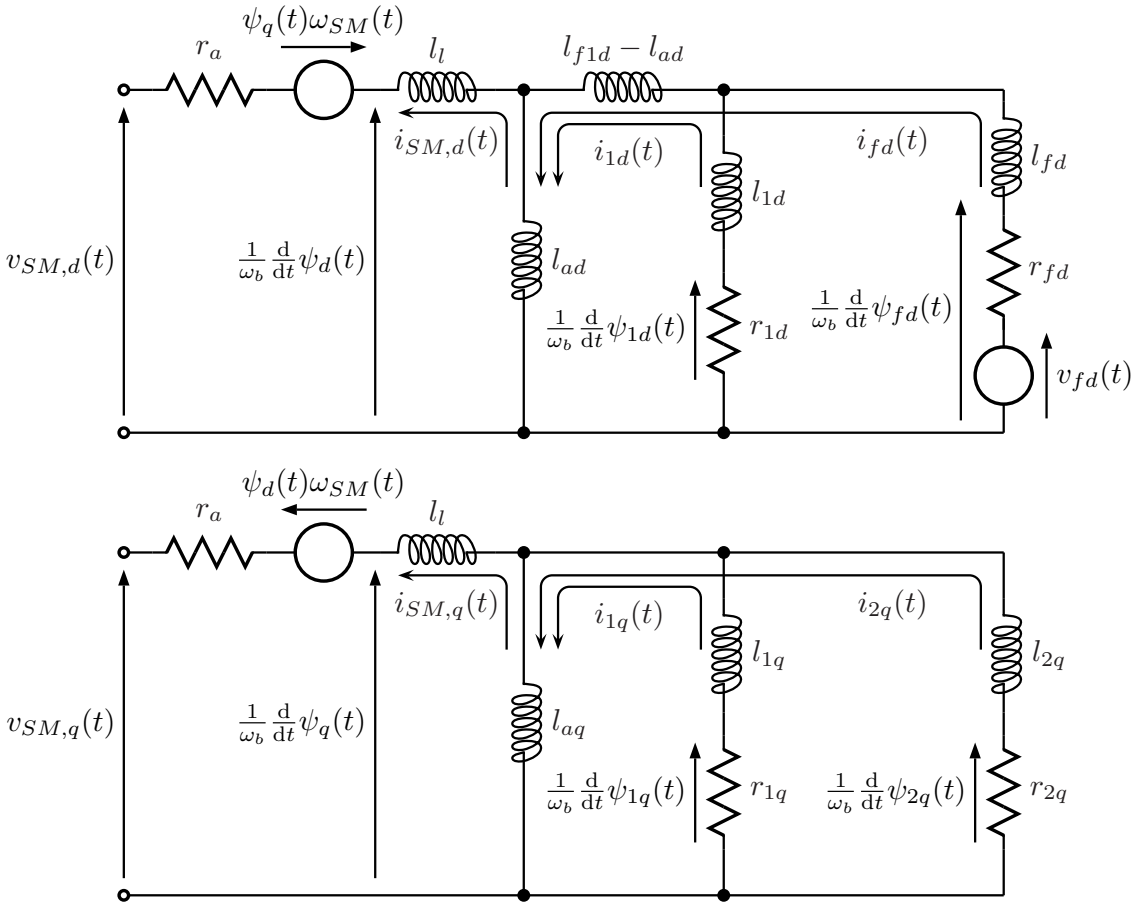

Figure 3.3: *SM pu d-axis (top) and q-axis (bottom) equivalent circuits*

The rotor voltage equations are given by (3.6)-(3.9), where $\psi_{fd}(t), \psi_{1d}(t), \psi_{1q}(t), \psi_{2q}(t)$ are the pu flux linkages, $r_{fd}, r_{1d}, r_{1q}, r_{2q}$ are the pu resistances and $i_{fd}(t), i_{1d}(t), i_{1q}(t), i_{2q}(t)$ are the pu currents of the field and amortisseur circuits, respectively.

$$v_{fd}(t) = \frac{1}{\omega_b}\frac{\mathrm{d}}{\mathrm{d}t}\psi_{fd}(t) + r_{fd}i_{fd}(t) \tag{3.6}$$

$$0 = \frac{1}{\omega_b}\frac{\mathrm{d}}{\mathrm{d}t}\psi_{1d}(t) + r_{1d}i_{1d}(t) \tag{3.7}$$

$$0 = \frac{1}{\omega_b}\frac{\mathrm{d}}{\mathrm{d}t}\psi_{1q}(t) + r_{1q}i_{1q}(t) \tag{3.8}$$

$$0 = \frac{1}{\omega_b}\frac{\mathrm{d}}{\mathrm{d}t}\psi_{2q}(t) + r_{2q}i_{2q}(t) \tag{3.9}$$

3.2.2 SM flux linkage equations

The stator flux linkage equations are given by (3.10) and (3.11), where l_l is the pu armature (unsaturated) leakage inductance, and l_{ad}, l_{aq} are the pu armature d- and q-axis (unsaturated) mutual inductances, respectively.

$$\psi_d(t) = -\left(l_{ad} + l_l\right) i_{SM,d}(t) + l_{ad}i_{fd}(t) + l_{ad}i_{1d}(t) \tag{3.10}$$

$$\psi_q(t) = -\left(l_{aq} + l_l\right) i_{SM,q}(t) + l_{aq}i_{1q}(t) + l_{aq}i_{2q}(t) \tag{3.11}$$

The rotor flux linkage equations are given by (3.12)-(3.15), where l_{f1d} is the pu (unsaturated) mutual inductance between the field and d-axis amortisseur circuits, l_{ffd},l_{11d},l_{11q}, l_{22q} are the pu (unsaturated) self-inductances of the field and the d- and q-axis amortisseur circuits (3.16)-(3.19), respectively, and l_{fd},l_{1d},l_{1q},l_{2q} are the corresponding pu (unsaturated) leakage inductances.

$$\psi_{fd}(t) = l_{ffd}i_{fd}(t) + l_{f1d}i_{1d}(t) - l_{ad}i_{SM,d}(t) \tag{3.12}$$

$$\psi_{1d}(t) = l_{f1d}i_{fd}(t) + l_{11d}i_{1d}(t) - l_{ad}i_{SM,d}(t) \tag{3.13}$$

$$\psi_{1q}(t) = l_{11q}i_{1q}(t) + l_{aq}i_{2q}(t) - l_{aq}i_{SM,q}(t) \tag{3.14}$$

$$\psi_{2q}(t) = l_{aq}i_{1q}(t) + l_{22q}i_{2q}(t) - l_{aq}i_{SM,q}(t) \tag{3.15}$$

$$l_{ffd} = l_{f1d} + l_{fd} \tag{3.16}$$

$$l_{11d} = l_{f1d} + l_{1d} \tag{3.17}$$

$$l_{11q} = l_{aq} + l_{1q} \tag{3.18}$$

$$l_{22q} = l_{aq} + l_{2q} \tag{3.19}$$

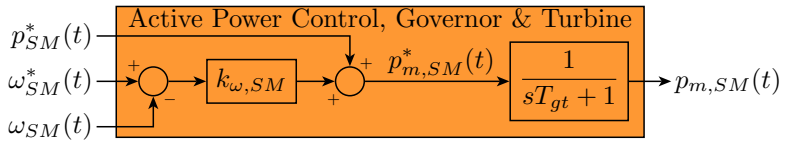

Figure 3.4: *Synchronous machine active power control, governor and turbine*

3.2.3 SM air-gap torque

The pu electromagnetic (air-gap) torque, $\tau_{e,SM}(t)$, is given by

$$\tau_{e,SM}(t) = \psi_d(t) i_{SM,q}(t) - \psi_q(t) i_{SM,d}(t) \tag{3.20}$$

3.2.4 SM equations of motion

The SM pu swing equation is given by (3.21), where $\delta\omega_{SM}(t)$ is the pu rotor angular speed deviation from the pu grid angular frequency (3.22), $\omega_g(t)$, $\tau_{m,SM}(t)$ is the pu mechanical input torque (3.23), $p_{m,SM}(t)$ is the pu mechanical input power, T_{SM} is the inertia time constant (mechanical starting time) and $k_{d,SM}$ is the damping factor (coefficient). As mentioned in Section 2.2.1, the term $k_{d,SM}\delta\omega_{SM}(t)$ includes a component of damping torque not accounted for in the calculation of $\tau_{e,SM}(t)$ [24]. This allows the modelling of the damping provided by the amortisseur circuits without explicitly considering them in the (reduced-order) model. Thus, when the amortisseur circuits are explicitly considered in the (general) model, the term is excluded e.g., by setting $k_{d,SM} = 0$.

$$\frac{\mathrm{d}}{\mathrm{d}t}\delta\omega_{SM}(t) = \frac{\tau_{m,SM}(t)}{T_{SM}} - \frac{\tau_{e,SM}(t)}{T_{SM}} - \frac{k_{d,SM}\delta\omega_{SM}(t)}{T_{SM}} \approx \frac{\mathrm{d}}{\mathrm{d}t}\omega_{SM}(t) \tag{3.21}$$

$$\delta\omega_{SM}(t) = \omega_{SM}(t) - \omega_g(t) \tag{3.22}$$

$$\tau_{m,SM}(t) = \frac{p_{m,SM}(t)}{\omega_{SM}(t)} \tag{3.23}$$

Expressions for the rotor (phase) angle difference (displacement), $\delta\theta_{SM}(t)$, and $\theta_{SM}(t)$ are given by (3.24) and (3.25), respectively.

$$\frac{\mathrm{d}}{\mathrm{d}t}\delta\theta_{SM}(t) = \omega_b\delta\omega_{SM}(t) = \omega_b\omega_{SM}(t) - \omega_b\omega_g(t) \tag{3.24}$$

$$\frac{\mathrm{d}}{\mathrm{d}t}\theta_{SM}(t) = \omega_b\omega_{SM}(t) = \omega_b\delta\omega_{SM}(t) + \omega_b\omega_g(t) \tag{3.25}$$

3.2.5 Active power control, governor and turbine

A block diagram portraying the models of the active power control (APC), (speed) governor and turbine is shown in Figure 3.4.

APC is provided by an active power-frequency droop (3.26) that models the steady-state characteristics of the governor [13], with $p^*_{m,SM}(t)$ being the APC output signal: the

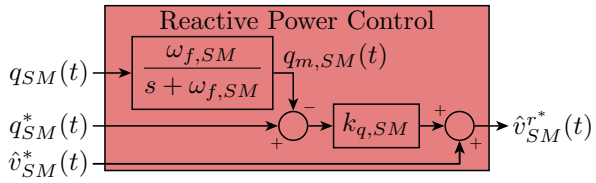

Figure 3.5: *Synchronous machine reactive power control*

pu mechanical input power reference, $p^*_{SM}(t)$ the pu (external) active power set-point (reference), $k_{\omega,SM}$ the active power-frequency droop gain (constant) and $\omega^*_{SM}(t)$ the pu (external) angular frequency/speed reference (set-point).

$$p^*_{m,SM}(t) = p^*_{SM}(t) - k_{\omega,SM}\left[\omega_{SM}(t) - \omega^*_{SM}(t)\right] \tag{3.26}$$

The dynamic characteristics of the governor and the turbine are modelled together as a first-order system (3.27), with time constant T_{gt} .

$$\frac{\mathrm{d}}{\mathrm{d}t}p_{m,SM}(t) = \frac{p^*_{m,SM}(t)}{T_{gt}} - \frac{p_{m,SM}(t)}{T_{gt}} \tag{3.27}$$

3.2.6 Reactive power control

The applied droop-based reactive power control (RPC) is similar to those commonly used in microgrid systems [13, 32, 34]. The corresponding block diagram is shown in Figure 3.5.

The RPC output signal: the pu armature voltage amplitude reference, $\hat{v}^{r^*}_{SM}(t)$, is calculated by (3.28), where $\hat{v}^*_{SM}(t)$ is the pu (external) voltage amplitude set-point (reference), $k_{q,SM}$ is the reactive power-voltage droop gain (constant), $q^*_{SM}(t)$ is the pu (external) reactive power set-point (reference) and $q_{m,SM}(t)$ is the pu filtered reactive power measurement. The state-space equation representing the applied first-order low-pass filter is given by (3.29), where $q_{SM}(t)$ is the pu reactive power measurement (3.30) and $\omega_{f,SM}$ is the filter cut-off angular frequency.

$$\hat{v}^{r^*}_{SM}(t) = \hat{v}^*_{SM}(t) + k_{q,SM}\left[q^*_{SM}(t) - q_{m,SM}(t)\right] \tag{3.28}$$

$$\frac{\mathrm{d}}{\mathrm{d}t}q_{m,SM}(t) = -\omega_{f,SM}q_{m,SM}(t) + \omega_{f,SM}q_{SM}(t) \tag{3.29}$$

$$q_{SM}(t) = -v_{SM,d}(t)i_{SM,q}(t) + v_{SM,q}(t)i_{SM,d}(t) \tag{3.30}$$

3.2.7 Exciter with automatic voltage regulator

A block diagram showing the model of the exciter with an automatic voltage regulator (AVR) is shown in Figure 3.6.

The AVR is modelled as a proportional-integral (PI) controller. Its reference, $\hat{v}^{r^*}_{SM}(t)$, is compared with the pu armature voltage amplitude, $\hat{v}_{SM}(t)$, to produce the AVR output signal: the pu field circuit voltage reference, $v^*_{fd}(t)$, given by (3.31), where $k_{p,ex}$ and

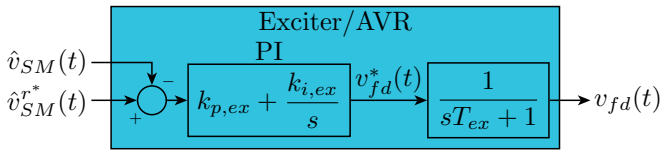

Figure 3.6: *Synchronous machine exciter with automatic voltage regulator*

$k_{i,ex}$ are the PI controller proportional and integral gains, respectively, and the state $\zeta(t)$ represents the integrator of the PI controller (3.32). Required controller anti-windup protection, output saturation, limiters or protective circuits are not included in the model, as they don't influence the dynamics of the control scheme within the normal operating range.

$$v^*_{fd}(t) = k_{p,ex}\left[\hat{v}^{r*}_{SM}(t) - \hat{v}_{SM}(t)\right] + k_{i,ex}\zeta(t) \tag{3.31}$$

$$\frac{\mathrm{d}}{\mathrm{d}t}\zeta(t) = \hat{v}^{r*}_{SM}(t) - \hat{v}_{SM}(t) \tag{3.32}$$

The dynamic characteristics of the exciter are modelled as a first-order system (3.33), with time constant T_{ex} .

$$\frac{\mathrm{d}}{\mathrm{d}t}v_{fd}(t) = \frac{v^*_{fd}(t)}{T_{ex}} - \frac{v_{fd}(t)}{T_{ex}} \tag{3.33}$$

3.2.8 Reference frame orientation

In steady state, the SM RRF rotates with the same angular speed as the grid voltage. Thus, the rotor (phase) angle, $\theta_{SM}(t)$, continuously increases, as shown in the vector diagram in Figure 3.7. The rotor (phase) angle difference (displacement), $\delta\theta_{SM}(t)$, represents the phase difference between the SM RRF and the rotating grid voltage vector, as shown also in Figure 3.7. Assuming the pu grid voltage amplitude, $\hat{v}_g(t)$, to be known, the pu grid voltage CSV in the SM RRF, $\mathbf{v}^{SM}_g(t)$, is then given by

$$\mathbf{v}^{SM}_g(t) = \hat{v}_g(t)\mathrm{e}^{-\mathrm{j}\delta\theta_{SM}(t)} \tag{3.34}$$

3.2.9 Nonlinear model

Neglecting the term $\frac{\mathrm{d}}{\mathrm{d}t}\omega_g(t)$, equations (3.4)-(3.34) have been reduced in Maple to a state-space model with 12 state variables and 6 input signals, with the state vector, $\mathbf{x}_{SM}(t)$, defined by (3.35), and the input vector, $\mathbf{u}_{SM}(\mathrm{t})$, defined by (3.36). Terms such as $\psi_d(t)i_{SM,q}(t)$ and $\psi_q(t)i_{SM,d}(t)$ in (3.23), $p_{m,SM}(t)/\omega_{SM}(t)$ in (3.23), $v_{SM,d}(t)i_{SM,q}(t)$ and $v_{SM,q}(t)i_{SM,d}(t)$ in (3.30) and $\hat{v}_g(t)\mathrm{e}^{-\mathrm{j}\delta\theta_{SM}(t)}$ in (3.34) make the model nonlinear. The resulting model equations are given in Appendix A.

$$\begin{aligned}\mathbf{x}_{SM}(t) \doteq [&i_{SM,d}(t)\ i_{SM,q}(t)\ i_{fd}(t)\ i_{1d}(t)\ i_{1q}(t)\ i_{2q}(t)\ \cdots \\ &\cdots\ \omega_{SM}(t)\ \delta\theta_{SM}(t)\ p_{m,SM}(t)\ q_{m,SM}(t)\ \zeta(t)\ v_{fd}(t)]^T\end{aligned} \tag{3.35}$$

$$\mathbf{u}_{SM}(t) \doteq [\hat{v}_g(t)\ p^*_{SM}(t)\ \hat{v}^*_{SM}(t)\ q^*_{SM}(t)\ \omega^*_{SM}(t)\ \omega_g(t)]^T \tag{3.36}$$

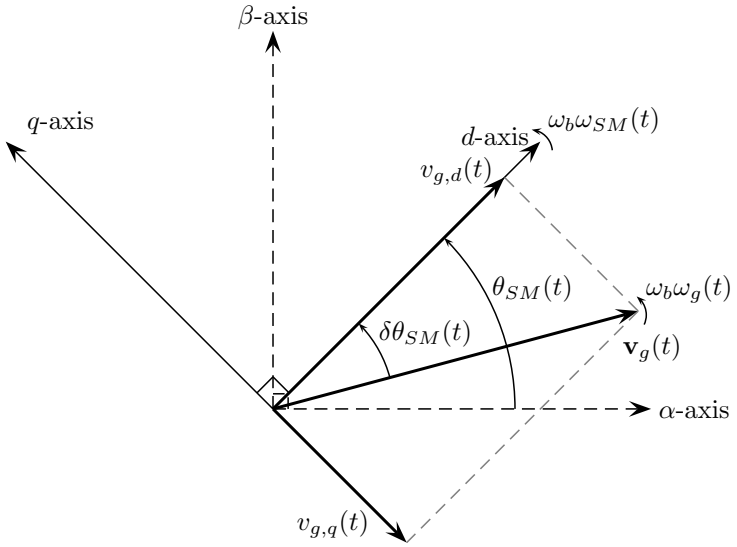

Figure 3.7: *Vector diagram defining the SM RRF and voltage CSV orientations*

3.2.10 Small-signal model

Classical stability assessment techniques based on eigenvalues are not directly applicable to the nonlinear state-space model. A linearised small-signal state-space model has therefore been derived in Maple, with the form given by (3.37), where the prefix Δ indicates small-signal deviations around the steady-state operating point [13, 24], $\mathbf{A}_{SM}$ is the state (system, dynamic) matrix and $\mathbf{B}_{SM}(t)$ is the input matrix. The resulting analytical expressions for the matrices are given in Appendix A.

$$\boldsymbol{\Delta}\dot{\mathbf{x}}_{SM}(t) \doteq \frac{\mathrm{d}}{\mathrm{d}t}\boldsymbol{\Delta}\mathbf{x}_{SM}(t) = \mathbf{A}_{SM}\boldsymbol{\Delta}\mathbf{x}_{SM}(t) + \mathbf{B}_{SM}\boldsymbol{\Delta}\mathbf{u}_{SM}(t) \tag{3.37}$$

3.3 SM system plus grid equivalent impedance

The SM system model has been modified, at a later stage, to include an equivalent of the grid impedance, as depicted in Figure 3.8. A capacitance has been added at the PCC to provide an independent state that allows to couple both state-space subsystems. The corresponding state-space equations in the SM RRF are given by (3.38) and (3.39), where c_{mg} is the pu coupling capacitance, $\mathbf{i}_{o,SM}(t)$ is the pu CSV of the currents flowing from the SM PCC into the grid equivalent, l_{mg} is the pu grid equivalent inductance and r_{mg} is the pu grid equivalent resistance.

$$\frac{\mathrm{d}}{\mathrm{d}t}\mathbf{v}_{SM}(t) = \frac{\omega_b}{c_{mg}}\mathbf{i}_{SM}(t) - \frac{\omega_b}{c_{mg}}\mathbf{i}_{o,SM}(t) - \mathrm{j}\omega_b\omega_g(t)\mathbf{v}_{SM}(t) \tag{3.38}$$

$$\frac{\mathrm{d}}{\mathrm{d}t}\mathbf{i}_{o,SM}(t) = \frac{\omega_b}{l_{mg}}\mathbf{v}_{SM}(t) - \frac{\omega_b}{l_{mg}}\mathbf{v}_g(t) - \left[\frac{r_{mg}\omega_b}{l_{mg}} + \mathrm{j}\omega_b\omega_g(t)\right]\mathbf{i}_{o,SM}(t) \tag{3.39}$$

Equations (3.4)-(3.34),(3.38),(3.39) have been consequently reduced in Maple to a state-space model with 16 state variables and 6 input signals, with the state vector, $\mathbf{x}_{SMg}(t)$,

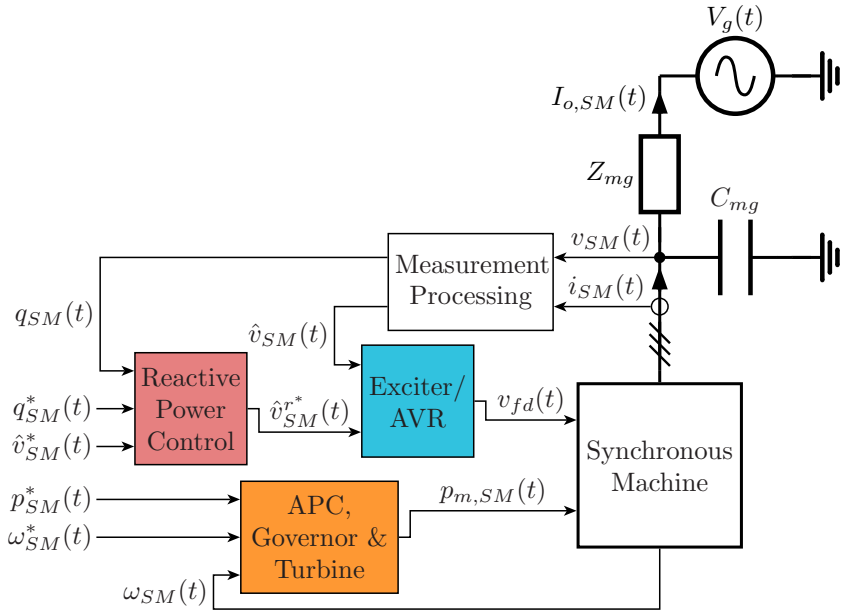

Figure 3.8: *Overview of the investigated system configuration and control structure for the synchronous machine plus grid equivalent impedance*

defined by (3.40), and the input vector, $\mathbf{u}_{SMg}(\mathrm{t})$, defined by (3.41). The resulting model equations are given in Appendix B.

$$\begin{aligned}\mathbf{x}_{SMg}(t) \doteq [&v_{SM,d}(t)\ v_{SM,q}(t)\ i_{o,SM,d}(t)\ i_{o,SM,q}(t)\ \cdots \\ &\cdots\ i_{SM,d}(t)\ i_{SM,q}(t)\ i_{fd}(t)\ i_{1d}(t)\ i_{1q}(t)\ i_{2q}(t)\ \cdots \\ &\cdots\ \omega_{SM}(t)\ \delta\theta_{SM}(t)\ p_{m,SM}(t)\ q_{m,SM}(t)\ \zeta(t)\ v_{fd}(t)]^T\end{aligned} \tag{3.40}$$

$$\mathbf{u}_{SMg}(t) \doteq [\hat{v}_g(t)\ \omega_g(t)\ p^*_{SM}(t)\ q^*_{SM}(t)\ \omega^*_{SM}(t)\ \hat{v}^*_{SM}(t)]^T \tag{3.41}$$

A linearised small-signal state-space model has also been derived in Maple, with the form given by (3.42), where the prefix Δ indicates small-signal deviations around the steady-state operating point, $\mathbf{A}_{SMg}$ is the state (system, dynamic) matrix and $\mathbf{B}_{SMg}(t)$ is the input matrix. The resulting analytical expressions for the matrices are given in Appendix B.

$$\boldsymbol{\Delta}\dot{\mathbf{x}}_{SMg}(t) \doteq \frac{\mathrm{d}}{\mathrm{d}t}\boldsymbol{\Delta}\mathbf{x}_{SMg}(t) = \mathbf{A}_{SMg}\boldsymbol{\Delta}\mathbf{x}_{SMg}(t) + \mathbf{B}_{SMg}\boldsymbol{\Delta}\mathbf{u}_{SMg}(t) \tag{3.42}$$

3.4 Virtual synchronous machine system

An overview of the investigated system configuration and control structure for the VSM is depicted in Figure 3.9, in which a voltage source converter (VSC) is connected to a grid through a LC filter. Positive values for active and reactive power flowing from the VSC into the grid result from the current directions indicated in Figure 3.9 [13].

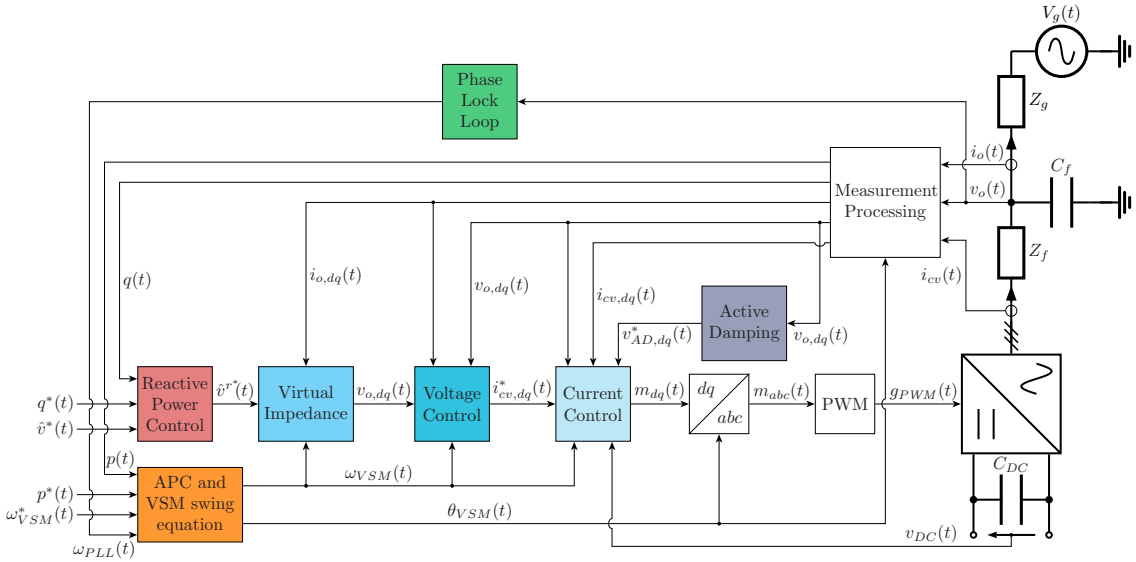

Figure 3.9: *Overview of the investigated system configuration and control structure for the virtual synchronous machine*

In modelling the VSC, the switching frequency has been assumed to be high enough for the switching action not to affect the progression of the states. Thus, the switching effects and any delay due to the implementation of the pulse-width modulation (PWM) have been neglected, and an ideal average model has been assumed [13, 23]. The PWM has been assumed to be done in the linear range. No application-specific constraints have been considered for the VSC DC side and, thus, modelling and control of the energy resource(s) on the DC side has been excluded. The AC side has been assumed to be effectively decoupled from any dynamics in the DC voltage, so that the dynamics on the AC side can be accurately represented without modelling the DC side. Furthermore, the power requested from the AC side has been assumed to be available at the DC side [13].

By applying the (amplitude-invariant) Park transformation, with the VSM virtual internal voltage phase angle, $\theta_{VSM}(t)$, as the transformation angle, the equations are expressed in the VSM RRF. As opposed to that of the SM RRF, the VSM RRF d-axis is thus aligned not to the axis of the virtual rotor field winding but to its corresponding virtual internal voltage, which leads the former by 90°. The VSM RRF is used for both control and modelling of the system. Thus, the electrical system model is also represented in this RRF.

As in Section 3.2.7, limitations, PI controller anti-windup protections or output saturations, required for the safe operation of the VSC, have been excluded from the modelling under the assumption that they don't influence the control scheme dynamics in the normal operating range [13].

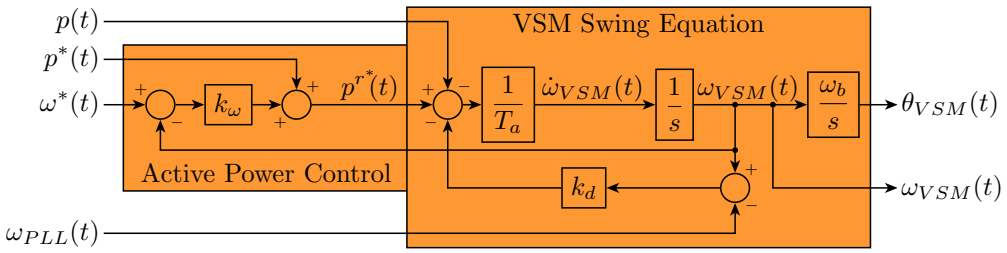

Figure 3.10: *Virtual synchronous machine swing equation and active power control*

3.4.1 Electrical system equations

According to Figure 3.9, the electrical system in the model comprises a set of filter inductors connected to the VSC and a shunt capacitor bank modelling the LC filter capacitance, at the point of common coupling (PCC) with (a Thévenin equivalent of) the grid. This incorporates the dynamic interaction between the VSC control system and the equivalent grid voltage in the model. Assuming an instantaneous average model of the VSC and neglecting the term $\frac{\mathrm{d}}{\mathrm{d}t}\omega_g(t)$, the electrical system state-space equations in the VSM RRF are given by (3.43)-(3.45) [3, 13, 32], where $\mathbf{i}_{cv}(t)$ is the pu filter inductors current CSV, l_f is the pu filter inductors inductance, $\mathbf{v}_{cv}(t)$ is the pu VSC output voltage CSV, $\mathbf{v}_o(t)$ is the pu PCC (filter capacitors) voltage CSV, r_f is the pu filter inductors equivalent resistance, c_f is the pu filter capacitance, $\mathbf{i}_o(t)$ is the pu CSV of the currents flowing from the VSM PCC into the grid equivalent, l_g is the pu grid equivalent inductance, r_g is the pu grid equivalent resistance and $\mathbf{v}_g(t)$ is the pu grid voltage CSV.

$$\frac{\mathrm{d}}{\mathrm{d}t}\mathbf{i}_{cv}(t) = \frac{\omega_b}{l_f}\mathbf{v}_{cv}(t) - \frac{\omega_b}{l_f}\mathbf{v}_o(t) - \left[\frac{r_f\omega_b}{l_f} + \mathrm{j}\omega_b\omega_g(t)\right]\mathbf{i}_{cv}(t) \tag{3.43}$$

$$\frac{\mathrm{d}}{\mathrm{d}t}\mathbf{v}_o(t) = \frac{\omega_b}{c_f}\mathbf{i}_{cv}(t) - \frac{\omega_b}{c_f}\mathbf{i}_o(t) - \mathrm{j}\omega_b\omega_g(t)\mathbf{v}_o(t) \tag{3.44}$$

$$\frac{\mathrm{d}}{\mathrm{d}t}\mathbf{i}_o(t) = \frac{\omega_b}{l_g}\mathbf{v}_o(t) - \frac{\omega_b}{l_g}\mathbf{v}_g(t) - \left[\frac{r_g\omega_b}{l_g} + \mathrm{j}\omega_b\omega_g(t)\right]\mathbf{i}_o(t) \tag{3.45}$$

3.4.2 Inertia emulation and active power control

The studied VSM implementation is based on the SM swing equation (3.21) representing its inertia and damping [9, 11, 13]. Block diagrams showing the implementation of the active power control (APC) and the VSM swing equation are shown in Figure 3.10, on the left and right, respectively.

The SM pu swing equation (3.21) is linearised with respect to the speed so that the inertia acceleration is determined by the power balance according to (3.46), where $\delta\omega_{VSM}(t)$ is the pu virtual rotor angular speed deviation from the pu grid angular frequency (3.47), $\omega_g(t)$, $\omega_{VSM}(t)$ is the pu virtual rotor angular speed, $p^{r^*}(t)$ is the APC output signal: the pu virtual mechanical input power, T_a is the virtual inertia time constant (mechanical starting time), $p(t)$ is the pu active power (measurement) (3.48) and k_d is the damping factor (coefficient) and $\omega_{PLL}(t)$ is the phase lock (phase-locked) loop (PLL) output signal: the pu estimated grid angular frequency. The corresponding block diagram is shown

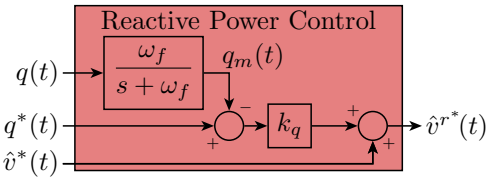

Figure 3.11: *Virtual synchronous machine reactive power control*

in the right side of Figure 3.10. As mentioned in Sections 2.2.1 and 3.2.4, the term $k_d\left[\omega_{VSM}(t) - \omega_{PLL}(t)\right]$ includes a component of (virtual) damping power not accounted for in $p(t)$. This allows the emulation of the damping provided by the SM amortisseur circuits without explicitly considering them in the (reduced-order) model.

$$\frac{\mathrm{d}}{\mathrm{d}t}\delta\omega_{VSM}(t) = \frac{p^{r^*}(t)}{T_a} - \frac{p(t)}{T_a} - \frac{k_d\left[\omega_{VSM}(t) - \omega_{PLL}(t)\right]}{T_a} \approx \frac{\mathrm{d}}{\mathrm{d}t}\omega_{VSM}(t) \tag{3.46}$$

$$\delta\omega_{VSM}(t) = \omega_{VSM}(t) - \omega_g(t) \tag{3.47}$$

$$p(t) = v_{o,d}(t)i_{o,d}(t) + v_{o,q}(t)i_{o,q}(t) \tag{3.48}$$

Expressions for the virtual internal voltage phase (angle) difference, $\delta\theta_{VSM}(t)$, and the virtual internal voltage phase angle, $\theta_{VSM}(t)$, are given by (3.49) and (3.50), respectively.

$$\frac{\mathrm{d}}{\mathrm{d}t}\delta\theta_{VSM}(t) = \omega_b\delta\omega_{VSM}(t) = \omega_b\omega_{VSM}(t) - \omega_b\omega_g(t) \tag{3.49}$$

$$\frac{\mathrm{d}}{\mathrm{d}t}\theta_{VSM}(t) = \omega_b\omega_{VSM}(t) = \omega_b\delta\omega_{VSM}(t) + \omega_b\omega_g(t) \tag{3.50}$$

As in Section 3.2.5, APC is provided by an active power-frequency droop (3.51) that models the the SM speed governor steady-state characteristics [13], with $p^*(t)$ being the pu (external) active power set-point (reference), k_ω the active power-frequency droop gain (constant) and $\omega^*(t)$ the pu (external) angular frequency/speed reference (set-point). The corresponding block diagram is shown in the left side of Figure 3.10.

$$p^{r^*}(t) = p^*(t) - k_\omega\left[\omega_{VSM}(t) - \omega^*(t)\right] \tag{3.51}$$

3.4.3 Reactive power control

As in Section 3.2.6, the applied droop-based RPC is similar to those commonly used in microgrid systems [13, 32, 34]. The corresponding block diagram is shown in Figure 3.11.

The RPC output signal: the pu virtual internal voltage amplitude reference, $\hat{v}^{r^*}(t)$, is calculated by (3.52), where $\hat{v}^*(t)$ is the pu (external) voltage amplitude set-point (reference), k_q is the reactive power-voltage droop gain (constant), $q^*(t)$ is the pu (external) reactive power set-point (reference) and $q_m(t)$ is the pu filtered reactive power measurement. The state-space equation representing the applied first-order low-pass filter is given by (3.53),

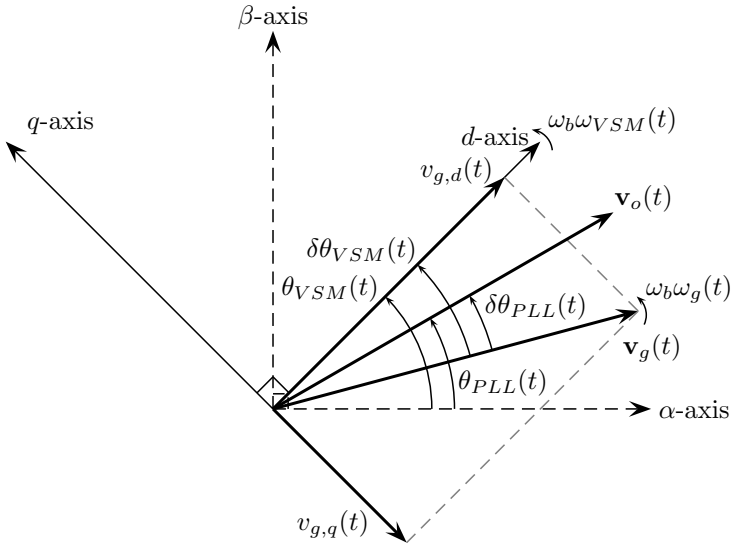

Figure 3.12: *Vector diagram defining the VSM RRF and voltage CSV orientations*

where $q(t)$ is the pu reactive power measurement (3.54) and ω_f is the filter cut-off angular frequency.

$$\hat{v}^{r^*}(t) = \hat{v}^*(t) + k_q \left[q^*(t) - q_m(t)\right] \tag{3.52}$$

$$\frac{\mathrm{d}}{\mathrm{d}t} q_m(t) = -\omega_f q_m(t) + \omega_f q(t) \tag{3.53}$$

$$q(t) = -v_{o,d}(t) i_{o,q}(t) + v_{o,q}(t) i_{o,d}(t) \tag{3.54}$$

3.4.4 Refence frame orientations

In steady state, the VSM RRF rotates with the same angular speed as the grid voltage. Thus, the virtual internal voltage phase angle, $\theta_{VSM}(t)$, continuously increases, as shown in the vector diagram in Figure 3.12. The virtual internal voltage phase (angle) difference (displacement), $\delta\theta_{VSM}(t)$, represents the phase difference between the VSM RRF d-axis and the rotating grid voltage vector, as shown also in Figure 3.12. Assuming $\hat{v}_g(t)$ to be known, the pu grid voltage CSV in the VSM RRF, $\mathbf{v}_g^{VSM}(t)$, is then given by (3.55)

$$\mathbf{v}_g^{VSM}(t) = \hat{v}_g(t) \mathrm{e}^{-\mathrm{j}\delta\theta_{VSM}(t)} \tag{3.55}$$

While estimating the value of $\omega_g(t)$, necessary to implement the virtual damping effect in the VSM swing equation, the PLL establishes its own RRF aligned with $\mathbf{v}_o(t)$, whose angles are defined in Figure 3.12 analogously to the ones of the VSM RRF. In order to model the PLL in its own RRF, $\mathbf{v}_o(t)$ can be transformed from the VSM RRF, $\mathbf{v}_o^{VSM}(t)$, to the PLL RRF, $\mathbf{v}_o^{PLL}(t)$, by (3.56), where $\delta\theta_{PLL}(t)$ is the PLL phase (angle) difference (displacement).

$$\mathbf{v}_o^{PLL}(t) = \mathbf{v}_o^{VSM}(t) \mathrm{e}^{-\mathrm{j}[\delta\theta_{PLL}(t) - \delta\theta_{VSM}(t)]} \tag{3.56}$$

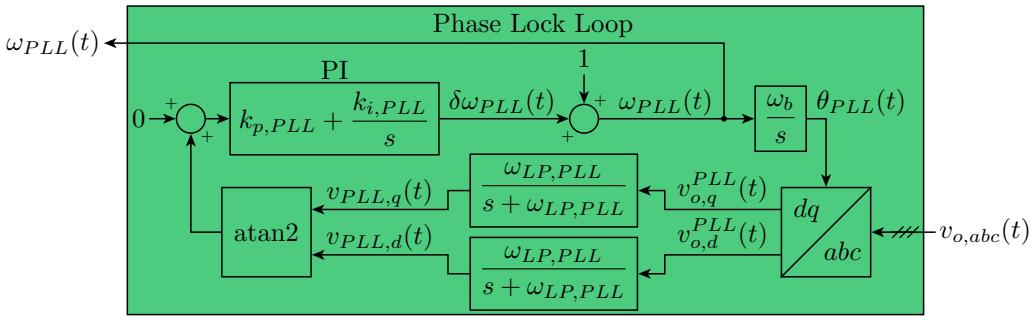

Figure 3.13: *Virtual synchronous machine phase lock loop*

3.4.5 Phase lock loop

The structure of the PLL, used for tracking the value of $\omega_g(t)$ [13, 20, 21] is shown in Figure 3.13. The PI controller output: the pu PLL angular speed deviation, $\delta\omega_{PLL}(t)$, is given by (3.57), where $k_{p,PLL}$ and $k_{i,PLL}$ are the PI controller proportional and integral gains, respectively, $v_{PLL,d}(t)$ and $v_{PLL,q}(t)$ are the pu low-pass filtered PCC (filter capacitors) voltage CSV d- and q-axis components in the PLL RRF (3.58), $\mathbf{v}_{PLL}(t)$, respectively, $\omega_{LP,PLL}$ is the filters cut-off angular frequency and the state $\varepsilon_{PLL}(t)$ represents the PI controller integrator (3.59). In calculating $\omega_{PLL}(t)$ from the controller output signal, $\delta\omega_{PLL}(t)$, the expression defining their relationship (3.60), analogous to the one given for the swing equation, has been linearised with respect to $\omega_g(t)$.

$$\delta\omega_{PLL}(t) = k_{p,PLL} \arctan\left[\frac{v_{PLL,q}(t)}{v_{PLL,d}(t)}\right] + k_{i,PLL}\varepsilon_{PLL}(t) \tag{3.57}$$

$$\frac{\mathrm{d}}{\mathrm{d}t}\mathbf{v}_{PLL}(t) = -\omega_{LP,PLL}\mathbf{v}_{PLL}(t) + \omega_{LP,PLL}\mathbf{v}_o^{PLL}(t) \tag{3.58}$$

$$\frac{\mathrm{d}}{\mathrm{d}t}\varepsilon_{PLL}(t) = \arctan\left[\frac{v_{PLL,q}(t)}{v_{PLL,d}(t)}\right] \tag{3.59}$$

$$\omega_{PLL}(t) = \delta\omega_{PLL}(t) + \omega_g(t) \approx \delta\omega_{PLL}(t) + 1 \tag{3.60}$$

Also in accordance with the definitions introduced for the swing equation, expressions for $\delta\theta_{PLL}(t)$ and the phase angle, $\theta_{PLL}(t)$, are given by (3.61) and (3.62), respectively. As shown in Figure 3.13, $\theta_{PLL}(t)$ is used as the transformation angle for the (amplitude-invariant) Park transformation of the measured $\mathbf{v}_o(t)$ into the PLL RRF.

$$\frac{\mathrm{d}}{\mathrm{d}t}\delta\theta_{PLL}(t) = \omega_b\delta\omega_{PLL}(t) \approx \omega_b\omega_{PLL}(t) - \omega_b \tag{3.61}$$

$$\frac{\mathrm{d}}{\mathrm{d}t}\theta_{PLL}(t) = \omega_b\omega_{PLL}(t) \approx \omega_b\delta\omega_{PLL}(t) + \omega_b \tag{3.62}$$

3.4.6 Virtual impedance and voltage control

The RPC output signal: the pu virtual internal voltage amplitude reference, $\hat{v}^{r^*}(t)$, is passed through a virtual impedance (VI) before being used as a reference for controlling

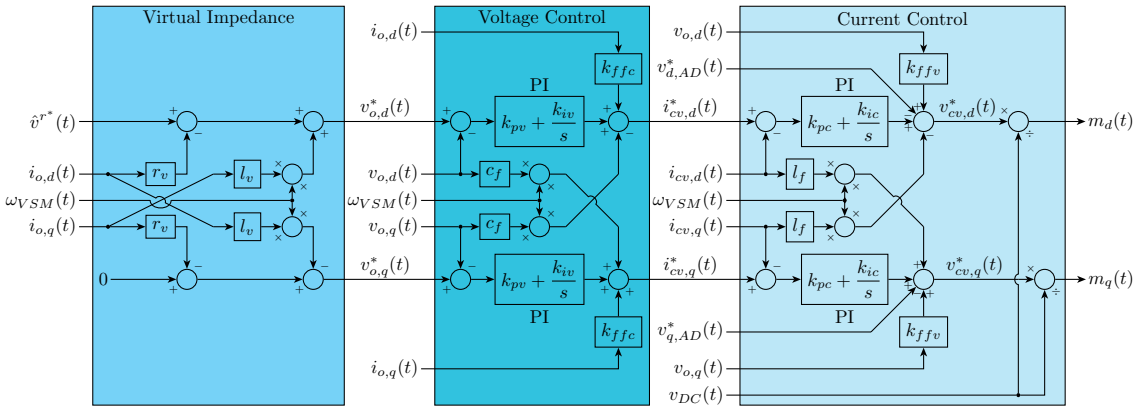

Figure 3.14: *Virtual synchronous machine virtual impedance, voltage control and current control*

$\mathbf{v}_o(t)$, as shown in Figure 3.9. The VI can be seen as an emulation of a SM synchronous impedance quasi-stationary characteristics. It affects the dynamic and steady-state characteristics of the VSM, and can be used to modify the system dynamic characteristics. The VI also reduces the VSM sensitivity to small disturbances in the grid, as the virtual power flowing through it causes a phase angle displacement between the PCC voltage and the VSM virtual internal voltage, and makes the VSM control the virtual internal voltage instead of the the actual PCC voltage. The effect of the pu virtual resistance, r_v, and inductance, l_v, on the pu PCC (filter capacitors) voltage CSV reference, $\mathbf{v}_o^*(t)$, is shown in the left side of Figure 3.14, and is given by (3.63) [13, 17, 18].

$$\mathbf{v}_o^*(t) = \hat{v}^{r^*}(t) - [r_v + \mathrm{j}l_v\omega_{VSM}(t)]\,\mathbf{i}_o(t) \tag{3.63}$$

The voltage control (VC) consists of RRF PI controllers with decoupling terms [13, 32], as shown in the middle of Figure 3.14. The VC output signals: the pu VSC current CSV reference for the VSC, $\mathbf{i}_{cv}^*(t)$, is given by (3.64), where k_{pv} and k_{iv} are the PI controllers proportional and integral gains, respectively, the states $\boldsymbol{\xi}(t)$ represent the PI controllers integrators (3.65) and k_{ffc} is the current feed-forward gain, used for disabling or enabling the forward feeding of the measured $\mathbf{i}_o(t)$ in the controllers output.

$$\mathbf{i}_{cv}^*(t) = k_{pv}\left[\mathbf{v}_o^*(t) - \mathbf{v}_o(t)\right] + k_{iv}\boldsymbol{\xi}(t) + \mathrm{j}c_f\omega_{VSM}(t)\mathbf{v}_o(t) + k_{ffc}\mathbf{i}_o(t) \tag{3.64}$$

$$\frac{\mathrm{d}}{\mathrm{d}t}\boldsymbol{\xi}(t) = \mathbf{v}_o^*(t) - \mathbf{v}_o(t) \tag{3.65}$$

3.4.7 Current control and active damping

The inner loop current control (CC) consists also of RRF PI controllers with decoupling terms [3, 13, 32], as shown in the right side of Figure 3.14. The CC output signals: the pu VSC voltage CSV reference for the VSC, $\mathbf{v}_{cv}^*(t)$, is given by (3.66), where k_{pc} and k_{ic} are the PI controller proportional and integral gains, respectively, the states $\boldsymbol{\gamma}(t)$ represent the PI controllers integrators (3.67), k_{ffv} is the voltage feed-forward gain, used for disabling or enabling the forward feeding of the measured $\mathbf{v}_o(t)$ in the controllers output and $\mathbf{v}_{AD}^*(t)$

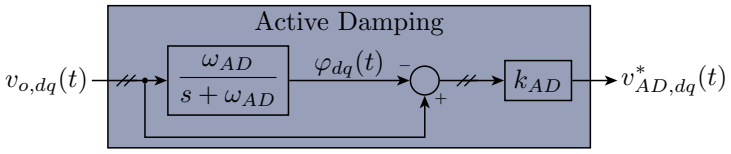

Figure 3.15: *Virtual synchronous machine active damping*

is a pu active damping term included and designed for suppressing LC oscillations in the filter [3, 13].

$$\begin{aligned}\mathbf{v}^*_{cv}(t) \;=\; & k_{pc}\left[i^*_{cv}(t) - i_{cv}(t)\right] + k_{ic}\boldsymbol{\gamma}(t) \\ & + \mathrm{j}l_f\omega_{VSM}(t)\mathbf{i}_{cv}(t) + k_{ffv}\mathbf{v}_o(t) - \mathbf{v}^*_{AD}(t) \qquad (3.66)\end{aligned}$$

$$\frac{\mathrm{d}}{\mathrm{d}t}\boldsymbol{\gamma}(t) \;=\; \mathbf{i}^*_{cv}(t) - \mathbf{i}_{cv}(t) \qquad (3.67)$$

The active damping algorithm, shown in Figure 3.15, is based on high-pass filtering of the pu measured $\mathbf{v}_o(t)$, implemented as the difference between $\mathbf{v}_o(t)$ and its low-pass filtered value, $\boldsymbol{\varphi}(t)$. The state-space equation representing the applied first-order low-pass filters is given by (3.68), where ω_{AD} is the filters cut-off angular frequency. The obtained high-pass filtered signal is then scaled by the active damping gain (3.69), k_{AD}.

$$\frac{\mathrm{d}}{\mathrm{d}t}\boldsymbol{\varphi}(t) \;=\; \omega_{AD}\mathbf{v}_o(t) - \omega_{AD}\boldsymbol{\varphi}(t) \qquad (3.68)$$

$$\mathbf{v}^*_{AD}(t) \;=\; k_{AD}\left[\mathbf{v}_o(t) - \boldsymbol{\varphi}(t)\right] \qquad (3.69)$$

To implement the VSC control system, the reference $\mathbf{v}^*_{cv}(t)$ is divided by the pu measured DC link voltage, $v_{DC}(t)$, to produce the modulation index (ratio) CSV, $\mathbf{m}(t)$, as displayed in the right of Figure 3.14. Neglecting the VSC switching operation and any delay related to the implementation of the PWM, the instantaneous average value of $\mathbf{v}_{cv}(t)$ is given by (3.70) [13, 23].

$$\mathbf{m}(t) = \frac{\mathbf{v}^*_{cv}(t)}{v_{DC}(t)}\ ,\ \mathbf{v}_{cv}(t) = \mathbf{m}(t)v_{DC}(t)\ \Rightarrow\ \mathbf{v}_{cv}(t) \approx \mathbf{v}^*_{cv}(t) \qquad (3.70)$$

3.4.8 Nonlinear model

Assuming $v_{DC}(t) = 1\,\mathrm{pu}$, equations (3.43)-(3.70) can be reduced to a model on state-space form with 19 distinct state variables and 6 input signals [13], with the state vector, $\mathbf{x}_{VSM}(t)$, defined by (3.71), and the input vector, $\mathbf{u}_{VSM}(\mathrm{t})$, defined by (3.72). Terms such as $\omega_g(t)\mathbf{i}_{cv}(t)$ in (3.43), $\omega_g(t)\mathbf{v}_o(t)$ in (3.44), $\omega_g(t)\mathbf{i}_o(t)$ in (3.45), $\arctan\left[v_{PLL,q}(t)/v_{PLL,d}(t)\right]$ in (3.57) and (3.59), $v_{o,d}(t)i_{o,d}(t)$ and $v_{o,q}(t)i_{o,q}(t)$ in (3.48), $v_{o,d}(t)i_{o,q}(t)$ and $v_{o,q}(t)i_{o,d}(t)$ in (3.54), $\hat{v}_g(t)\mathrm{e}^{-\mathrm{j}\delta\theta_{VSM}(t)}$ in (3.55), $\mathbf{v}_o^{VSM}(t)\mathrm{e}^{-\mathrm{j}\delta\theta_{PLL}(t)}$ and $\mathbf{v}_o^{VSM}(t)\mathrm{e}^{\mathrm{j}\delta\theta_{VSM}(t)}$ in (3.56), $\omega_{VSM}(t)\mathbf{i}_o(t)$ in (3.63), $\omega_{VSM}(t)\mathbf{v}_o(t)$ in (3.64) and $\omega_{VSM}(t)\mathbf{i}_{cv}(t)$ in (3.66) make the model nonlinear.

$$\begin{aligned}\mathbf{x}_{VSM}(t) \doteq [&v_{o,d}(t)\ v_{o,q}(t)\ i_{cv,d}(t)\ i_{cv,q}(t)\ \gamma_d(t)\ \gamma_q(t)\ i_{o,d}(t)\ \cdots \\ &\cdots\ i_{o,q}(t)\ \varphi_d(t)\ \varphi_q(t)\ v_{PLL,d}(t)\ v_{PLL,q}(t)\ \varepsilon_{PLL}(t)\ \cdots \\ &\cdots\ \delta\theta_{VSM}(t)\ \xi_d(t)\ \xi_q(t)\ q_m(t)\ \delta\omega_{VSM}(t)\ \delta\theta_{PLL}(t)]^T\end{aligned} \tag{3.71}$$

$$\mathbf{u}_{VSM}(t) \doteq [p^*(t)\ q^*(t)\ \hat{v}_g(t)\ \hat{v}^*(t)\ \omega^*(t)\ \omega_g(t)]^T \tag{3.72}$$

3.4.9 Small-signal model

Classical stability assessment techniques based on eigenvalues are not directly applicable to the nonlinear state-space model. As in Section 3.2.10, a linearised small-signal state-space model can be consequently derived [13], with the form given by (3.73), where the prefix Δ denotes small-signal deviations around the steady-state operating point [24], $\mathbf{A}_{VSM}$ is the state (system, dynamic) matrix and $\mathbf{B}_{VSM}(t)$ is the input matrix.

$$\boldsymbol{\Delta}\dot{\mathbf{x}}_{VSM}(t) \doteq \frac{\mathrm{d}}{\mathrm{d}t}\boldsymbol{\Delta}\mathbf{x}_{VSM}(t) = \mathbf{A}_{VSM}\boldsymbol{\Delta}\mathbf{x}_{VSM}(t) + \mathbf{B}_{VSM}\boldsymbol{\Delta}\mathbf{u}_{VSM}(t) \tag{3.73}$$

Chapter 4

Simulation results

In this chapter, a base case is defined and simulation results are presented and discussed. These include: dynamic responses of the base case systems to changes in their inputs (from time-step simulations); base case eigenvalues, participation factors and parametric sensitivities; and eigenvalue traces for system inputs and parameters varying around the base case values.

The dynamic (nonlinear) models of the investigated systems and their corresponding small-signal (linearised) state-space models have been implemented in MATLAB Simulink. For the synchronous machine (SM) and virtual synchronous machine systems, the corresponding initial conditions have been calculated by numerically solving and evaluating the expressions derived in Maple for the solution of the nonlinear equations in steady-state conditions. For the SM system plus grid impedance (SMg system), developed at a later stage, the corresponding initial conditions have been calculated by time-step simulations. The SimPowerSystems blockset has been used to model the electrical systems, with controllable voltage source blocks representing the ideal average model of the voltage source converter (VSC), in the case of the VSM system.

The base case has been defined by taking the parameters and initial inputs from [13]. The rated (apparent) power, S_{rated}, is 2.749 MVA, and the rated voltage, V_{rated}, is $690\,\text{V}_{\text{rms,L-L}}$. The SM(g) system base case parameters and initial inputs are given in Table 4.1. A salient-pole SM is represented by the general model (amortisseur circuits are considered, damping factor, $k_{d,SM}$, is set to 0) excluding the 2nd q-axis amortisseur circuit (e.g., by setting its pu resistance, r_{2q}, to a high value). The virtual synchronous machine (VSM) system base case parameters and initial inputs are specified in Table 4.2. Where possible, the SM base case parameters are equal the corresponding ones of the VSM base case, to facilitate comparison. Only 5 parameters in the VSM system correspond to the electrical system, and are thus taken as fixed. As opposed to the VSM system, most of the SM system parameters are assumed to be fixed, and only 5 parameters are considered tunable.

Table 4.1: *SM(g) system base case parameters (top) and initial inputs (bottom)*

Par.	Value	Par.	Value	Par.	Value
S_{rated}	2.749 MVA	l_{11d}	1.405 pu	$k_{p,ex}$	0.023 53
V_{rated}	690 $V_{\text{rms,L-L}}$	l_{f1d}	1.117 pu	$k_{i,ex}$	5.028×10^{-3}
ω_b	100π rad/s	r_a	4.044×10^{-3} pu	$k_{\omega,SM}$	20
T_{SM}	2 s	l_{ad}	1.117 pu	$\omega_{f,SM}$	1000 rad/s
$k_{d,SM}$	0	l_l	0.054 50 pu	$k_{q,SM}$	0.2
r_{2q}	—	l_{aq}	0.4772 pu	c_{mg}	1×10^{-5} pu
l_{22q}	—	r_{fd}	8.476×10^{-4} pu	l_{mg}	0.2 pu
r_{1q}	0.028 59 pu	l_{ffd}	1.363 pu	r_{mg}	0.01 pu
l_{11q}	1.672 pu	T_{gt}	0.5 s		
r_{1d}	0.041 00 pu	T_{ex}	0.1 s		
Var.	Value	Var.	Value	Var.	Value
$p^*_{SM}(0)$	0.5010 pu	$\omega^*_{SM}(0)$	1 pu	$\omega_g(0)$	1 pu
$q^*_{SM}(0)$	0 pu	$\hat{v}^*_{SM}(0)$	1 pu	$\hat{v}_g(0)$	1 pu

Table 4.2: *VSM system base case parameters (top) and initial inputs (bottom)*

Par.	Value	Par.	Value	Par.	Value
S_{rated}	2.749 MVA	r_g	0.01 pu	k_{ic}	14.25
V_{rated}	690 $V_{\text{rms,L-L}}$	r_v	0 pu	k_{ffv}	1
ω_b	100π rad/s	l_v	0.2 pu	$\omega_{LP,PLL}$	500 rad/s
T_a	2 s	k_{pv}	0.5889	$k_{p,PLL}$	0.084 43
k_d	400	k_{iv}	736.1	$k_{i,PLL}$	4.691
c_f	0.074 pu	k_{ffc}	0	k_ω	20
l_f	0.08 pu	ω_{AD}	50 rad/s	ω_f	1000 rad/s
r_f	2.85×10^{-3} pu	k_{AD}	0.5	k_q	0.2
l_g	0.2 pu	k_{pc}	1.273		
Var.	Value	Var.	Value	Var.	Value
$p^*(0)$	0.5 pu	$\omega^*(0)$	1 pu	$\omega_g(0)$	1 pu
$q^*(0)$	0 pu	$\hat{v}^*(0)$	1.02 pu	$\hat{v}_g(0)$	1 pu

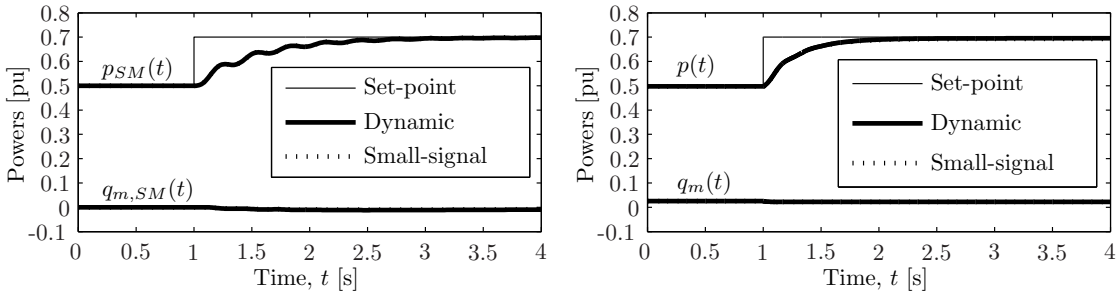

Figure 4.1: *SM (left) and VSM (right) pu active and low-pass-filtered reactive power response to a step change in the active power set-point*

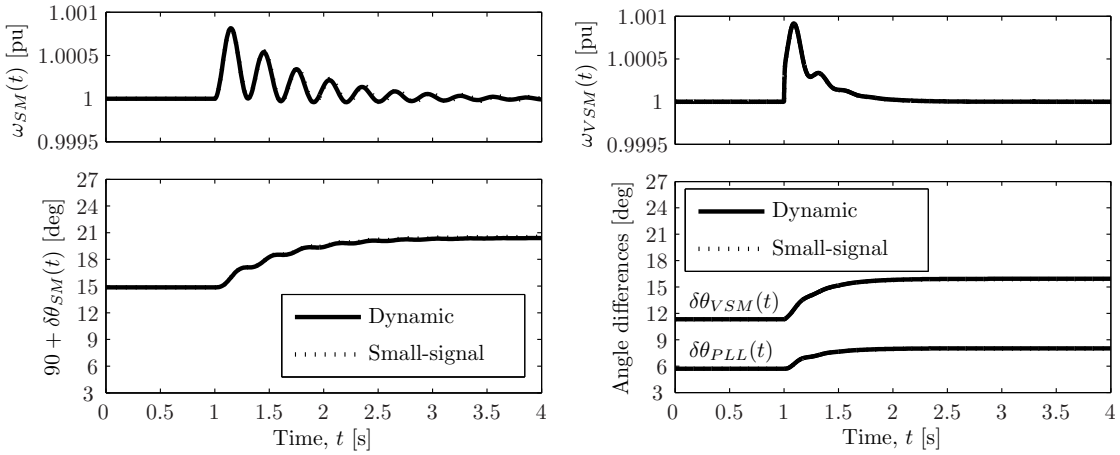

Figure 4.2: *SM (left) and VSM (right) (virtual) rotor angular speed and (phase) angle differences (displacements) response to a step change in the active power set-point*

4.1 Dynamic response

In order to validate the small-signal models, their dynamic responses have been verified to match those of the dynamic (nonlinear) models around the linearisation points. Multiple numerical time-step numerical simulations have been performed on different steady-state operating (linearisation) points. Some of the results of a couple simulation cases are shown in this section. These cases and the presented dynamic responses have been chosen to reproduce those shown in [13] for the VSM system small-signal model and facilitate their comparison with those corresponding to the SM(g) system small-signal model.

4.1.1 Change in the loading

Figures 4.1 and 4.2 show some of the dynamic responses of the SM and VSM systems to a step change in the pu (external) active power set-point (reference), $p^*_{SM}(t), p^*(t)$. The pu active power set-point and the pu active and low-pass filtered reactive powers are plotted in Figure 4.1, while the (virtual) rotor angular speed and the corresponding (phase) angle differences (displacements) are shown in Figure 4.2. To facilitate comparison, the SM rotor (phase) angle difference (displacement), $\delta\theta_{SM}(t)$, is shifted by 90°.

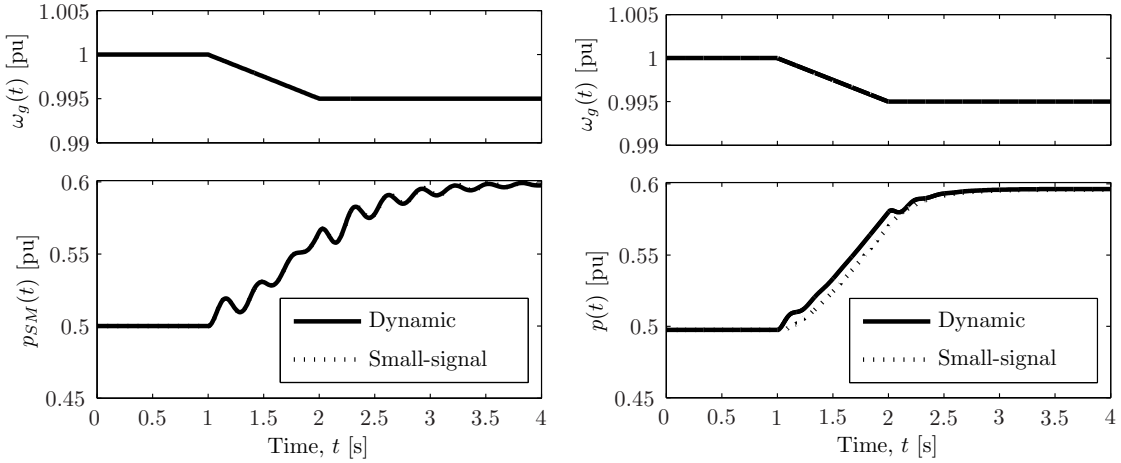

Figure 4.3: *SM (left) and VSM (right) pu active power response to a ramp change in the grid frequency*

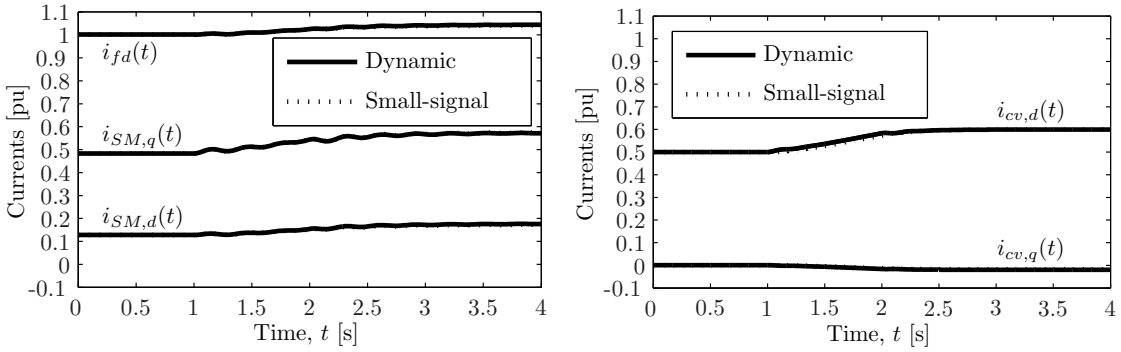

Figure 4.4: *SM (left) and VSM (right) pu currents response to a ramp change in the grid frequency*

As discussed in [13], the excess power input accumulates in the (virtual) inertia, which leads to an increase of the speed during the first part of the transient, resulting in an increase in the phase angle differences. Once the electrical power output reaches the input power, the system steady-state power balance is restored, and the value of the (virtual) rotor angular speed returns to that of the grid angular frequency. The VSM system dynamic responses present the same general characteristics as those of the SM system. However, since the VSM damping factor, k_d, can be chosen without considering any of the physical constraints in a SM, its high value makes the VSM responses more damped.

4.1.2 Change in the grid frequency

Figures 4.3 and 4.4 show some of the dynamic responses of the SM and VSM systems to a ramp change in the pu grid angular frequency, $\omega_g(t).\omega_g(t)$ and the pu active powers are plotted in Figure 4.3, while some of the pu currents are plotted in Figure 4.4.

In response to the change in $\omega_g(t)$, the active power control (APC) increases the active

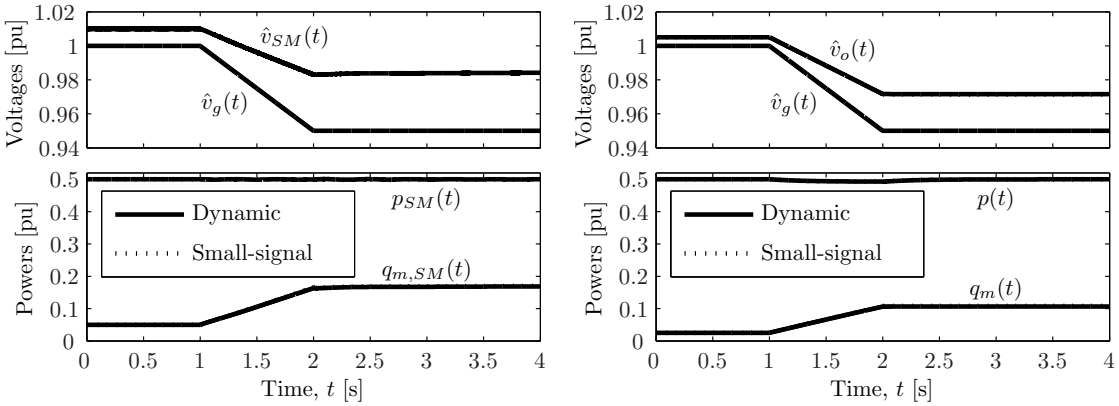

Figure 4.5: *SMg (left) and VSM (right) dynamic response to a ramp change in the pu grid voltage amplitude*

power output to contribute to the system frequency control. The (virtual) rotor angular speed follows $\omega_g(t)$, releasing energy from its (virtual) inertia. Again, the high k_d makes the VSM response more damped. As discussed in [13], the VSM system (linearised) small-signal model cannot represent correctly the dynamic transition to a new operating point with a $\omega_g(t)$ different from that of the linearisation point. This can be attributed to the choice of the virtual rotor angular speed deviation, $\delta\omega_{VSM}(t)$, instead of its angular speed, $\omega_{VSM}(t)$, as a state variable in the VSM system model. For that reason, there is a small deviation between the VSM system nonlinear and linearised models while $\omega_g(t)$ is changing and shortly after it settles to its new value. The VSM system linearised model is nevertheless able to represent the corresponding change in the steady-state active power, thanks to a contribution from the change in $\omega_g(t)$ through the input matrix (3.73), $\mathbf{B}_{VSM}$. Since the SM rotor angular speed, $\omega_{SM}(t)$, has been chosen as state variable in the SM system model, all SM system dynamic (nonlinear) and small-signal (linearised) model responses present an excellent match.

4.1.3 Change in the grid voltage amplitude

Figure 4.5 shows some of the dynamic responses of the SMg and VSM systems to a ramp change in the pu grid voltage amplitude, $\hat{v}_g(t)$. $\hat{v}_g(t)$ and the pu voltage amplitude at the points of common coupling (PCC), $\hat{v}_{SM}(t), \hat{v}_o(t)$, are plotted at the top, while the active and low-pass-filtered reactive powers are plotted at the bottom.

In response to the change in $\hat{v}_g(t)$, the reactive power control (RPC) increases the reactive power output to contribute to voltage control. In comparison with the SMg system, the VSM system presents a greater difference between the PCC voltage and the voltage amplitude set-point (1.02 pu), but also a smaller change (less sensitive response) and a smaller steady-state error (the set-point values being 0 pu) in the reactive power output. This effect, comparable to that of increasing the VSM reactive power-voltage droop gain, can be attributed to the influence of the virtual impedance in the corresponding control loop.

The good match between the responses of the dynamic (nonlinear) models and the cor-

responding small-signal (linearised) state-space models indicates that the small-signal models accurately represent the investigated systems. This confirms the validity of the small-signal models around the steady-state operating points, and supports their use in the small-signal stability analysis of the systems by traditional linear techniques.

4.2 Eigenvalue analysis

Having verified the validity of the (linearised) small-signal models around the steady-state operating points, the stability of the systems has been confirmed for their whole operating ranges. This has been done by calculating the eigenvalues (modes), $\lambda_i = \sigma_i + \mathrm{j}\omega_i$, of their small-signal model state matrices, $\mathbf{A}_{SM}, \mathbf{A}_{SMg}, \mathbf{A}_{VSM}$, for the given base case parameters, with their initial inputs varying within the corresponding intervals. The unit of an eigenvalue imaginary part, ω_i, is rad/s, while Np/s is commonly used for the real part [24], σ_i. Usually, the mentioned units are used but not indicated explicitly, for convenience of notation.

Traces of SM and VSM (system) modes for varying active power set-points (the rest of their inputs as in the base cases) are plotted at the top and bottom of Figure 4.6, respectively. Enlarged views of the lower-frequency SM and VSM mode traces are shown at the top and bottom of Figure 4.7, respectively. The traces demonstrate that the systems are stable for the entire range of active power set-points. Moreover, the modes show little movement, which suggests that the systems have dynamic responses similar to those of the base case, for the different operating conditions within the operating ranges. Traces of SM(g) and VSM low-frequency modes for varying tunable parameters (the rest as in the base cases) are shown in Figures 4.12, 4.13, 4.17 and 4.18.

By combining the corresponding left and right eigenvectors, the respective participation factors have been calculated to determine the relationship between the eigenvalues and the states [24]. The eigenvalues *parametric sensitivity*: their sensitivity to a change in each of the system parameters, has been computed using the expressions obtained in Maple for the partial derivatives of the state matrices with respect to each of the system parameters, together with the corresponding left and right eigenvectors [30].

Using the magnitude of the participation factors, the main participating states have been identified for each mode. The eigenvalues and their main participating states are listed in Tables 4.3 and 4.4 for the SM and VSM systems, respectively. For each mode, the state with the highest participation factor magnitude is listed first. The states with a participation factor magnitude of at least 10 % of the highest are listed next in descending order of participation factor magnitude, with a superindex indicating the percentage of the highest. The *critical modes*: the slowest and least damped (closest to the origin), are of main interest for assessing the stability of the systems. The real part of the critical modes parametric sensitivity is depicted in Figures 4.8 to 4.11 for the SM system, and Figures 4.14 to 4.16 for the VSM system.

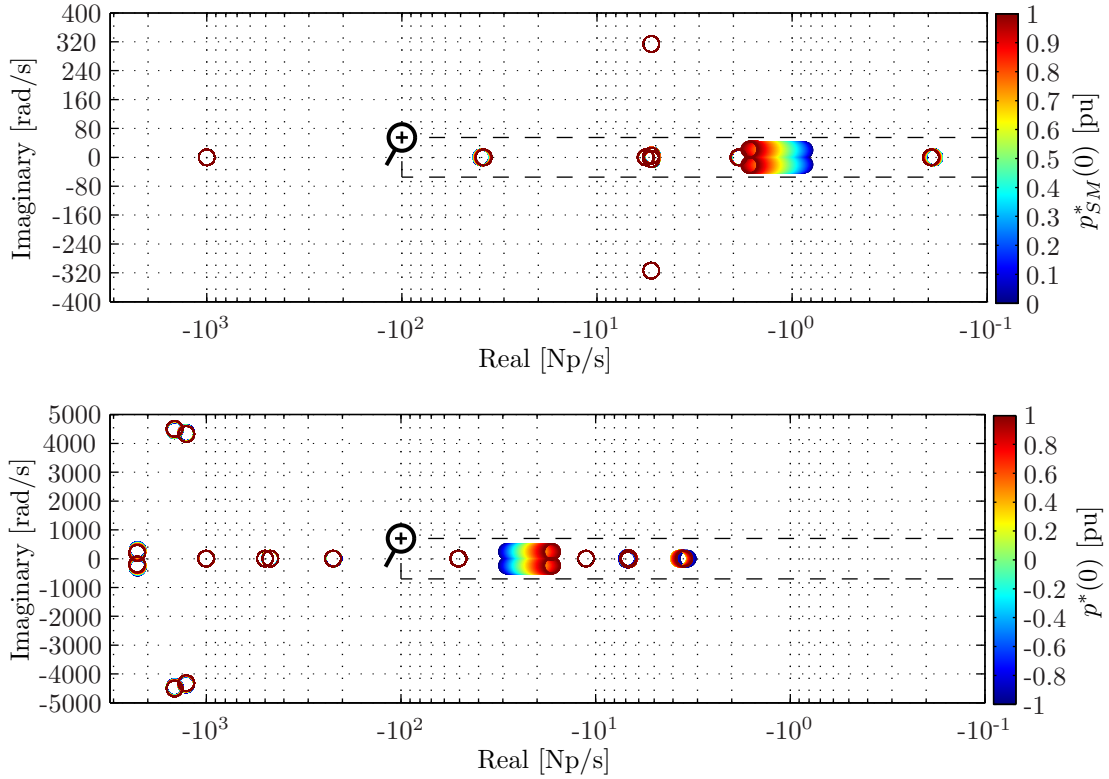

Figure 4.6: *Traces of SM (top) and VSM (bottom) modes for varying active power set-points (enlarged views of the lower-frequency mode traces in Figure 4.7)*

Table 4.3: *SM system base case eigenvalues (modes) and their main participating states*

Mode	Value	State	Mode(s)	Value(s)	State(s)
λ_1	-6.686×10^9	i_{2q}	$\lambda_{3,4}$	$-5.269 \pm \mathrm{j}314.0$	$i_{SM,d}$, $i_{fd}^{[46\%]}$, $i_{1d}^{[39\%]}$, $i_{SM,q}^{[20\%]}$
λ_2	-1000	$q_{m,SM}$	λ_5	-38.86	i_{1d} , $i_{SM,d}^{[56\%]}$, $i_{fd}^{[16\%]}$
λ_{11}	-1.866	$p_{m,SM}$	$\lambda_{8,9}$	$-5.245 \pm \mathrm{j}5.042$	i_{fd} , $i_{SM,d}^{[78\%]}$, $v_{fd}^{[24\%]}$
λ_{12}	-5.613	i_{1q}	λ_{10}	-0.1889	ζ , $i_{fd}^{[15\%]}$, $i_{SM,d}^{[11\%]}$
Mode(s)	Value(s)	State(s)			
$\lambda_{6,7}$	$-1.154 \pm \mathrm{j}20.70$	ω_{SM} , $\delta\theta_{SM}^{[96\%]}$, $i_{SM,d}^{[50\%]}$, $i_{fd}^{[41\%]}$, $i_{SM,q}^{[29\%]}$, $i_{1q}^{[28\%]}$, $i_{1d}^{[14\%]}$			

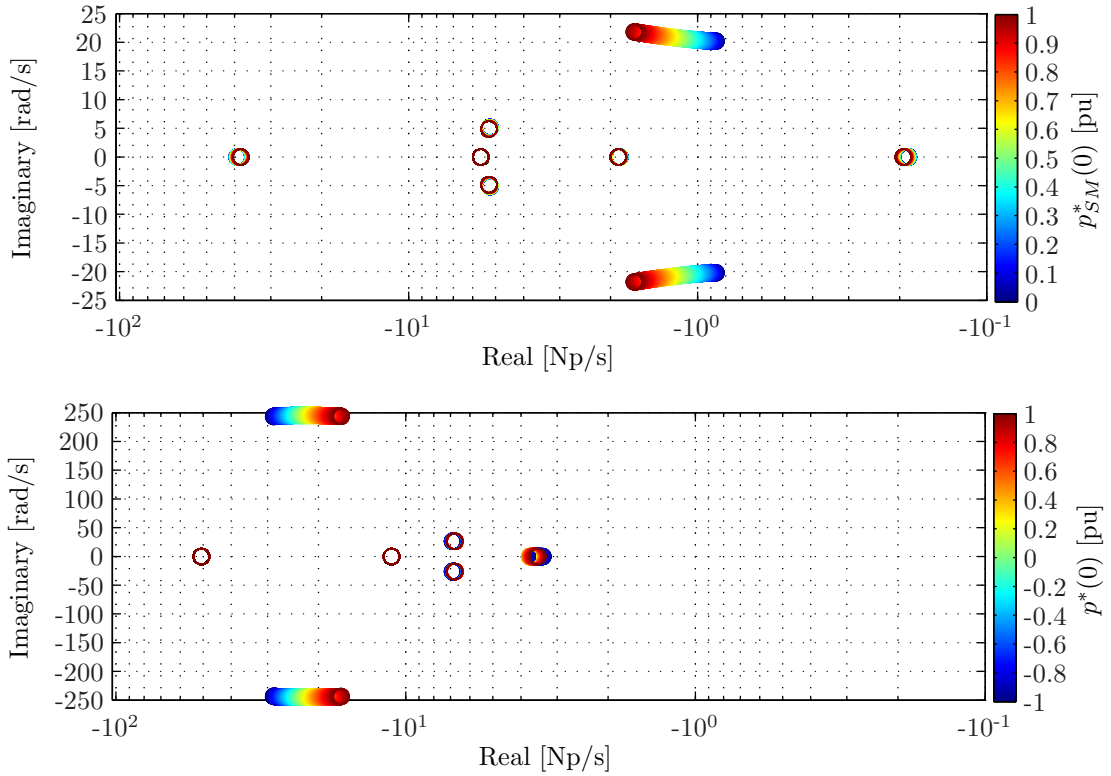

Figure 4.7: *Enlarged views of the lower-frequency SM (top) and VSM (bottom) mode traces for varying active power set-points (full view in Figure 4.6)*

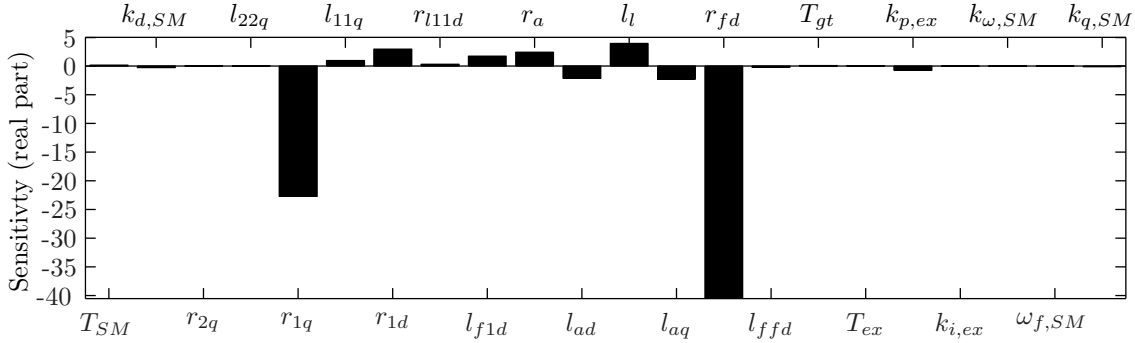

Figure 4.8: *Parametric sensitivity (real part) of SM modes* $\lambda_{6,7} \approx -1.154 \pm \mathrm{j}20.70$

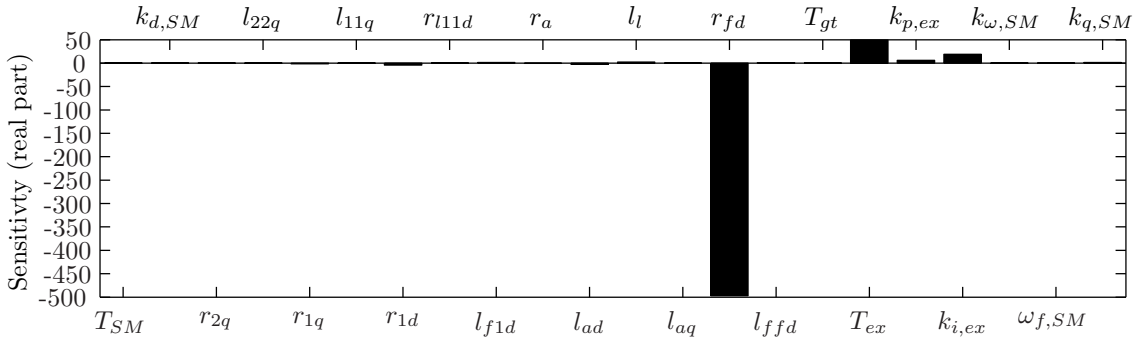

Figure 4.9: *Parametric sensitivity (real part) of SM modes* $\lambda_{8,9} \approx -5.245 \pm \mathrm{j}5.042$

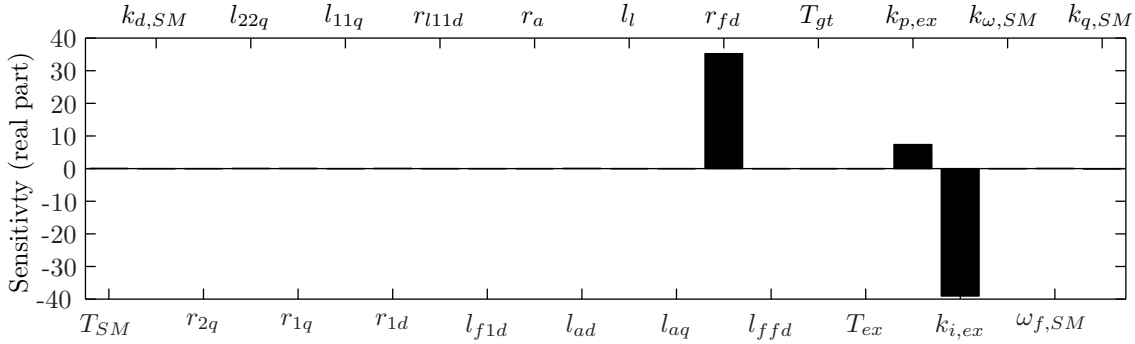

Figure 4.10: *Parametric sensitivity (real part) of SM mode* $\lambda_{10} \approx -0.1889$

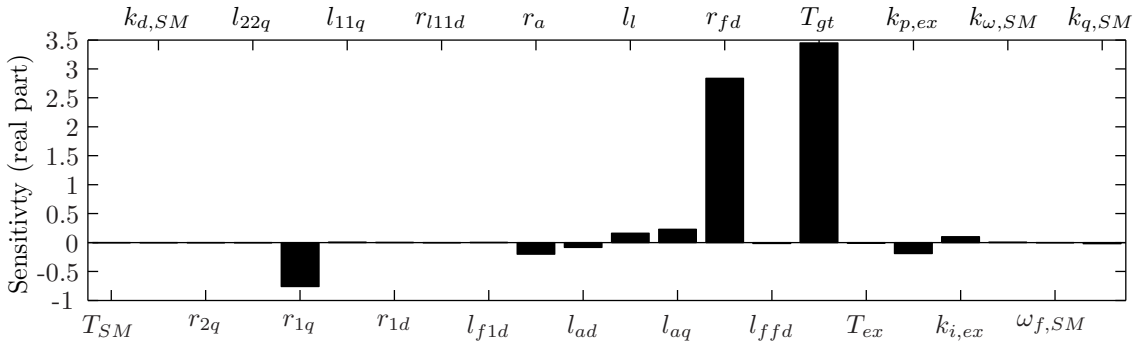

Figure 4.11: *Parametric sensitivity (real part) of SM mode* $\lambda_{11} \approx -1.866$

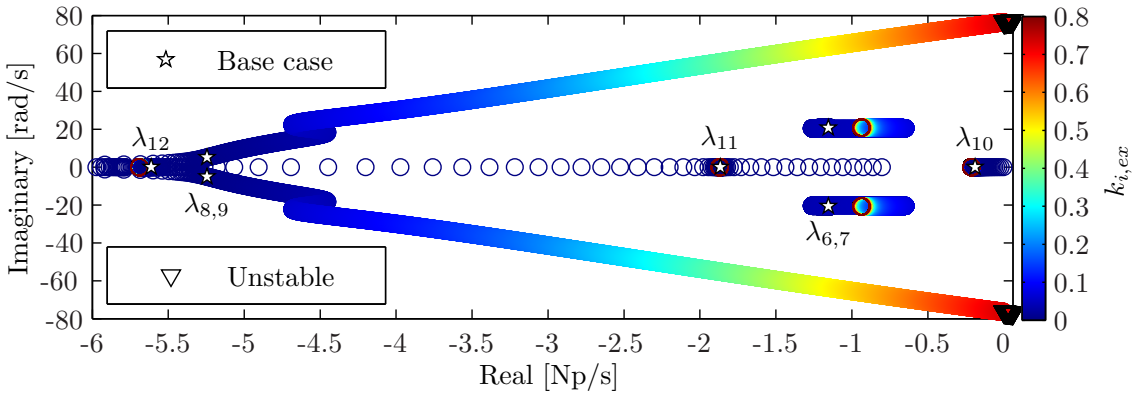

Figure 4.12: *Trace of SM low-frequency modes for varying exciter integral gain,* $k_{i,ex}$*, and integral time held constant at the base case value,* $k_{i,ex}/k_{p,ex} \approx 4.68\,\mathrm{s}$

4.2.1 Synchronous machine system

Table 4.3 indicates that λ_1 corresponds to the SM 2nd q-axis amortisseur circuit. Furthermore, its distant location from the imaginary axis is a result of the high value given to the corresponding pu resistance, r_{2q}, to exclude the circuit from the model, and is therefore not shown in Figure 4.6. Just as the VSM system, the SM system has an eigenvalue corresponding to the reactive power measurement low-pass filter at $\lambda \approx -1000$, which relates to the filter cut-off angular frequency.

Significant coupling between the SM current states can be appreciated by looking at the main participating states of modes 3 to 10 in Table 4.3. Moreover, most of the SM system eigenvalues are slower or not as well damped as the VSM system ones. From those, λ_{11} relates to the first-order system used to model the dynamic characteristics of the governor and the turbine, whose time constant, $T_{gt} = 0.5\,\text{s}$, is similar to that of the mode, $-1/\sigma_{11} \approx 0.5359\,\text{s}$. Figure 4.11 suggests that λ_{11} is mainly influenced by T_{gt}, and parametric sweep analysis has confirmed that, for a fixed T_{gt}, λ_{11} is relatively fixed as well, as can be seen in Figure 4.12. λ_5 and λ_{12} correspond to the 1st d- and q-axis amortisseur circuits, respectively, and are determined mainly by the SM parameters (taken as fixed).

Similarly to λ_5 and λ_{12}, the (complex conjugated) pair $\lambda_{3,4}$ is determined mainly by the SM parameters, and has shown to be relatively fixed. This pair represents the direct current (DC) offset of the armature phase currents, reflected in the SM rotating reference frame (RRF) as fundamental frequency components of the armature d- and q-axis currents, $i_{SM,d}, i_{SM,q}$. As opposed to them, the pair $\lambda_{8,9}$, corresponding to the field circuit, has also shown significant influence from the reactive power-voltage control loop through the field voltage, v_{fd}, making it more prone to move. Furthermore, $\lambda_{8,9}$ are the critical modes with the highest (most positive) sensitivity to changes in $k_{i,ex}$, which has demonstrated to be the tunning parameter that can most easily cause instability, as can be observed at the right of Figures 4.8 to 4.11, and in Figure 4.12. Table 4.3 suggests that λ_{10} corresponds to the exciter/AVR. Moreover, as depicted in Figure 4.10, the exciter/AVR tuning parameters, $k_{p,ex}, k_{i,ex}$, are the main tunable parameters influencing λ_{10}. As can be seen in Figure 4.12, its position has shown to be limited by the corresponding integral time, $k_{p,ex}/k_{i,ex}$, which has, for the base case, a value of 4.68 s.

The pair $\lambda_{6,7}$ relates to the rotor motion (swings), is mainly influenced by the SM parameters, as can be observed in Figure 4.8, and, as depicted in Figure 4.12, has shown limited movement. Furthermore, it is the least damped pair (closest to the origin) and thus dominates the oscillating component of the system dynamic response. This can be observed at the left of Figures 4.1 and 4.2, more evidently in the response of the rotor angular speed, $\omega_{SM}(t)$, in which the oscillation has a period of about $2\pi/|\omega_{6,7}| \approx 0.3035\,\text{s}$ and an amplitude that decays initially with a time constant of about $-1/\sigma_{6,7} \approx 0.8666\,\text{s}$. Its damping ratio, $-\sigma_{6,7}/\sqrt{\sigma_{6,7}^2+\omega_{6,7}^2} \approx 0.056 > 0.05$, indicates a damping that, in practise, is considered satisfactory for traditional power systems [30]. The unidirectional (aperiodic) component of the system dynamic response is dominated by the slowest (real) modes: λ_{10} and λ_{11}, and has, in the case of the mentioned responses, a time constant of about $-1/\sigma_{11} \approx 0.5359\,\text{s}$.

The modelled exciter has shown little capability of increasing the damping of oscillations.

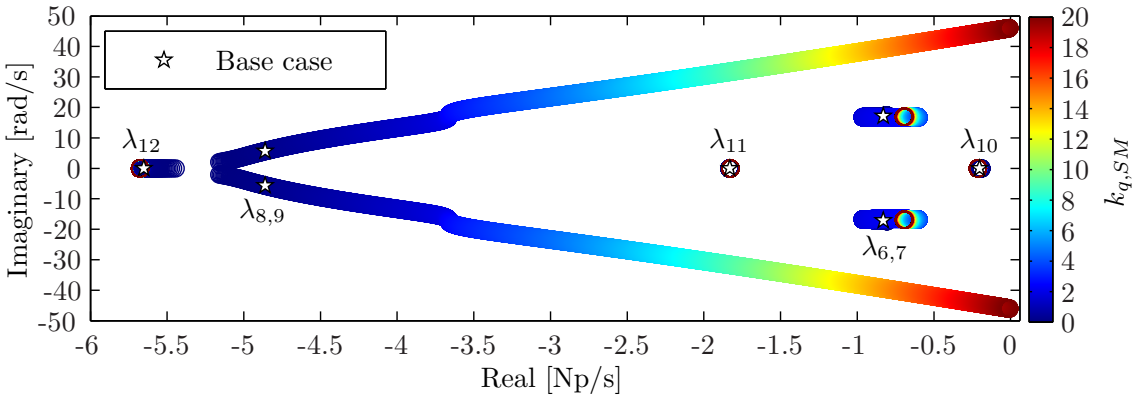

Figure 4.13: *Trace of SMg low-frequency modes for varying reactive power-voltage droop gain, $k_{q,SM}$*

Table 4.4: *VSM system base case eigenvalues (modes) and their main participating states*

Mode	Value	State	Mode(s)	Value(s)	State(s)
λ_1	-500.0	$v_{PLL,d}$	λ_{19}	-11.19	γ_d
λ_8	-1002	q_m	$\lambda_{2,3}$	$-1460 \pm \mathrm{j}4498$	$\mathbf{v}_o$, $\mathbf{i}_{cv}^{[59\,\%]}$, $\mathbf{i}_o^{[31\,\%]}$, $\boldsymbol{\xi}^{[12\,\%]}$
λ_9	-469.6	$v_{PLL,q}$	$\lambda_{4,5}$	$-1272 \pm \mathrm{j}4329$	$\mathbf{v}_o$, $\mathbf{i}_{cv}^{[65\,\%]}$, $\mathbf{i}_o^{[32\,\%]}$, $\boldsymbol{\xi}^{[14\,\%]}$
λ_{12}	-223.5	$\delta\omega_{VSM}$	$\lambda_{6,7}$	$-2262 \pm \mathrm{j}225.2$	$\mathbf{i}_{cv}$, $\mathbf{i}_o^{[68\,\%]}$, $\boldsymbol{\xi}^{[58\,\%]}$, $\mathbf{v}_o^{[52\,\%]}$, $q_m^{[20\,\%]}$
λ_{15}	-50.82	φ_q	$\lambda_{10,11}$	$-19.50 \pm \mathrm{j}245.0$	$\boldsymbol{\xi}$, $\mathbf{i}_o^{[48\,\%]}$, $q_m^{[12\,\%]}$
λ_{16}	-50.60	φ_d	$\lambda_{13,14}$	$-6.759 \pm \mathrm{j}26.38$	$\delta\theta_{PLL}$, $\delta\theta_{VSM}^{[51\,\%]}$, $\varepsilon_{PLL}^{[50\,\%]}$
λ_{18}	-11.20	γ_q	λ_{17}	-3.691	$\delta\theta_{VSM}$, $\delta\theta_{PLL}^{[48\,\%]}$

Moreover, since the SM is directly connected to a stiff grid, it can control its reactive power output to some extent, but has no control over the armature voltage, which is set by the grid. These restrictions suggest that, in order to make a more relevant comparison between this system and the VSM system, at least two changes should be considered in the modelling. A more detailed model of the exciter should be used, including a *power system stabiliser* (PSS), which uses auxiliary stabilising signals to provide more damping of oscillations by controlling the excitation [24]. Furthermore, the network equivalent impedance should be included in the modelling of the connection between the SM and the stiff grid. The latter has been implemented in the SMg system, developed at a later stage.

As opposed to that of the VSM system [13], the SM reactive power-voltage droop gain, $k_{q,SM}$, can be increased up to at least 20 without causing instability, as depicted in Figure 4.13 for the SMg system. This means that, by increasing this gain, the SM(g) system can attain a steady-state reactive power (sharing) error much smaller than that of the VSM system.

4.2.2 Virtual Synchronous machine system

As opposed to the SM system, most of the VSM system eigenvalues are fast or well damped, as can be seen in Figure 4.6, Figure 4.7 and Table 4.4. Moreover, the d-axis participating states have the same influence on the system response as the corresponding

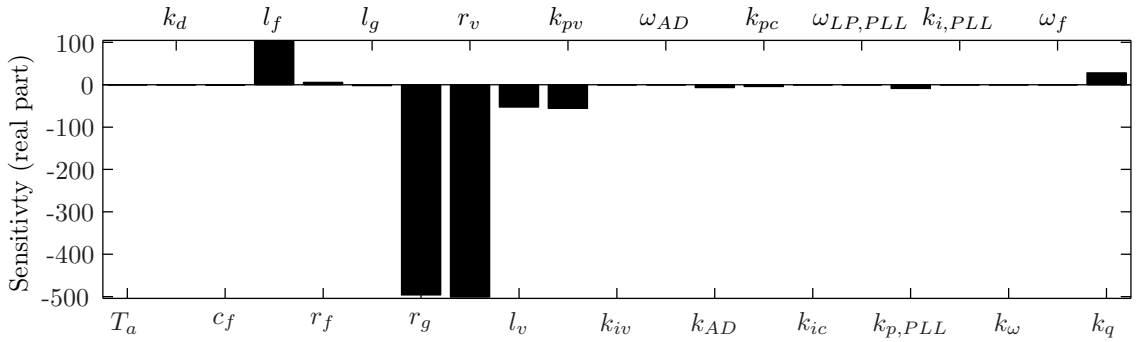

Figure 4.14: *Parametric sensitivity (real part) of VSM modes* $\lambda_{10,11} \approx -19.50 \pm \mathrm{j}245.0$

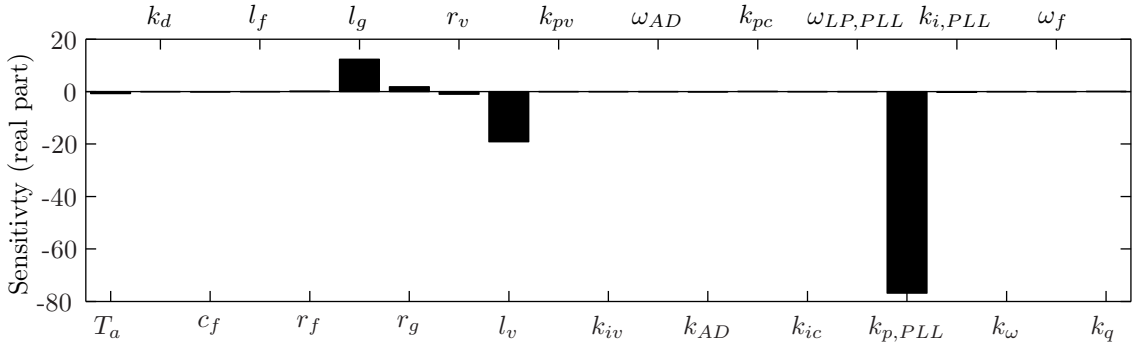

Figure 4.15: *Parametric sensitivity (real part) of VSM modes* $\lambda_{13,14} \approx -6.759 \pm \mathrm{j}26.38$

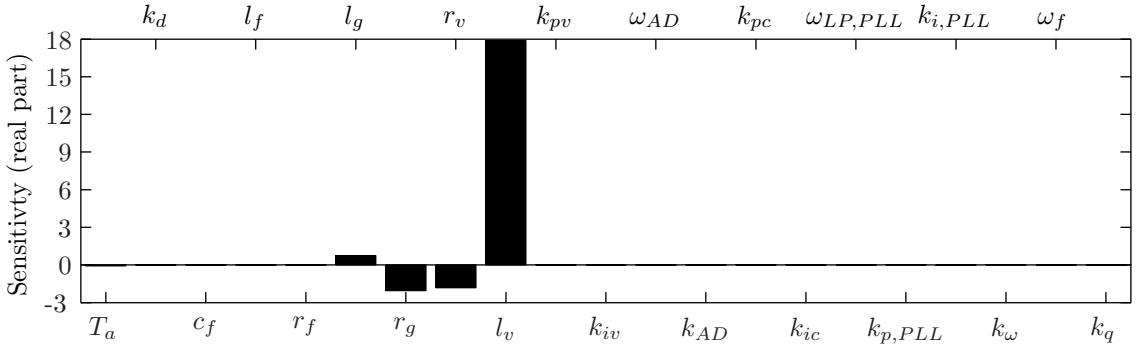

Figure 4.16: *Parametric sensitivity (real part) of VSM mode* $\lambda_{17} \approx -3.691$

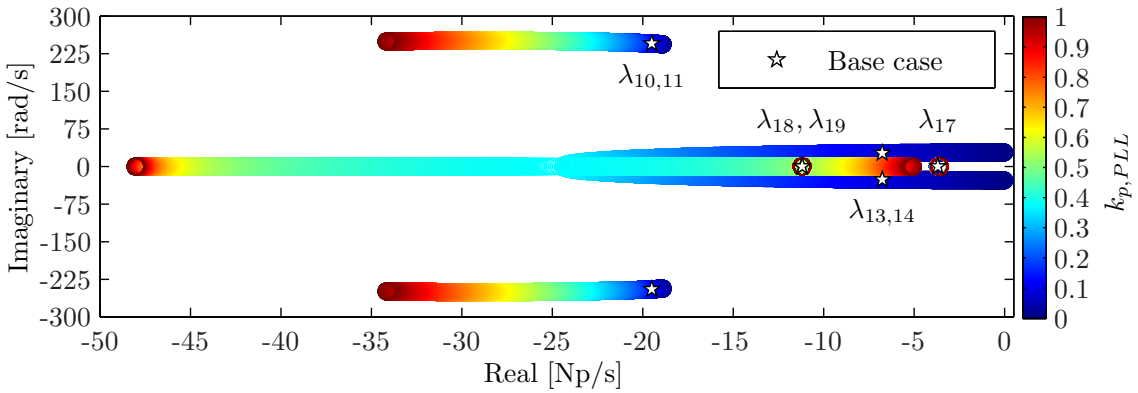

Figure 4.17: *Trace of VSM low-frequency modes for varying PLL proportional gain,* $k_{p,PLL}$

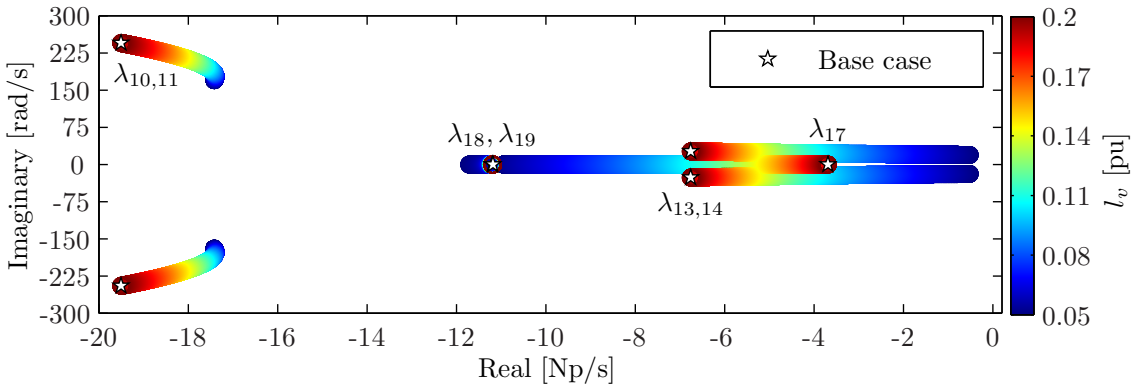

Figure 4.18: *Trace of VSM low-frequency modes for varying virtual inductance, l_v*

q-axis ones. This can be easily observed for modes 1, 9, 15, 16, 18 and 19, and their corresponding main participating state. For this reason and to facilitate reading, each d-axis state has been represented together with its corresponding q-axis state for the complex conjugated eigenvalues, by making use of the complex space vector (CSV) notation (3.1).

Modes 2 to 7, corresponding to the three pairs located at the left end of Figure 4.6, are mainly related to the LCL circuit in the *electrical system*, as indicated in Table 4.4. Just as the SM system, the VSM system has an eigenvalue corresponding to the reactive power measurement low-pass filter at $\lambda \approx -1000$, which relates to the filter cut-off angular frequency. Similarly, the two modes related to the phase lock (phase-locked) loop (PLL) low-pass filters are located at $\lambda \approx -500$, and the two modes related to the active damping low-pass filters are located at $\lambda \approx -50$, which correspond to the filters cut-off angular frequencies.

Apparent decoupling stands out between the swing equation states in $\lambda_{12}, \lambda_{17}$, as opposed to those of the SM system. Moreover, significant coupling can be observed between the PLL and the virtual internal voltage phase (angle) differences (displacements), $\delta\theta_{PLL}, \delta\theta_{VSM}$, in $\lambda_{13,14}$ and λ_{17}. These differences can be attributed to the particular implementation of the swing equation and the alignment of the RRF. Coupling can also be observed between the electrical system states and those related to the control outer loops in the other 4 pairs of complex conjugated eigenvalues, on which the electrical system parameters exert considerable influence.

Among the VSM slowest and least damped modes, λ_{18} and λ_{19} correspond to the current control and their position has shown to be limited by the corresponding integral time, k_{pc}/k_{ic}, which is, for the base case, equal to the filter inductors time constant, $l_f/(\omega_b r_f) \approx 0.0894\,\text{s}$. The pair $\lambda_{10,11}$ relates mainly to the reactive power-voltage control outer loops, and, as can be observed by comparing Figures 4.14 to 4.16, is the most sensitive to changes in the reactive power-voltage droop gain, k_q. As shown in [13], increasing k_q moves the pair to the right, towards the imaginary axis, with $k_q > 0.892$ moving it over the axis and causing instability. It can be seen from Figure 4.14 that, besides k_q, the main tunable parameters influencing $\lambda_{10,11}$ are the voltage control proportional gain, k_{pv}, and the virtual inductance, l_v.

$\lambda_{13,14}$, mainly related to the PLL, is the least damped pair (closest to the origin) and

thus dominates the oscillating component of the system dynamic response. This can be observed in the response of the virtual rotor angular speed, $\omega_{VSM}(t)$, at the right of Figure 4.2, in which the (significantly damped) oscillation has a period of about $2\pi/|\omega_{13,14}| \approx 0.2382\,\text{s}$. It can be seen in Figure 4.15 that l_v and the PLL proportional gain, $k_{p,PLL}$, are the main tunable parameters influencing $\lambda_{13,14}$, and that increasing these parameters moves the pair to the left, increasing its damping. Figure 4.17 shows that increasing $k_{p,PLL}$ also moves $\lambda_{10,11}$ to the left, and reduces the magnitude of the imaginary part of $\lambda_{13,14}$ until the pair enters the real axis, splitting into two purely real modes, at around $k_{p,PLL} \approx 0.3763$. Furthermore, its negligible influence on modes 17 to 19 indicates that such variation can increase the damping of oscillations and the system robustness against parameter variations, without reducing the speed of its response.

The unidirectional component of the system dynamic response is dominated by the slowest (real) mode: λ_{17}, and has a time constant of $-1/\sigma_{17} \approx 0.2709\,\text{s}$, which can be seen in the responses at the right of Figures 4.1 and 4.2. It can be seen in Figure 4.16 that λ_7 is most sensitive to changes in l_v, in the opposite direction of $\lambda_{10,11}$ and $\lambda_{13,14}$. As depicted in Figure 4.18, this implies a trade-off in the placement of the dominant modes: increasing l_v improves the damping of oscillations and the robustness to changes in k_q, as it moves $\lambda_{13,14}$ (and $\lambda_{10,11}$) to the left, while making the system response slower, as it moves λ_{17} to the right. As mentioned in [12] and shown in Figure 4.16, the other parameters have a much smaller influence on λ_{17}, which makes it unlikely to cause instability in the system, and thus not as critical as $\lambda_{10,11}$ or $\lambda_{13,14}$, for instance. Nevertheless, it can be concluded, from Figures 4.17 and 4.18, that a good compromise between speed/performance and robustness/damping of oscillations could be achieved by decreasing l_v and increasing $k_{p,PLL}$, for the base case at least.

Chapter 5

Conclusions and recommendations

5.1 Conclusions

Simulation and analysis of the reference virtual synchronous machine (VSM) implementation in grid-connected mode (VSM system) has been enabled by the corresponding routines and dynamic models created and implemented in the MATLAB programming language and the Simulink graphical block diagramming tool, respectively, within the MATLAB numerical computing integrated environment.

The respective script created in Maple has considerably facilitated the development of the nonlinear state-space analytical model of a traditional power generation unit with a synchronous machine (SM) in grid-connected mode (SM system). The model allows the study of the SM system in similar conditions/context as the VSM system, and facilitates their comparison. Moreover, it can represent the most relevant dynamic characteristics of a round or salient-pole rotor SM, including the amortisseur circuits or the representation of the corresponding damping torque in the swing equation of a reduced-order version of the model. Furthermore, it has been the basis for developing the respective small-signal model. The corresponding routines and dynamic models created in MATLAB and Simulink, respectively, have enabled the simulation and analysis of the SM system.

The SM system small-signal model, developed for any set of inputs and parameter values and any operating (linearisation) point, has enabled the use of linear techniques in the study of the system small-signal stability characteristics. The created Maple script has simplified the development process by allowing the linearisation of the respective nonlinear state-space model analytically/symbolically in an automated manner.

The defined base case and presented dynamic response cases have enabled the reproduction of the the results shown in [13] for the VSM system small-signal model, and have facilitated the comparison of the studied systems. Multiple numerical time-step numerical simulations, performed on different steady-state operating (linearisation) points, have allowed the comparison of the small-signal model dynamic responses with those of the

dynamic (nonlinear) models around the linearisation points. The good match between the responses of the dynamic (nonlinear) models and the corresponding small-signal (linearised) state-space models indicates that the small-signal models accurately represent the investigated systems. This confirms the validity of the small-signal models around the steady-state operating points, and supports their use in the small-signal stability analysis of the systems by traditional linear techniques.

The VSM system dynamic responses to changes in angular frequency or active power present the same general characteristics as those of the SM system. However, since the VSM damping factor, k_d, can be chosen without considering any of the physical constraints in a SM, its high value makes the VSM responses more damped. Despite of all the SM system dynamic (nonlinear) and small-signal (linearised) model dynamic responses presenting an excellent match, the VSM system (linearised) small-signal model cannot represent correctly the dynamic transition to a new operating point with a grid frequency, $\omega_g(t)$, different from that of the linearisation point. This can be attributed to the choice of the virtual rotor angular speed deviation, $\delta\omega_{VSM}(t)$, instead of its angular speed, $\omega_{VSM}(t)$, as a state variable in the VSM system model. The VSM system linearised model is nevertheless able to represent the respective change in the steady-state active power, thanks a contribution from the change in $\omega_g(t)$ through the input matrix, $\mathbf{B}_{VSM}$.

The corresponding script created in Maple has enabled the derivation of expressions for the solution of the SM system nonlinear model equations in steady state. The respective functions developed and implemented in MATLAB for numerically solving and evaluating the expressions have allowed a quick calculation of the linearisation point (initial/steady-state conditions) for any given set of inputs and parameter values. Having an efficient, automated way of computing the steady-state solution has proved important for exploiting the full potential of the small-signal stability analysis by means of linear techniques. However, the need to derive analytical expressions for the steady-state solution of each particular system makes this approach inefficient for the small-signal stability analysis of increasingly bigger, more complex, interconnected systems, as opposed to the numerical methods established for load-flow analysis in traditional power systems.

Obtaining the analytical expressions for the partial derivatives of the SM system small-signal model state matrix with respect to each of the system parameters has enabled the calculation of its parametric sensitivity for any set of parameter values and any operating (linearisation) point. The created Maple script has simplified the process by allowing the analytical/symbolical partial differentiation to be done in an automated manner.

A good command of a computer algebra system like Maple has been essential not only for carrying out the necessary analytical/symbolic manipulation of the equations, but also for evaluating the generated expressions for verification and debugging purposes, and formating them for their implementation in MATLAB functions and for their presentation in this report.

The calculation, for any set of parameter values and any operating (linearisation) point, of the eigenvectors and eigenvalues, and their participation factors and sensitivity to changes in the system parameters has been enabled by the corresponding functions created and implemented in MATLAB. These have constituted the main tool for analysing and comparing the small-signal characteristics of the modelled systems. By iteratively computing

the modes of the respective (small-signal model) state matrices, the stability of the systems has been confirmed for the given base case parameters, with their initial inputs varying within the corresponding intervals. In doing so, the eigenvalues have shown little movement, which suggests that the systems have dynamic responses similar to the base case ones, for the different operating conditions within the operating ranges.

Most of the SM system eigenvalues are slower or not as well damped as the VSM system ones. Moreover, most SM system modes have shown to be relatively fixed and determined mainly by non-tunable system parameters. Among them, the least damped pair, related to the rotor motion (swings), has a damping that, in practise, is considered satisfactory for traditional power systems. As opposed to them, the (complex conjugated eigenvalue) pair corresponding to the SM field circuit has shown significant influence from the reactive power-voltage control loop through the field voltage, v_{fd}, making it more prone to move. Furthermore, the pair constitutes the two critical modes with the highest (most positive) sensitivity to changes in the exciter integral gain, $k_{i,ex}$, which has demonstrated to be the tunning parameter that can most easily cause instability in the SM system. The modelled exciter has shown little capability of increasing the damping of oscillations, and the location of the 4 slowest and least damped eigenvalues has shown to be limited by the non-tunable system parameters, indicating that the SM system performance (dynamic response) or robustness cannot be significantly improved.

Apparent decoupling stands out between the VSM system swing equation states, as opposed to those of the SM system. Moreover, significant coupling has been observed between the VSM phase lock (phase-locked) loop (PLL) and virtual internal voltage phase (angle) differences (displacement), $\delta\theta_{PLL}, \delta\theta_{VSM}$. These differences can be attributed to the particular implementation of the swing equation and the alignment of the corresponding rotating reference frame (RRF). A trade-off has been observed in the placement of the VSM system critical modes: increasing the VSM virtual inductance, l_v, improves the damping of oscillations and the robustness to changes in the parameters, while making the system response slower. However, parametric sweep analysis has indicated that a good compromise between speed/performance and robustness/damping of oscillations could be achieved by decreasing l_v and increasing the VSM PLL proportional gain, $k_{p,PLL}$, for the base case at least.

The inclusion of the grid equivalent impedance in the SM system modelling (SMg system), carried out at a later stage, has enabled a more relevant comparison of the studied systems, particularly with regards to the reactive power-voltage control. In comparison with the SMg system, the VSM system presents a greater difference between the voltage at the point of common coupling (PCC) and the voltage amplitude set-point. Furthermore, it also exhibits a less sensitive response of the reactive power output to a change in the grid voltage amplitude and a smaller steady-state reactive power error. This effect, comparable to that of increasing the VSM reactive power-voltage droop gain, can be attributed to the influence of the virtual impedance in the corresponding control loop. However, as opposed to that of the VSM system, the SM reactive power-voltage droop gain, $k_{q,SM}$, can be increased up to a much greater value without causing instability. This means that, by increasing this gain, the SM(g) system can attain a steady-state reactive power (sharing) error much smaller than that of the VSM system.

In developing the necessary experience to establish reduced-order models for systems with

significant influence from generation interfaced with power electronic converters, this work has contributed by adapting and expanding previous VSM small-signal modelling and analysis to include a SM with a control scheme similar to those of traditional generation units and to the one used in the reference VSM implementation.

5.2 Recommendations for further work

Using a more detailed model of the exciter in the SM system, that includes a power system stabiliser (PSS) would contribute to make a more relevant comparison of the studied systems. Moreover, changing the orientation/alignment of the SM RRF or the VSM RRF to coincide with the other would facilitate the analysis, comparison and manipulation of the corresponding angle differences. This would imply shifting the SM RRF 90° forward, or shifting the VSM RRF 90° backward.

Iterative methods, similar to those established for load-flow analysis in traditional power systems, could be devised or implemented to numerically determine the steady-state solution of the nonlinear equations derived for systems like the studied ones. This would avoid the need to solve the nonlinear equations analytically/symbolically or run time-step simulations iteratively, in analysing the small-signal stability of each new system configuration for varying parameters, inputs and operating points.

Further expansion and interconnection of the developed and implemented models, and further comparison of their small-signal characteristics needs to be done in different conditions, in order to assess their relevance and convenience e.g., whether they provide the right degree of detail. In doing so, the functions provided in MATLAB and Maple for determining the equivalent system representation of interconnected linear models/systems can facilitate the manipulation of the small-signal models already developed for the studied systems. Load dynamics should be included in the eventual modelling and analysis of the systems in islanded operation.

References

[1] Hans-Peter Beck and Ralf Hesse. Virtual synchronous machine. In *Proceedings of the 9th International Conference on Electrical Power Quality and Utilisation (EPQU)*, pages 1–6, Barcelona, Spain, 9-11 October 2007.

[2] Hassan Bevrani, Toshifumi Ise, and Yushi Miura. Virtual synchronous generators: A survey and new perspectives. *International Journal of Electrical Power & Energy Systems*, 54(2014):244–254, January 2014.

[3] Vladimir Blasko and Vikram Kaura. A New Mathematical Model and Control of a Three-Phase AC-DC Voltage Source Converter. *IEEE Transactions on Power Electronics*, 12(1):116–123, January 1997.

[4] Nathaniel Bottrell, Milan Prodanović, and Timothy C. Green. Dynamic Stability of a Microgrid With an Active Load. *IEEE Transactions on Power Electronics*, 28(11):5107–5119, November 2013.

[5] Yong Chen, Ralf Hesse, Dirk Turschner, and Hans-Peter Beck. Dynamic Properties of the Virtual Synchronous Machine (VISMA). In *Proceedings of the International Conference on Renewable Energies and Power Quality (ICREPQ'11)*, Las Palmas, Spain, 13-15 April 2011.

[6] Yong Chen, Ralf Hesse, Dirk Turschner, and Hans-Peter Beck. Investigation of the Virtual Synchronous Machine in the Island Mode. In *Proceedings of the IEEE PES 3rd International Conference on Innovative Smart Grid Technologies (ISGT Europe)*, pages 1–6, Berlin, Germany, 14-17 October 2012.

[7] CIRED Working Group on Smart Grids. Smart Grids on the Distribution Level - Hype or Vision? CIRED's Point of View. Technical report, CIRED, May 2013.

[8] Salvatore D'Arco, Giuseppe Guidi, and Jon Are Suul. Embedded Limitations and Protections for Droop-based Control Schemes with Cascaded Loops in the Synchronous Reference Frame. In *Proceedings of the 2014 International Power Electronics Conference (IPEC-Hiroshima 2014 - ECCE-ASIA)*, pages 1544–1551, Hiroshima, Japan, 18-21 May 2014.

[9] Salvatore D'Arco and Jon Are Suul. Virtual Synchronous Machines – Classification of Implementations and Analysis of Equivalence to Droop Controllers for Microgrids. In *Proceedings of the IEEE PowerTech 2013 Conference*, pages 1–7, Grenoble, France, 16-20 June 2013.

[10] Salvatore D'Arco and Jon Are Suul. Equivalence of Virtual Synchronous Machines and Frequency-Droops for Converter-Based MicroGrids. *IEEE Transactions on Smart Grid*, 5(1):394–395, January 2014.

[11] Salvatore D'Arco, Jon Are Suul, and Olav Bjarte Fosso. Control System Tuning and Stability Analysis of Virtual Synchronous Machines. In *Proceedings of the IEEE 2013 Energy Conversion Congress and Exposition (ECCE)*, pages 2664–2671, Denver, CO, USA, 15-19 September 2013.

[12] Salvatore D'Arco, Jon Are Suul, and Olav Bjarte Fosso. Small-Signal Modelling and Parametric Sensitivity of a Virtual Synchronous Machine. In *Proceedings of the 18th Power Systems Computation Conference (PSCC)*, pages 1–9, Wroclaw, Poland, 18-22 August 2014.

[13] Salvatore D'Arco, Jon Are Suul, and Olav Bjarte Fosso. A Virtual Synchronous Machine implementation for distributed control of power converters in SmartGrids. *Electric Power Systems Research*, 122(2015):180–197, May 2015.

[14] J. Driesen and K. Visscher. Virtual Synchronous Generators. In *Proceedings of the IEEE PES 2008 General Meeting: Conversion and Delivery of Electrical Energy in the 21st Century*, pages 1–3, Pittsburgh, PA, USA, 20-24 July 2008.

[15] Janaka Ekanayake, Lee Holdsworth, and Nick Jenkins. Control of DFIG wind turbines. *Power Engineer*, 17(1):28–32, February 2003.

[16] Janaka Ekanayake and Nick Jenkins. Comparison of the Response of Doubly Fed and Fixed-Speed Induction Generator Wind Turbines to Changes in Network Frequency. *IEEE Transactions on Energy Conversion*, 19(4):800–802, December 2004.

[17] Aboutaleb Haddadi and Geza Joos. Load Sharing of Autonomous Distribution-level Microgrids. In *Proceedings of the IEEE PES 2011 General Meeting: The Electrification of Transportation & The Grid of the Future*, pages 1–9, Detroit, MI, USA, 24-28 July 2011.

[18] Jinwei He and Yun Wei Li. Analysis, Design, and Implementation of Virtual Impedance for Power Electronics Interfaced Distributed Generation. *IEEE Transactions on Industry Applications*, 47(6):2525–2538, November/December 2011.

[19] Ralf Hesse, Dirk Turschner, and Hans-Peter Beck. Micro grid stabilization using the Virtual Synchronous Machine (VISMA). In *Proceedings of the International Conference on Renewable Energies and Power Quality (ICREPQ'09)*, Valencia, Spain, 15-17 April 2009.

[20] Vikram Kaura and Vladimir Blasko. Operation of a Phase Locked Loop System Under Distorted Utility Conditions. *IEEE Transactions on Industry Applications*, 33(1):58–63, January/February 1997.

[21] Helge Kolstad. *Control of an Adjustable Speed Hydro Utilizing Field Programmable Devices*. PhD thesis, Norwegian University of Science and Technology, Trondheim, Norway, 2002.

[22] Benjamin Kroposki, Robert Lasseter, Toshifumi Ise, Satoshi Morozumi, Stavros Papathanassiou, and Nikos Hatziargyriou. Making Microgrids Work. *IEEE Power and Energy Magazine*, 6(3):40–53, May-June 2008.

[23] Natalia Kroutikova, Carlos A. Hernandez-Aramburo, and Timothy C. Green. State-space model of grid-connected inverters under current control mode. *IET Electric Power Applications*, 1(3):329–338, May 2007.

[24] Prabha Kundur. *Power system stability and control*. McGraw-Hill, New York, United States, 1994.

[25] Prabha Kundur, John Paserba, Venkat Ajjarapu, Göran Andersson, Anjan Bose, Claudio Canizares, Nikos Hatziargyriou, David Hill, Alex Stankovic, Carson Taylor, Thierry Van Cutsem, and Vijay Vittal. Definition and Classification of Power System Stability. IEEE/CIGRE Joint Task Force on Stability Terms and Definitions. *IEEE Transactions on Power Systems*, 19(3):1387–1401, August 2004.

[26] Gillian Lalor, Julia Ritchie, Shane Rourke, Damian Flynn, and Mark J. O'Malley. Dynamic Frequency Control with Increasing Wind Generation. In *Proceedings of the IEEE PES 2004 General Meeting*, pages 1715–1720, Denver, CO, United States, 10 June 2004.

[27] Robert H. Lasseter. MicroGrids. In *Proceedings of the IEEE PES 2002 Winter Meeting*, volume 1, pages 305–308, 2002.

[28] Robert H. Lasseter. Microgrids and Distributed Generation. *Journal of Energy Engineering*, 133(3):144–149, September 2007.

[29] Zarchi Linn, Yushi Miura, and Toshifumi Ise. Power System Stabilization Control by HVDC with SMES Using Virtual Synchronous Generator. *IEEJ Journal of Industry Applications*, 1(2):102–110, September 2012.

[30] Jan Machowski, Janusz W. Bialek, and James R. Bumby. *Power system dynamics: stability and control*. John Wiley & Sons, Chichester, United Kingdom, 2nd edition, 2008.

[31] Johan Morren, Jan Pierikb, and Sjoerd W.H. de Haan. Inertial response of variable speed wind turbines. *Electric Power Systems Research*, 76(11):980–987, July 2006.

[32] Nagaraju Pogaku, Milan Prodanović, and Timothy C. Green. Modeling, Analysis and Testing of Autonomous Operation of an Inverter-Based Microgrid. *IEEE Transactions on Power Electronics*, 22(2):613–625, March 2007.

[33] Danny Pudjianto, Charlotte Ramsay, and Goran Strbac. Virtual power plant and system integration of distributed energy resources. *IET Renewable Power Generation*, 1(1):10–16, March 2007.

[34] Joan Rocabert, Alvaro Luna, Frede Blaabjerg, and Pedro Rodríguez. Control of Power Converters in AC Microgrids. *IEEE Transactions on Power Electronics*, 27(11):4734–4749, November 2012.

[35] K. Sakimoto, Y. Miura, and T. Ise. Stabilization of a power system with a distributed generator by a Virtual Synchronous Generator function. In *Proceedings of the IEEE 8th International Conference on Power Electronics and ECCE Asia (ICPE & ECCE)*, pages 1498–1505, Jeju, South Korea, 30 May - 3 June 2011.

[36] Eko Adhi Setiawan. *Concept and controllability of virtual power plant.* PhD thesis, University of Kassel, Kassel, Germany, 2007.

[37] Toshinobu Shintai, Yuushi Miura, and Toshifumi Ise. Reactive power control for load sharing with virtual synchronous generator control. In *Proceedings of the 7th International Power Electronics and Motion Control Conference (IPEMC)*, pages 846–853, Harbin, China, 2-5 June 2012.

[38] M.P.N. van Wesenbeeck, S.W.H. de Haan, P. Varela, and K. Visscher. Grid Tied Converter with Virtual Kinetic Storage. In *Proceedings of the IEEE PowerTech 2009 Conference*, pages 1–7, Bucharest, Romania, 28 June - 2 July 2009.

[39] Tine L. Vandoorn, Brecht Zwaenepoel, Jeroen D.M.De Kooning, Bart Meersman, and Lieven Vandevelde. Smart Microgrids and Virtual Power Plants in a Hierarchical Control Structure. In *Proceedings of the IEEE PES 2nd International Conference on Innovative Smart Grid Technologies (ISGT Europe)*, pages 1–7, Manchester, United Kingdom, 5-7 December 2011.

[40] K. Visscher and S.W.H. de Haan. Virtual synchronous machines (VSG's) for frequency stabilisation in future grids with a significant share of decentralized generation. In *Proceedings of the CIRED 2008 Seminar: SmartGrids for Distribution*, pages 1–4, Frankfurt, Germany, 23-24 June 2008.

[41] Qing-Chang Zhong and George Weiss. Synchronverters: Inverters That Mimic Synchronous Generators. *IEEE Transactions on Industrial Electronics*, 58(4):1259–1267, April 2011.

[42] Jiebei Zhu, Campbell D. Booth, Grain P. Adam, Andrew J. Roscoe, and Chris G. Bright. Inertia Emulation Control Strategy for VSC-HVDC Transmission Systems. *IEEE Transactions on Power Systems*, 28(2):1277–1287, May 2013.

Appendix A

Synchronous machine system mathematical models

A.1 Nonlinear model

Neglecting the term $\frac{\mathrm{d}}{\mathrm{d}t}\omega_g(t)$, equations (3.4)-(3.34) have been reduced in Maple to the nonlinear state-space model given by (A.1)-(A.12).

$$\begin{aligned}\frac{\mathrm{d}}{\mathrm{d}t}i_{SM,d}(t) = &\frac{\omega_b r_a\left(l_{11d}l_{ffd} - {l_{f1d}}^2\right)}{l_{SM,d}}i_{SM,d}(t) - \frac{\omega_b(l_{aq}+l_l)\left(l_{11d}l_{ffd} - {l_{f1d}}^2\right)}{l_{SM,d}}\omega_{SM}(t)i_{SM,q}(t)\\ &+ \frac{\omega_b l_{ad} r_{fd}(l_{11d} - l_{f1d})}{l_{SM,d}}i_{fd}(t) - \frac{\omega_b l_{ad} r_{1d}(l_{f1d} - l_{ffd})}{l_{SM,d}}i_{1d}(t)\\ &+ \frac{\omega_b l_{aq}\left(l_{11d}l_{ffd} - {l_{f1d}}^2\right)}{l_{SM,d}}\omega_{SM}(t)i_{1q}(t) + \frac{\omega_b l_{aq}\left(l_{11d}l_{ffd} - {l_{f1d}}^2\right)}{l_{SM,d}}\omega_{SM}(t)i_{2q}(t)\\ &- \frac{\omega_b l_{ad}(l_{11d} - l_{f1d})}{l_{SM,d}}v_{fd}(t) + \frac{\omega_b\left(l_{11d}l_{ffd} - {l_{f1d}}^2\right)}{l_{SM,d}}\hat{v}_g(t)\cos\left[\delta\theta_{SM}(t)\right]\ ,\end{aligned} \tag{A.1}$$

$$l_{SM,d} = l_{11d}{l_{ad}}^2 - l_{11d}l_{ad}l_{ffd} - l_{11d}l_{ffd}l_l - 2\,{l_{ad}}^2 l_{f1d} + {l_{ad}}^2 l_{ffd} + l_{ad}{l_{f1d}}^2 + {l_{f1d}}^2 l_l$$

$$\begin{aligned}\frac{\mathrm{d}}{\mathrm{d}t}i_{SM,q}(t) = &-\frac{(l_{ad}+l_l)\big(l_{11q}l_{22q}-{l_{aq}}^2\big)\omega_b}{l_{SM,q}}\omega_{SM}(t)i_{SM,d}(t)\\ &-\frac{r_a\big(l_{11q}l_{22q}-{l_{aq}}^2\big)\omega_b}{l_{SM,q}}i_{SM,q}(t)+\frac{l_{ad}\big(l_{11q}l_{22q}-{l_{aq}}^2\big)\omega_b}{l_{SM,q}}\omega_{SM}(t)i_{fd}(t)\\ &+\frac{l_{ad}\big(l_{11q}l_{22q}-{l_{aq}}^2\big)\omega_b}{l_{SM,q}}\omega_{SM}(t)i_{1d}(t)-\frac{l_{aq}r_{1q}(l_{22q}-l_{aq})\omega_b}{l_{SM,q}}i_{1q}(t)\\ &-\frac{l_{aq}r_{2q}(l_{11q}-l_{aq})\omega_b}{l_{SM,q}}i_{2q}(t)+\frac{\big(l_{11q}l_{22q}-{l_{aq}}^2\big)\omega_b}{l_{SM,q}}\hat{v}_g(t)\sin\left[\delta\theta_{SM}(t)\right]\ ,\end{aligned} \tag{A.2}$$

$$l_{SM,q} = l_{11q}l_{22q}l_{aq}+l_{11q}l_{22q}l_l-l_{11q}{l_{aq}}^2-l_{22q}{l_{aq}}^2+{l_{aq}}^3-{l_{aq}}^2l_l$$

$$\begin{aligned}\frac{\mathrm{d}}{\mathrm{d}t}i_{fd}(t) = &\frac{l_{ad}r_a(l_{11d}-l_{f1d})\omega_b}{l_{SM,d}}i_{SM,d}(t)-\frac{l_{ad}(l_{aq}+l_l)(l_{11d}-l_{f1d})\omega_b}{l_{SM,d}}\omega_{SM}(t)i_{SM,q}(t)\\ &+\frac{r_{fd}\big(l_{11d}l_{ad}+l_{11d}l_l-{l_{ad}}^2\big)\omega_b}{l_{SM,d}}i_{fd}(t)+\frac{r_{1d}\big({l_{ad}}^2-l_{ad}l_{f1d}-l_{f1d}l_l\big)\omega_b}{l_{SM,d}}i_{1d}(t)\\ &+\frac{l_{ad}l_{aq}(l_{11d}-l_{f1d})\omega_b}{l_{SM,d}}\omega_{SM}(t)i_{1q}(t)+\frac{l_{ad}l_{aq}(l_{11d}-l_{f1d})\omega_b}{l_{SM,d}}\omega_{SM}(t)i_{2q}(t)\\ &-\frac{\big(l_{11d}l_{ad}+l_{11d}l_l-{l_{ad}}^2\big)\omega_b}{l_{SM,d}}v_{fd}(t)+\frac{\omega_b l_{ad}(l_{11d}-l_{f1d})}{l_{SM,d}}\hat{v}_g(t)\cos\left[\delta\theta_{SM}(t)\right]\end{aligned} \tag{A.3}$$

$$\begin{aligned}\frac{\mathrm{d}}{\mathrm{d}t}i_{1d}(t) = &-\frac{\omega_b l_{ad}r_a(l_{f1d}-l_{ffd})}{l_{SM,d}}i_{SM,d}(t)+\frac{\omega_b l_{ad}(l_{f1d}-l_{ffd})(l_{aq}+l_l)}{l_{SM,d}}\omega_{SM}(t)i_{SM,q}(t)\\ &+\frac{\omega_b r_{fd}\big({l_{ad}}^2-l_{ad}l_{f1d}-l_{f1d}l_l\big)}{l_{SM,d}}i_{fd}(t)-\frac{\omega_b r_{1d}\big({l_{ad}}^2-l_{ffd}l_{ad}-l_{ffd}l_l\big)}{l_{SM,d}}i_{1d}(t)\\ &-\frac{\omega_b l_{ad}l_{aq}(l_{f1d}-l_{ffd})}{l_{SM,d}}\omega_{SM}(t)i_{1q}(t)-\frac{\omega_b l_{ad}l_{aq}(l_{f1d}-l_{ffd})}{l_{SM,d}}\omega_{SM}(t)i_{2q}(t)\\ &-\frac{\omega_b\big({l_{ad}}^2-l_{ad}l_{f1d}-l_{f1d}l_l\big)}{l_{SM,d}}v_{fd}(t)-\frac{(l_{f1d}-l_{ffd})l_{ad}\omega_b}{l_{SM,d}}\hat{v}_g(t)\cos\left[\delta\theta_{SM}(t)\right]\end{aligned} \tag{A.4}$$

$$\begin{aligned}\frac{\mathrm{d}}{\mathrm{d}t}i_{1q}(t) = &-\frac{\omega_b l_{aq}(l_{ad}+l_l)(l_{22q}-l_{aq})}{l_{SM,q}}\omega_{SM}(t)i_{SM,d}(t)\\ &-\frac{\omega_b l_{aq}r_a(l_{22q}-l_{aq})}{l_{SM,q}}i_{SM,q}(t)+\frac{\omega_b l_{ad}l_{aq}(l_{22q}-l_{aq})}{l_{SM,q}}\omega_{SM}(t)i_{fd}(t)\\ &+\frac{\omega_b l_{ad}l_{aq}(l_{22q}-l_{aq})}{l_{SM,q}}\omega_{SM}(t)i_{1d}(t)-\frac{\omega_b r_{1q}\big(l_{22q}l_{aq}+l_{22q}l_l-{l_{aq}}^2\big)}{l_{SM,q}}i_{1q}(t)\\ &+\frac{\omega_b l_{aq}l_l r_{2q}}{l_{SM,q}}i_{2q}(t)+\frac{\omega_b l_{aq}(l_{22q}-l_{aq})}{l_{SM,q}}\hat{v}_g(t)\sin\left[\delta\theta_{SM}(t)\right]\end{aligned} \tag{A.5}$$

$$\begin{aligned}\frac{\mathrm{d}}{\mathrm{d}t}i_{2q}(t) = &-\frac{\omega_b l_{aq}(l_{ad}+l_l)(l_{11q}-l_{aq})}{l_{SM,q}}\omega_{SM}(t)i_{SM,d}(t)\\ &-\frac{\omega_b l_{aq} r_a (l_{11q}-l_{aq})}{l_{SM,q}}i_{SM,q}(t)+\frac{\omega_b l_{ad} l_{aq}(l_{11q}-l_{aq})}{l_{SM,q}}\omega_{SM}(t)i_{fd}(t)\\ &+\frac{\omega_b l_{ad} l_{aq}(l_{11q}-l_{aq})}{l_{SM,q}}\omega_{SM}(t)i_{1d}(t)+\frac{\omega_b l_{aq} l_l r_{1q}}{l_{SM,q}}i_{1q}(t)\\ &-\frac{\omega_b r_{2q}\left(l_{11q}l_{aq}+l_{11q}l_l-{l_{aq}}^2\right)}{l_{SM,q}}i_{2q}(t)+\frac{\omega_b l_{aq}(l_{11q}-l_{aq})}{l_{SM,q}}\hat{v}_g(t)\sin\left[\delta\theta_{SM}(t)\right]\end{aligned} \tag{A.6}$$

$$\begin{aligned}\frac{\mathrm{d}}{\mathrm{d}t}\omega_{SM}(t) \approx &\frac{l_{ad}-l_{aq}}{T_{SM}}i_{SM,q}(t)i_{SM,d}(t)+\frac{l_{aq}}{T_{SM}}i_{1q}(t)i_{SM,d}(t)\\ &+\frac{l_{aq}}{T_{SM}}i_{2q}(t)i_{SM,d}(t)-\frac{l_{ad}}{T_{SM}}i_{fd}(t)i_{SM,q}(t)-\frac{l_{ad}}{T_{SM}}i_{1d}(t)i_{SM,q}(t)\\ &-\frac{k_{d,SM}}{T_{SM}}\omega_{SM}(t)+\frac{k_{d,SM}}{T_{SM}}\omega_g(t)+\frac{1}{T_{SM}}\frac{p_{m,SM}(t)}{\omega_{SM}(t)}\end{aligned} \tag{A.7}$$

$$\frac{\mathrm{d}}{\mathrm{d}t}\delta\theta_{SM}(t) = \omega_b\omega_{SM}(t)-\omega_b\omega_g(t) \tag{A.8}$$

$$\frac{\mathrm{d}}{\mathrm{d}t}p_{m,SM}(t) = -\frac{k_{\omega,SM}}{T_{gt}}\omega_{SM}(t)-\frac{1}{T_{gt}}p_{m,SM}(t)+\frac{1}{T_{gt}}p^*_{SM}(t)+\frac{k_{\omega,SM}}{T_{gt}}\omega^*_{SM}(t) \tag{A.9}$$

$$\begin{aligned}\frac{\mathrm{d}}{\mathrm{d}t}q_{m,SM}(t) = &-\omega_{f,SM}i_{SM,d}(t)\hat{v}_g(t)\sin\left[\delta\theta_{SM}(t)\right]\\ &-\omega_{f,SM}i_{SM,q}(t)\hat{v}_g(t)\cos\left[\delta\theta_{SM}(t)\right]-\omega_{f,SM}q_{m,SM}(t)\end{aligned} \tag{A.10}$$

$$\frac{\mathrm{d}}{\mathrm{d}t}\zeta(t) = -k_{q,SM}q_{m,SM}(t)-\hat{v}_g(t)+\hat{v}^*_{SM}(t)+k_{q,SM}q^*_{SM}(t) \tag{A.11}$$

$$\begin{aligned}\frac{\mathrm{d}}{\mathrm{d}t}v_{fd}(t) = &-\frac{k_{p,ex}k_{q,SM}}{T_{ex}}q_{m,SM}(t)+\frac{k_{i,ex}}{T_{ex}}\zeta(t)-\frac{1}{T_{ex}}v_{fd}(t)\\ &-\frac{k_{p,ex}}{T_{ex}}\hat{v}_g(t)+\frac{k_{p,ex}}{T_{ex}}\hat{v}^*_{SM}(t)+\frac{k_{p,ex}k_{q,SM}}{T_{ex}}q^*_{SM}(t)\end{aligned} \tag{A.12}$$

A.2 Small-signal model

By linearisation of the nonlinear model (A.1)-(A.12), the small-signal state-space model has been derived in Maple, with the form given by (A.13), where $\mathbf{x}_{SM}(t)$ is state vector (A.14), $\mathbf{u}_{SM}$(t) is the input vector (A.15), $\mathbf{A}_{SM}$ is the state (system, dynamic) matrix, $\mathbf{B}_{SM}(t)$ is the input matrix (A.21) and the prefix Δ indicates small-signal deviations around the steady-state operating point [13, 24], $t = 0$. For convenience of notation, $\mathbf{A}_{SM}$ is expressed through 4 sub-matrices (A.17)-(A.20), according to (A.16).

$$\boldsymbol{\Delta}\dot{\mathbf{x}}_{SM}(t) \doteq \frac{\mathrm{d}}{\mathrm{d}t}\boldsymbol{\Delta}\mathbf{x}_{SM}(t) = \mathbf{A}_{SM}\boldsymbol{\Delta}\mathbf{x}_{SM}(t) + \mathbf{B}_{SM}\boldsymbol{\Delta}\mathbf{u}_{SM}(t) \tag{A.13}$$

$$\begin{aligned}\mathbf{x}_{SM}(t) \doteq [&i_{SM,d}(t)\ i_{SM,q}(t)\ i_{fd}(t)\ i_{1d}(t)\ i_{1q}(t)\ i_{2q}(t)\ \cdots \\ &\cdots\ \omega_{SM}(t)\ \delta\theta_{SM}(t)\ p_{m,SM}(t)\ q_{m,SM}(t)\ \zeta(t)\ v_{fd}(t)]^T\end{aligned} \tag{A.14}$$

$$\mathbf{u}_{SM}(t) \doteq [\hat{v}_g(t)\ p^*_{SM}(t)\ \hat{v}^*_{SM}(t)\ q^*_{SM}(t)\ \omega^*_{SM}(t)\ \omega_g(t)]^T \tag{A.15}$$

$$\begin{aligned}\begin{bmatrix}\boldsymbol{\Delta}\dot{\mathbf{x}}_{SM,1}(t)\\ \boldsymbol{\Delta}\dot{\mathbf{x}}_{SM,2}(t)\\ \boldsymbol{\Delta}\dot{\mathbf{x}}_{SM,3}(t)\\ \boldsymbol{\Delta}\dot{\mathbf{x}}_{SM,4}(t)\end{bmatrix} &= \begin{bmatrix}\mathbf{A}_{SM,1} & \mathbf{A}_{SM,2} & \mathbf{A}_{SM,3} & \mathbf{A}_{SM,4}\end{bmatrix}\begin{bmatrix}\boldsymbol{\Delta}\mathbf{x}_{SM,1}(t)\\ \boldsymbol{\Delta}\mathbf{x}_{SM,2}(t)\\ \boldsymbol{\Delta}\mathbf{x}_{SM,3}(t)\\ \boldsymbol{\Delta}\mathbf{x}_{SM,4}(t)\end{bmatrix} \\ &\quad + \mathbf{B}_{SM}\boldsymbol{\Delta}\mathbf{u}_{SM}(t)\end{aligned} \tag{A.16}$$

$$\mathbf{A}_{SM,1} = \left[\begin{array}{c|c|c} \frac{\omega_b r_a\left(l_{11d} l_{ffd} - {l_{f1d}}^2\right)}{l_{SM,d}} & -\frac{\omega_b (l_{aq}+l_l)\left(l_{11d} l_{ffd} - {l_{f1d}}^2\right)\omega_{SM}(0)}{l_{SM,d}} & \frac{\omega_b l_{ad} r_{fd}\left(l_{11d} - l_{f1d}\right)}{l_{SM,d}} \\ -\frac{(l_{ad}+l_l)\left(l_{11q} l_{22q} - {l_{aq}}^2\right)\omega_b \omega_{SM}(0)}{l_{SM,q}} & -\frac{r_a\left(l_{11q} l_{22q} - {l_{aq}}^2\right)\omega_b}{l_{SM,q}} & \frac{l_{ad}\left(l_{11q} l_{22q} - {l_{aq}}^2\right)\omega_b \omega_{SM}(0)}{l_{SM,q}} \\ \frac{l_{ad} r_a\left(l_{11d} - l_{f1d}\right)\omega_b}{l_{SM,d}} & -\frac{l_{ad}(l_{aq}+l_l)\left(l_{11d} - l_{f1d}\right)\omega_b \omega_{SM}(0)}{l_{SM,d}} & \frac{r_{fd}\left(l_{11d} l_{ad} + l_{11d} l_l - {l_{ad}}^2\right)\omega_b}{l_{SM,d}} \\ -\frac{\omega_b l_{ad} r_a\left(l_{f1d} - l_{ffd}\right)}{l_{SM,d}} & \frac{\omega_b l_{ad}\left(l_{f1d} - l_{ffd}\right)(l_{aq}+l_l)\omega_{SM}(0)}{l_{SM,d}} & \frac{\omega_b r_{fd}\left({l_{ad}}^2 - l_{ad} l_{f1d} - l_{f1d} l_l\right)}{l_{SM,d}} \\ -\frac{\omega_b l_{aq}(l_{ad}+l_l)(l_{22q} - l_{aq})\omega_{SM}(0)}{l_{SM,q}} & -\frac{\omega_b l_{aq} r_a (l_{22q} - l_{aq})}{l_{SM,q}} & \frac{\omega_b l_{ad} l_{aq}(l_{22q} - l_{aq})\omega_{SM}(0)}{l_{SM,q}} \\ -\frac{\omega_b l_{aq}(l_{ad}+l_l)(l_{11q} - l_{aq})\omega_{SM}(0)}{l_{SM,q}} & -\frac{\omega_b l_{aq} r_a (l_{11q} - l_{aq})}{l_{SM,q}} & \frac{\omega_b l_{ad} l_{aq}(l_{11q} - l_{aq})\omega_{SM}(0)}{l_{SM,q}} \\ \frac{l_{ad} i_{SM,q}(0) - l_{aq} i_{SM,q}(0) + l_{aq} i_{1q}(0) + l_{aq} i_{2q}(0)}{T_{SM}} & -\frac{-l_{ad} i_{SM,d}(0) + l_{aq} i_{SM,d}(0) + l_{ad} i_{fd}(0) + l_{ad} i_{1d}(0)}{T_{SM}} & -\frac{l_{ad} i_{SM,q}(0)}{T_{SM}} \\ 0 & 0 & 0 \\ 0 & 0 & 0 \\ -\omega_{f,SM} \sin\left[\delta\theta_{SM}(0)\right]\hat{v}_g(0) & -\omega_{f,SM} \cos\left[\delta\theta_{SM}(0)\right]\hat{v}_g(0) & 0 \\ 0 & 0 & 0 \\ 0 & 0 & 0 \end{array}\right] \tag{A.17}$$

$$
\mathbf{A}_{SM,2} = \begin{bmatrix}
-\frac{\omega_b l_{aq} r_{1d} \left(l_{f1d} - l_{ffd}\right)}{l_{SM,d}} & \frac{\omega_b l_{aq} \left(l_{11d} l_{ffd} - l_{f1d}{}^2\right) \omega_{SM}(0)}{l_{SM,d}} & \frac{\omega_b l_{aq} \left(l_{11d} l_{ffd} - l_{f1d}{}^2\right) \omega_{SM}(0)}{l_{SM,d}} \\
\frac{l_{ad} \left(l_{11q} l_{22q} - l_{aq}{}^2\right) \omega_b \omega_{SM}(0)}{l_{SM,q}} & -\frac{l_{aq} r_{1q} \left(l_{22q} - l_{aq}\right) \omega_b}{l_{SM,q}} & -\frac{l_{aq} r_{2q} \left(l_{11q} - l_{aq}\right) \omega_b}{l_{SM,q}} \\
\frac{r_{1d} \left(l_{ad}{}^2 - l_{ad} l_{f1d} - l_{f1d} l_l\right) \omega_b}{l_{SM,d}} & \frac{l_{ad} l_{aq} \left(l_{11d} - l_{f1d}\right) \omega_b \omega_{SM}(0)}{l_{SM,d}} & \frac{l_{ad} l_{aq} \left(l_{11d} - l_{f1d}\right) \omega_b \omega_{SM}(0)}{l_{SM,d}} \\
-\frac{\omega_b r_{1d} \left(l_{ad}{}^2 - l_{ffd} l_{ad} - l_{ffd} l_l\right)}{l_{SM,d}} & -\frac{\omega_b l_{ad} l_{aq} \left(l_{f1d} - l_{ffd}\right) \omega_{SM}(0)}{l_{SM,d}} & -\frac{\omega_b l_{ad} l_{aq} \left(l_{f1d} - l_{ffd}\right) \omega_{SM}(0)}{l_{SM,d}} \\
\frac{\omega_b l_{ad} l_{aq} \left(l_{22q} - l_{aq}\right) \omega_{SM}(0)}{l_{SM,q}} & -\frac{\omega_b r_{1q} \left(l_{22q} l_{aq} + l_{22q} l_l - l_{aq}{}^2\right)}{l_{SM,q}} & \frac{\omega_b l_{aq} l_l r_{2q}}{l_{SM,q}} \\
\frac{\omega_b l_{ad} l_{aq} \left(l_{11q} - l_{aq}\right) \omega_{SM}(0)}{l_{SM,q}} & \frac{\omega_b l_{aq} l_l r_{1q}}{l_{SM,q}} & -\frac{\omega_b r_{2q} \left(l_{11q} l_{aq} + l_{11q} l_l - l_{aq}{}^2\right)}{l_{SM,q}} \\
-\frac{l_{ad} i_{SM,q}(0)}{T_{SM}} & \frac{l_{aq} i_{SM,d}(0)}{T_{SM}} & \frac{l_{aq} i_{SM,d}(0)}{T_{SM}} \\
0 & 0 & 0 \\
0 & 0 & 0 \\
0 & 0 & 0 \\
0 & 0 & 0 \\
0 & 0 & 0
\end{bmatrix} \tag{A.18}
$$

$$\mathbf{A}_{SM,3} = \left[\begin{array}{c|c} \frac{\omega_b\left(l_{11d}l_{ffd}-{l_{f1d}}^2\right)\left[-l_{aq}i_{SM,q}(0)-l_l i_{SM,q}(0)+l_{aq}i_{1q}(0)+l_{aq}i_{2q}(0)\right]}{l_{SM,d}} & -\frac{\omega_b \sin\left[\delta\theta_{SM}(0)\right]\left(l_{11d}l_{ffd}-{l_{f1d}}^2\right)\hat{v}_g(0)}{l_{SM,d}} \\ \frac{\left(l_{11q}l_{22q}-{l_{aq}}^2\right)\omega_b\left[-l_{ad}i_{SM,d}(0)-l_l i_{SM,d}(0)+l_{ad}i_{fd}(0)+l_{ad}i_{1d}(0)\right]}{l_{SM,q}} & \frac{\cos\left[\delta\theta_{SM}(0)\right]\left(l_{11q}l_{22q}-{l_{aq}}^2\right)\omega_b\hat{v}_g(0)}{l_{SM,q}} \\ \frac{\omega_b l_{ad}\left(l_{11d}-l_{f1d}\right)\left[-l_{aq}i_{SM,q}(0)-l_l i_{SM,q}(0)+l_{aq}i_{1q}(0)+l_{aq}i_{2q}(0)\right]}{l_{SM,d}} & -\frac{\sin\left[\delta\theta_{SM}(0)\right]l_{ad}\left(l_{11d}-l_{f1d}\right)\omega_b\hat{v}_g(0)}{l_{SM,d}} \\ -\frac{\left(l_{f1d}-l_{ffd}\right)l_{ad}\omega_b\left[-l_{aq}i_{SM,q}(0)-l_l i_{SM,q}(0)+l_{aq}i_{1q}(0)+l_{aq}i_{2q}(0)\right]}{l_{SM,d}} & \frac{\omega_b \sin\left[\delta\theta_{SM}(0)\right]l_{ad}\left(l_{f1d}-l_{ffd}\right)\hat{v}_g(0)}{l_{SM,d}} \\ \frac{\omega_b l_{aq}(l_{22q}-l_{aq})\left[-l_{ad}i_{SM,d}(0)-l_l i_{SM,d}(0)+l_{ad}i_{fd}(0)+l_{ad}i_{1d}(0)\right]}{l_{SM,q}} & \frac{\omega_b \cos\left[\delta\theta_{SM}(0)\right]l_{aq}(l_{22q}-l_{aq})\hat{v}_g(0)}{l_{SM,q}} \\ \frac{\omega_b l_{aq}(l_{11q}-l_{aq})\left[-l_{ad}i_{SM,d}(0)-l_l i_{SM,d}(0)+l_{ad}i_{fd}(0)+l_{ad}i_{1d}(0)\right]}{l_{SM,q}} & \frac{\omega_b \cos\left[\delta\theta_{SM}(0)\right]l_{aq}(l_{11q}-l_{aq})\hat{v}_g(0)}{l_{SM,q}} \\ -\frac{k_{d,SM}\omega_{SM}^2(0)+p_{m,SM}(0)}{T_{SM}\omega_{SM}^2(0)} & 0 \\ \omega_b & 0 \\ -\frac{k_{\omega,SM}}{T_{gt}} & 0 \\ 0 & \omega_{f,SM}\left\{-\cos\left[\delta\theta_{SM}(0)\right]i_{SM,d}(0)+\sin\left[\delta\theta_{SM}(0)\right]i_{SM,q}(0)\right\}\hat{v}_g(0) \\ 0 & 0 \\ 0 & 0 \end{array}\right] \tag{A.19}$$

$$\mathbf{A}_{SM,4} = \left[\begin{array}{c|c|c|c}
0 & 0 & 0 & -\frac{\omega_b l_{ad}\left(l_{11d}-l_{f1d}\right)}{l_{SM,d}} \\
0 & 0 & 0 & 0 \\
0 & 0 & 0 & -\frac{\left(l_{11d}l_{ad}+l_{11d}l_l-{l_{ad}}^2\right)\omega_b}{l_{SM,d}} \\
0 & 0 & 0 & -\frac{\omega_b\left({l_{ad}}^2-l_{ad}l_{f1d}-l_{f1d}l_l\right)}{l_{SM,d}} \\
0 & 0 & 0 & 0 \\
0 & 0 & 0 & 0 \\
\frac{1}{T_{SM}\omega_{SM}(0)} & 0 & 0 & 0 \\
0 & 0 & 0 & 0 \\
-{T_{gt}}^{-1} & 0 & 0 & 0 \\
0 & -\omega_{f,SM} & 0 & 0 \\
0 & -k_{q,SM} & 0 & 0 \\
0 & -\frac{k_{p,ex}k_{q,SM}}{T_{ex}} & \frac{k_{i,ex}}{T_{ex}} & -{T_{ex}}^{-1}
\end{array}\right] \tag{A.20}$$

$$\mathbf{B}_{SM} = \left[\begin{array}{c|c|c|c|c|c} \frac{\omega_b \cos[\delta\theta_{SM}(0)]\left(l_{11d} l_{ffd} - {l_{f1d}}^2\right)}{l_{SM,d}} & 0 & 0 & 0 & 0 & 0 \\ \frac{\sin[\delta\theta_{SM}(0)]\left(l_{11q} l_{22q} - {l_{aq}}^2\right)\omega_b}{l_{SM,q}} & 0 & 0 & 0 & 0 & 0 \\ \frac{\cos[\delta\theta_{SM}(0)] l_{ad}\left(l_{11d} - l_{f1d}\right)\omega_b}{l_{SM,d}} & 0 & 0 & 0 & 0 & 0 \\ -\frac{\omega_b \cos[\delta\theta_{SM}(0)] l_{ad}\left(l_{f1d} - l_{ffd}\right)}{l_{SM,d}} & 0 & 0 & 0 & 0 & 0 \\ -\frac{\omega_b \sin[\delta\theta_{SM}(0)] l_{aq}(-l_{22q} + l_{aq})}{l_{SM,q}} & 0 & 0 & 0 & 0 & 0 \\ \frac{\omega_b \sin[\delta\theta_{SM}(0)] l_{aq}(l_{11q} - l_{aq})}{l_{SM,q}} & 0 & 0 & 0 & 0 & 0 \\ 0 & 0 & 0 & 0 & 0 & \frac{k_{d,SM}}{T_{SM}} \\ 0 & 0 & 0 & 0 & 0 & -\omega_b \\ 0 & {T_{gt}}^{-1} & 0 & 0 & \frac{k_{\omega,SM}}{T_{gt}} & 0 \\ -\omega_{f,SM}\left\{\sin[\delta\theta_{SM}(0)] i_{SM,d}(0) + \cos[\delta\theta_{SM}(0)] i_{SM,q}(0)\right\} & 0 & 0 & 0 & 0 & 0 \\ -1 & 0 & 1 & k_{q,SM} & 0 & 0 \\ -\frac{k_{p,ex}}{T_{ex}} & 0 & \frac{k_{p,ex}}{T_{ex}} & \frac{k_{p,ex} k_{q,SM}}{T_{ex}} & 0 & 0 \end{array}\right] \tag{A.21}$$

Appendix B

SM system plus grid equivalent impedance mathematical models

B.1 Nonlinear model

Neglecting the term $\frac{\mathrm{d}}{\mathrm{d}t}\omega_g(t)$, equations (3.4)-(3.34),(3.38),(3.39), have been reduced in Maple to the nonlinear state-space model given by (B.1)-(B.16).

$$\frac{\mathrm{d}}{\mathrm{d}t}v_{SM,d}(t) = \omega_b\omega_g(t)v_{SM,q}(t) - \frac{\omega_b}{c_{mg}}i_{o,SM,d}(t) + \frac{\omega_b}{c_{mg}}i_{SM,d}(t) \tag{B.1}$$

$$\frac{\mathrm{d}}{\mathrm{d}t}v_{SM,q}(t) = -\omega_b\omega_g(t)v_{SM,d}(t) - \frac{\omega_b}{c_{mg}}i_{o,SM,q}(t) + \frac{\omega_b}{c_{mg}}i_{SM,q}(t) \tag{B.2}$$

$$\frac{\mathrm{d}}{\mathrm{d}t}i_{o,SM,d}(t) = \frac{\omega_b}{l_{mg}}v_{SM,d}(t) + \omega_b\omega_g(t)i_{o,SM,q}(t) - \frac{r_{mg}\omega_b}{l_{mg}}i_{o,SM,d}(t) - \frac{\omega_b}{l_{mg}}\hat{v}_g(t)\cos\left[\delta\theta_{SM}(t)\right] \tag{B.3}$$

$$\frac{\mathrm{d}}{\mathrm{d}t}i_{o,SM,q}(t) = \frac{\omega_b}{l_{mg}}v_{SM,q}(t) - \omega_b\omega_g(t)i_{o,SM,d}(t) - \frac{r_{mg}\omega_b}{l_{mg}}i_{o,SM,q}(t) + \frac{\omega_b}{l_{mg}}\hat{v}_g(t)\sin\left[\delta\theta_{SM}(t)\right] \tag{B.4}$$

$$\begin{aligned}\frac{\mathrm{d}}{\mathrm{d}t}i_{SM,d}(t) = &\frac{\omega_b\left(l_{11d}l_{ffd} - {l_{f1d}}^2\right)}{l_{SM,d}}v_{SM,d}(t) + \frac{\omega_b r_a\left(l_{11d}l_{ffd} - {l_{f1d}}^2\right)}{l_{SM,d}}i_{SM,d}(t)\\ &- \frac{\omega_b(l_{aq}+l_l)\left(l_{11d}l_{ffd} - {l_{f1d}}^2\right)}{l_{SM,d}}\omega_{SM}(t)i_{SM,q}(t) + \frac{\omega_b l_{ad}r_{fd}(l_{11d}-l_{f1d})}{l_{SM,d}}i_{fd}(t)\\ &- \frac{\omega_b l_{ad}r_{1d}(l_{f1d}-l_{ffd})}{l_{SM,d}}i_{1d}(t) + \frac{\omega_b l_{aq}\left(l_{11d}l_{ffd} - {l_{f1d}}^2\right)}{l_{SM,d}}\omega_{SM}(t)i_{1q}(t)\\ &+ \frac{\omega_b l_{aq}\left(l_{11d}l_{ffd} - {l_{f1d}}^2\right)}{l_{SM,d}}\omega_{SM}(t)i_{2q}(t) - \frac{\omega_b l_{ad}(l_{11d}-l_{f1d})}{l_{SM,d}}v_{fd}(t)\end{aligned} \tag{B.5}$$

$$\begin{aligned}\frac{\mathrm{d}}{\mathrm{d}t}i_{SM,q}(t) = &-\frac{\left(l_{11q}l_{22q} - {l_{aq}}^2\right)\omega_b}{l_{SM,q}}v_{SM,q}(t) - \frac{(l_{ad}+l_l)\left(l_{11q}l_{22q} - {l_{aq}}^2\right)\omega_b}{l_{SM,q}}\omega_{SM}(t)i_{SM,d}(t)\\ &- \frac{r_a\left(l_{11q}l_{22q} - {l_{aq}}^2\right)\omega_b}{l_{SM,q}}i_{SM,q}(t) + \frac{l_{ad}\left(l_{11q}l_{22q} - {l_{aq}}^2\right)\omega_b}{l_{SM,q}}\omega_{SM}(t)i_{fd}(t)\\ &+ \frac{l_{ad}\left(l_{11q}l_{22q} - {l_{aq}}^2\right)\omega_b}{l_{SM,q}}\omega_{SM}(t)i_{1d}(t)\\ &- \frac{l_{aq}r_{1q}(l_{22q}-l_{aq})\omega_b}{l_{SM,q}}i_{1q}(t) - \frac{l_{aq}r_{2q}(l_{11q}-l_{aq})\omega_b}{l_{SM,q}}i_{2q}(t)\end{aligned} \tag{B.6}$$

$$\begin{aligned}\frac{\mathrm{d}}{\mathrm{d}t}i_{fd}(t) = &\frac{\omega_b l_{ad}(l_{11d}-l_{f1d})}{l_{SM,d}}v_{SM,d}(t) + \frac{l_{ad}r_a(l_{11d}-l_{f1d})\omega_b}{l_{SM,d}}i_{SM,d}(t)\\ &- \frac{l_{ad}(l_{aq}+l_l)(l_{11d}-l_{f1d})\omega_b}{l_{SM,d}}\omega_{SM}(t)i_{SM,q}(t)\\ &+ \frac{r_{fd}\left(l_{11d}l_{ad} + l_{11d}l_l - {l_{ad}}^2\right)\omega_b}{l_{SM,d}}i_{fd}(t)\\ &+ \frac{r_{1d}\left({l_{ad}}^2 - l_{ad}l_{f1d} - l_{f1d}l_l\right)\omega_b}{l_{SM,d}}i_{1d}(t) + \frac{l_{ad}l_{aq}(l_{11d}-l_{f1d})\omega_b}{l_{SM,d}}\omega_{SM}(t)i_{1q}(t)\\ &+ \frac{l_{ad}l_{aq}(l_{11d}-l_{f1d})\omega_b}{l_{SM,d}}\omega_{SM}(t)i_{2q}(t) - \frac{\left(l_{11d}l_{ad} + l_{11d}l_l - {l_{ad}}^2\right)\omega_b}{l_{SM,d}}v_{fd}(t)\end{aligned} \tag{B.7}$$

$$\begin{aligned}\frac{\mathrm{d}}{\mathrm{d}t}i_{1d}(t) = &-\frac{\omega_b l_{ad}(l_{f1d}-l_{ffd})}{l_{SM,d}}v_{SM,d}(t) - \frac{\omega_b l_{ad} r_a (l_{f1d}-l_{ffd})}{l_{SM,d}}i_{SM,d}(t)\\ &+\frac{\omega_b l_{ad}(l_{f1d}-l_{ffd})(l_{aq}+l_l)}{l_{SM,d}}\omega_{SM}(t)i_{SM,q}(t)\\ &+\frac{\omega_b r_{fd}\left({l_{ad}}^2 - l_{ad}l_{f1d} - l_{f1d}l_l\right)}{l_{SM,d}}i_{fd}(t)\\ &-\frac{\omega_b r_{1d}\left({l_{ad}}^2 - l_{ffd}l_{ad} - l_{ffd}l_l\right)}{l_{SM,d}}i_{1d}(t) - \frac{\omega_b l_{ad} l_{aq}(l_{f1d}-l_{ffd})}{l_{SM,d}}\omega_{SM}(t)i_{1q}(t)\\ &-\frac{\omega_b l_{ad} l_{aq}(l_{f1d}-l_{ffd})}{l_{SM,d}}\omega_{SM}(t)i_{2q}(t) - \frac{\omega_b\left({l_{ad}}^2 - l_{ad}l_{f1d} - l_{f1d}l_l\right)}{l_{SM,d}}v_{fd}(t)\end{aligned} \tag{B.8}$$

$$\begin{aligned}\frac{\mathrm{d}}{\mathrm{d}t}i_{1q}(t) = &-\frac{\omega_b l_{aq}(l_{ad}+l_l)(l_{22q}-l_{aq})i_{SM,d}(t)}{l_{SM,q}}\omega_{SM}(t)\\ &+\frac{\omega_b l_{ad} l_{aq}(l_{22q}-l_{aq})i_{fd}(t)}{l_{SM,q}}\omega_{SM}(t) + \frac{\omega_b l_{ad} l_{aq}(l_{22q}-l_{aq})i_{1d}(t)}{l_{SM,q}}\omega_{SM}(t)\\ &-\frac{\omega_b l_{aq}(l_{22q}-l_{aq})}{l_{SM,q}}v_{SM,q}(t) - \frac{\omega_b l_{aq} r_a (l_{22q}-l_{aq})}{l_{SM,q}}i_{SM,q}(t)\\ &-\frac{\omega_b r_{1q}\left(l_{22q}l_{aq} + l_{22q}l_l - {l_{aq}}^2\right)}{l_{SM,q}}i_{1q}(t) + \frac{l_{aq}\omega_b l_l r_{2q}}{l_{SM,q}}i_{2q}(t)\end{aligned} \tag{B.9}$$

$$\begin{aligned}\frac{\mathrm{d}}{\mathrm{d}t}i_{2q}(t) = &-\frac{\omega_b l_{aq}(l_{11q}-l_{aq})}{l_{SM,q}}v_{SM,q}(t) - \frac{\omega_b l_{aq}(l_{ad}+l_l)(l_{11q}-l_{aq})}{l_{SM,q}}\omega_{SM}(t)i_{SM,d}(t)\\ &-\frac{\omega_b l_{aq} r_a (l_{11q}-l_{aq})}{l_{SM,q}}i_{SM,q}(t) + \frac{\omega_b l_{ad} l_{aq}(l_{11q}-l_{aq})}{l_{SM,q}}\omega_{SM}(t)i_{fd}(t)\\ &+\frac{\omega_b l_{ad} l_{aq}(l_{11q}-l_{aq})}{l_{SM,q}}\omega_{SM}(t)i_{1d}(t) + \frac{\omega_b l_{aq} l_l r_{1q}}{l_{SM,q}}i_{1q}(t)\\ &-\frac{\omega_b r_{2q}\left(l_{11q}l_{aq} + l_{11q}l_l - {l_{aq}}^2\right)}{l_{SM,q}}i_{2q}(t)\end{aligned} \tag{B.10}$$

$$\begin{aligned}\frac{\mathrm{d}}{\mathrm{d}t}\omega_{SM}(t) \approx &\frac{(l_{ad}-l_{aq})}{T_{SM}}i_{SM,q}(t)i_{SM,d}(t) + \frac{l_{aq}}{T_{SM}}i_{1q}(t)i_{SM,d}(t)\\ &+\frac{l_{aq}}{T_{SM}}i_{2q}(t)i_{SM,d}(t) - \frac{l_{ad}}{T_{SM}}i_{fd}(t)i_{SM,q}(t) - \frac{l_{ad}}{T_{SM}}i_{1d}(t)i_{SM,q}(t)\\ &-\frac{k_{d,SM}}{T_{SM}}\omega_{SM}(t) + \frac{1}{T_{SM}}\frac{p_{m,SM}(t)}{\omega_{SM}(t)} + \frac{k_{d,SM}}{T_{SM}}\omega_g(t)\end{aligned} \tag{B.11}$$

$$\frac{\mathrm{d}}{\mathrm{d}t}\delta\theta_{SM}(t) = \omega_b\omega_{SM}(t) - \omega_b\omega_g(t) \tag{B.12}$$

$$\frac{\mathrm{d}}{\mathrm{d}t}p_{m,SM}(t) = -\frac{k_{\omega,SM}}{T_{gt}}\omega_{SM}(t) - \frac{1}{T_{gt}}p_{m,SM}(t) + \frac{1}{T_{gt}}p^*_{SM}(t) + \frac{k_{\omega,SM}}{T_{gt}}\omega^*_{SM}(t) \quad \text{(B.13)}$$

$$\frac{\mathrm{d}}{\mathrm{d}t}q_{m,SM}(t) = -\omega_{f,SM}v_{SM,d}(t)i_{SM,q}(t) + \omega_{f,SM}v_{SM,q}(t)i_{SM,d}(t) - \omega_{f,SM}q_{m,SM}(t) \quad \text{(B.14)}$$

$$\frac{\mathrm{d}}{\mathrm{d}t}\zeta(t) = -\sqrt{v^2_{SM,d}(t) + v^2_{SM,q}(t)} - k_{q,SM}q_{m,SM}(t) + k_{q,SM}q^*_{SM}(t) + \hat{v}^*_{SM}(t) \quad \text{(B.15)}$$

$$\begin{aligned}\frac{\mathrm{d}}{\mathrm{d}t}v_{fd}(t) = &-\frac{k_{p,ex}}{T_{ex}}\sqrt{v^2_{SM,d}(t) + v^2_{SM,q}(t)} - \frac{k_{p,ex}k_{q,SM}}{T_{ex}}q_{m,SM}(t) \\ &+ \frac{k_{i,ex}}{T_{ex}}\zeta(t) - \frac{1}{T_{ex}}v_{fd}(t) + \frac{k_{p,ex}k_{q,SM}}{T_{ex}}q^*_{SM}(t) + \frac{k_{p,ex}}{T_{ex}}\hat{v}^*_{SM}(t)\end{aligned} \quad \text{(B.16)}$$

B.2 Small-signal model

By linearisation of the nonlinear model (B.1)-(B.16), the small-signal state-space model has been derived in Maple, with the form given by (B.17), where $\mathbf{x}_{SMg}(t)$ is state vector (B.18), $\mathbf{u}_{SMg}$(t) is the input vector (B.19), $\mathbf{A}_{SMg}$ is the state (system, dynamic) matrix, $\mathbf{B}_{SMg}(t)$ is the input matrix (B.21) and the prefix Δ indicates small-signal deviations around the steady-state operating point, $t = 0$. For convenience of notation, $\mathbf{A}_{SMg}$ is expressed through 4 sub-matrices (B.22)-(B.25), according to (B.20).

$$\mathbf{\Delta}\dot{\mathbf{x}}_{SMg}(t) \doteq \frac{\mathrm{d}}{\mathrm{d}t}\mathbf{\Delta}\mathbf{x}_{SMg}(t) = \mathbf{A}_{SMg}\mathbf{\Delta}\mathbf{x}_{SMg}(t) + \mathbf{B}_{SMg}\mathbf{\Delta}\mathbf{u}_{SMg}(t) \quad \text{(B.17)}$$

$$\begin{aligned}\mathbf{x}_{SM}(t) \doteq [&v_{SM,d}(t)\ v_{SM,q}(t)\ i_{o,SM,d}(t)\ i_{o,SM,q}(t)\ \cdots \\ &\cdots\ i_{SM,d}(t)\ i_{SM,q}(t)\ i_{fd}(t)\ i_{1d}(t)\ i_{1q}(t)\ i_{2q}(t)\ \cdots \\ &\cdots\ \omega_{SM}(t)\ \delta\theta_{SM}(t)\ p_{m,SM}(t)\ q_{m,SM}(t)\ \zeta(t)\ v_{fd}(t)]^T\end{aligned} \quad \text{(B.18)}$$

$$\mathbf{u}_{SMg}(t) \doteq [\hat{v}_g(t)\ \omega_g(t)\ p^*_{SM}(t)\ q^*_{SM}(t)\ \omega^*_{SM}(t)\ \hat{v}^*_{SM}(t)]^T \quad \text{(B.19)}$$

$$\begin{bmatrix} \boldsymbol{\Delta}\dot{\mathbf{x}}_{SMg,1}(t) \\ \boldsymbol{\Delta}\dot{\mathbf{x}}_{SMg,2}(t) \\ \boldsymbol{\Delta}\dot{\mathbf{x}}_{SMg,3}(t) \\ \boldsymbol{\Delta}\dot{\mathbf{x}}_{SMg,4}(t) \end{bmatrix} = \begin{bmatrix} \mathbf{A}_{SMg,1} & \mathbf{A}_{SMg,2} & \mathbf{A}_{SMg,3} & \mathbf{A}_{SMg,4} \end{bmatrix} \begin{bmatrix} \boldsymbol{\Delta}\mathbf{x}_{SMg,1}(t) \\ \boldsymbol{\Delta}\mathbf{x}_{SMg,2}(t) \\ \boldsymbol{\Delta}\mathbf{x}_{SMg,3}(t) \\ \boldsymbol{\Delta}\mathbf{x}_{SMg,4}(t) \end{bmatrix} + \mathbf{B}_{SMg}\boldsymbol{\Delta}\mathbf{u}_{SMg}(t) \quad \text{(B.20)}$$

$$\mathbf{B}_{SMg} = \left[\begin{array}{c|c|c|c|c|c} 0 & \omega_b v_{SM,q}(0) & 0 & 0 & 0 & 0 \\ 0 & -\omega_b v_{SM,d}(0) & 0 & 0 & 0 & 0 \\ -\frac{\omega_b \cos[\delta\theta_{SM}(0)]}{l_{mg}} & \omega_b i_{o,SM,q}(0) & 0 & 0 & 0 & 0 \\ \frac{\omega_b \sin[\delta\theta_{SM}(0)]}{l_{mg}} & -\omega_b i_{o,SM,d}(0) & 0 & 0 & 0 & 0 \\ 0 & 0 & 0 & 0 & 0 & 0 \\ 0 & 0 & 0 & 0 & 0 & 0 \\ 0 & 0 & 0 & 0 & 0 & 0 \\ 0 & 0 & 0 & 0 & 0 & 0 \\ 0 & 0 & 0 & 0 & 0 & 0 \\ 0 & 0 & 0 & 0 & 0 & 0 \\ 0 & \frac{k_{d,SM}}{T_{SM}} & 0 & 0 & 0 & 0 \\ 0 & -\omega_b & 0 & 0 & 0 & 0 \\ 0 & 0 & {T_{gt}}^{-1} & 0 & \frac{k_{\omega,SM}}{T_{gt}} & 0 \\ 0 & 0 & 0 & 0 & 0 & 0 \\ 0 & 0 & 0 & k_{q,SM} & 0 & 1 \\ 0 & 0 & 0 & \frac{k_{p,ex}k_{q,SM}}{T_{ex}} & 0 & \frac{k_{p,ex}}{T_{ex}} \end{array}\right] \quad \text{(B.21)}$$

$$\mathbf{A}_{SMg,1} = \left[\begin{array}{c|c|c|c|c} 0 & \omega_b\omega_g(0) & -\frac{\omega_b}{c_{mg}} & 0 & \frac{\omega_b}{c_{mg}} \\ -\omega_b\omega_g(0) & 0 & 0 & -\frac{\omega_b}{c_{mg}} & 0 \\ \frac{\omega_b}{l_{mg}} & 0 & -\frac{r_{mg}\omega_b}{l_{mg}} & \omega_b\omega_g(0) & 0 \\ 0 & \frac{\omega_b}{l_{mg}} & -\omega_b\omega_g(0) & -\frac{r_{mg}\omega_b}{l_{mg}} & 0 \\ \frac{\omega_b\left(l_{11d}l_{ffd}-{l_{f1d}}^2\right)}{l_{SM,d}} & 0 & 0 & 0 & \frac{\omega_b r_a\left(l_{11d}l_{ffd}-{l_{f1d}}^2\right)}{l_{SM,d}} \\ 0 & -\frac{\left(l_{11q}l_{22q}-{l_{aq}}^2\right)\omega_b}{l_{SM,q}} & 0 & 0 & -\frac{(l_{ad}+l_l)\left(l_{11q}l_{22q}-{l_{aq}}^2\right)\omega_b\omega_{SM}(0)}{l_{SM,q}} \\ \frac{\omega_b l_{ad}\left(l_{11d}-l_{f1d}\right)}{l_{SM,d}} & 0 & 0 & 0 & \frac{l_{ad}r_a\left(l_{11d}-l_{f1d}\right)\omega_b}{l_{SM,d}} \\ -\frac{\omega_b l_{ad}\left(l_{f1d}-l_{ffd}\right)}{l_{SM,d}} & 0 & 0 & 0 & -\frac{\omega_b l_{ad}r_a\left(l_{f1d}-l_{ffd}\right)}{l_{SM,d}} \\ 0 & -\frac{\omega_b l_{aq}(l_{22q}-l_{aq})}{l_{SM,q}} & 0 & 0 & -\frac{\omega_b l_{aq}(l_{ad}+l_l)(l_{22q}-l_{aq})\omega_{SM}(0)}{l_{SM,q}} \\ 0 & -\frac{\omega_b l_{aq}(l_{11q}-l_{aq})}{l_{SM,q}} & 0 & 0 & -\frac{\omega_b l_{aq}(l_{ad}+l_l)(l_{11q}-l_{aq})\omega_{SM}(0)}{l_{SM,q}} \\ 0 & 0 & 0 & 0 & \frac{l_{ad}i_{SM,q}(0)-l_{aq}i_{SM,q}(0)+l_{aq}i_{1q}(0)+l_{aq}i_{2q}(0)}{T_{SM}} \\ 0 & 0 & 0 & 0 & 0 \\ 0 & 0 & 0 & 0 & 0 \\ -\omega_{f,SM}i_{SM,q}(0) & \omega_{f,SM}i_{SM,d}(0) & 0 & 0 & \omega_{f,SM}v_{SM,q}(0) \\ -\frac{v_{SM,d}(0)}{\sqrt{v_{SM,d}^2(0)+v_{SM,q}^2(0)}} & -\frac{v_{SM,q}(0)}{\sqrt{v_{SM,d}^2(0)+v_{SM,q}^2(0)}} & 0 & 0 & 0 \\ -\frac{k_{p,ex}v_{SM,d}(0)}{T_{ex}\sqrt{v_{SM,d}^2(0)+v_{SM,q}^2(0)}} & -\frac{k_{p,ex}v_{SM,q}(0)}{T_{ex}\sqrt{v_{SM,d}^2(0)+v_{SM,q}^2(0)}} & 0 & 0 & 0 \end{array}\right] \tag{B.22}$$

$$\mathbf{A}_{SMg,2} = \left[\begin{array}{c|c|c|c} 0 & 0 & 0 & 0 \\ \frac{\omega_b}{c_{mg}} & 0 & 0 & 0 \\ 0 & 0 & 0 & 0 \\ 0 & 0 & 0 & 0 \\ -\frac{\omega_b(l_{aq}+l_l)\left(l_{11d}l_{ffd}-l_{f1d}{}^2\right)\omega_{SM}(0)}{l_{SM,d}} & \frac{\omega_b l_{ad} r_{fd}\left(l_{11d}-l_{f1d}\right)}{l_{SM,d}} & -\frac{\omega_b l_{ad} r_{1d}\left(l_{f1d}-l_{ffd}\right)}{l_{SM,d}} & \frac{\omega_b l_{aq}\left(l_{11d}l_{ffd}-l_{f1d}{}^2\right)\omega_{SM}(0)}{l_{SM,d}} \\ -\frac{r_a\left(l_{11q}l_{22q}-l_{aq}{}^2\right)\omega_b}{l_{SM,q}} & \frac{l_{ad}\left(l_{11q}l_{22q}-l_{aq}{}^2\right)\omega_b\omega_{SM}(0)}{l_{SM,q}} & \frac{l_{ad}\left(l_{11q}l_{22q}-l_{aq}{}^2\right)\omega_b\omega_{SM}(0)}{l_{SM,q}} & -\frac{l_{aq} r_{1q}(l_{22q}-l_{aq})\omega_b}{l_{SM,q}} \\ -\frac{l_{ad}(l_{aq}+l_l)\left(l_{11d}-l_{f1d}\right)\omega_b\omega_{SM}(0)}{l_{SM,d}} & \frac{r_{fd}\left(l_{11d}l_{ad}+l_{11d}l_l-l_{ad}{}^2\right)\omega_b}{l_{SM,d}} & \frac{r_{1d}\left(l_{ad}{}^2-l_{ad}l_{f1d}-l_{f1d}l_l\right)\omega_b}{l_{SM,d}} & \frac{l_{ad}l_{aq}\left(l_{11d}-l_{f1d}\right)\omega_b\omega_{SM}(0)}{l_{SM,d}} \\ \frac{\omega_b l_{ad}\left(l_{f1d}-l_{ffd}\right)(l_{aq}+l_l)\omega_{SM}(0)}{l_{SM,d}} & \frac{\omega_b r_{fd}\left(l_{ad}{}^2-l_{ad}l_{f1d}-l_{f1d}l_l\right)}{l_{SM,d}} & -\frac{\omega_b r_{1d}\left(l_{ad}{}^2-l_{ffd}l_{ad}-l_{ffd}l_l\right)}{l_{SM,d}} & -\frac{\omega_b l_{ad}l_{aq}\left(l_{f1d}-l_{ffd}\right)\omega_{SM}(0)}{l_{SM,d}} \\ -\frac{\omega_b l_{aq} r_a(l_{22q}-l_{aq})}{l_{SM,q}} & \frac{\omega_b l_{ad}l_{aq}(l_{22q}-l_{aq})\omega_{SM}(0)}{l_{SM,q}} & \frac{\omega_b l_{ad}l_{aq}(l_{22q}-l_{aq})\omega_{SM}(0)}{l_{SM,q}} & -\frac{\omega_b r_{1q}\left(l_{22q}l_{aq}+l_{22q}l_l-l_{aq}{}^2\right)}{l_{SM,q}} \\ -\frac{\omega_b l_{aq} r_a(l_{11q}-l_{aq})}{l_{SM,q}} & \frac{\omega_b l_{ad}l_{aq}(l_{11q}-l_{aq})\omega_{SM}(0)}{l_{SM,q}} & \frac{\omega_b l_{ad}l_{aq}(l_{11q}-l_{aq})\omega_{SM}(0)}{l_{SM,q}} & \frac{\omega_b l_{aq}l_l r_{1q}}{l_{SM,q}} \\ -\frac{-l_{ad}i_{SM,d}(0)+l_{aq}i_{SM,d}(0)+l_{ad}i_{fd}(0)+l_{ad}i_{1d}(0)}{T_{SM}} & -\frac{l_{ad}i_{SM,q}(0)}{T_{SM}} & -\frac{l_{ad}i_{SM,q}(0)}{T_{SM}} & \frac{l_{aq}i_{SM,d}(0)}{T_{SM}} \\ 0 & 0 & 0 & 0 \\ 0 & 0 & 0 & 0 \\ -\omega_{f,SM}v_{SM,d}(0) & 0 & 0 & 0 \\ 0 & 0 & 0 & 0 \\ 0 & 0 & 0 & 0 \end{array}\right] \tag{B.23}$$

$$\mathbf{A}_{SMg,3} = \left[\begin{array}{c|c|c|c} 0 & 0 & 0 & 0 \\ \hline 0 & 0 & 0 & 0 \\ \hline 0 & 0 & \frac{\omega_b \sin\left[\delta\theta_{SM}(0)\right]\hat{v}_g(0)}{l_{mg}} & 0 \\ \hline 0 & 0 & \frac{\omega_b \cos\left[\delta\theta_{SM}(0)\right]\hat{v}_g(0)}{l_{mg}} & 0 \\ \hline \frac{\omega_b l_{aq}\left(l_{11d}l_{ffd}-{l_{f1d}}^2\right)\omega_{SM}(0)}{l_{SM,d}} & \frac{\omega_b\left(l_{11d}l_{ffd}-{l_{f1d}}^2\right)\left[-l_{aq}i_{SM,q}(0)-l_l i_{SM,q}(0)+l_{aq}i_{1q}(0)+l_{aq}i_{2q}(0)\right]}{l_{SM,d}} & 0 & 0 \\ \hline -\frac{l_{aq}r_{2q}(l_{11q}-l_{aq})\omega_b}{l_{SM,q}} & \frac{\left(l_{11q}l_{22q}-{l_{aq}}^2\right)\omega_b\left[-l_{ad}i_{SM,d}(0)-l_l i_{SM,d}(0)+l_{ad}i_{fd}(0)+l_{ad}i_{1d}(0)\right]}{l_{SM,q}} & 0 & 0 \\ \hline \frac{l_{ad}l_{aq}\left(l_{11d}-l_{f1d}\right)\omega_b\omega_{SM}(0)}{l_{SM,d}} & \frac{\omega_b l_{ad}\left(l_{11d}-l_{f1d}\right)\left[-l_{aq}i_{SM,q}(0)-l_l i_{SM,q}(0)+l_{aq}i_{1q}(0)+l_{aq}i_{2q}(0)\right]}{l_{SM,d}} & 0 & 0 \\ \hline -\frac{\omega_b l_{ad}l_{aq}\left(l_{f1d}-l_{ffd}\right)\omega_{SM}(0)}{l_{SM,d}} & -\frac{\omega_b l_{ad}\left(l_{f1d}-l_{ffd}\right)\left[-l_{aq}i_{SM,q}(0)-l_l i_{SM,q}(0)+l_{aq}i_{1q}(0)+l_{aq}i_{2q}(0)\right]}{l_{SM,d}} & 0 & 0 \\ \hline \frac{\omega_b l_{aq}l_l r_{2q}}{l_{SM,q}} & \frac{\omega_b l_{aq}(l_{22q}-l_{aq})\left[-l_{ad}i_{SM,d}(0)-l_l i_{SM,d}(0)+l_{ad}i_{fd}(0)+l_{ad}i_{1d}(0)\right]}{l_{SM,q}} & 0 & 0 \\ \hline -\frac{\omega_b r_{2q}\left(l_{11q}l_{aq}+l_{11q}l_l-{l_{aq}}^2\right)}{l_{SM,q}} & \frac{\omega_b l_{aq}(l_{11q}-l_{aq})\left[-l_{ad}i_{SM,d}(0)-l_l i_{SM,d}(0)+l_{ad}i_{fd}(0)+l_{ad}i_{1d}(0)\right]}{l_{SM,q}} & 0 & 0 \\ \hline \frac{l_{aq}i_{SM,d}(0)}{T_{SM}} & -\frac{k_{d,SM}\omega_{SM}^2(0)+p_{m,SM}(0)}{T_{SM}\omega_{SM}^2(0)} & 0 & \frac{1}{T_{SM}\omega_{SM}(0)} \\ \hline 0 & \omega_b & 0 & 0 \\ \hline 0 & -\frac{k_{\omega,SM}}{T_{gt}} & 0 & -{T_{gt}}^{-1} \\ \hline 0 & 0 & 0 & 0 \\ \hline 0 & 0 & 0 & 0 \\ \hline 0 & 0 & 0 & 0 \end{array}\right] \tag{B.24}$$

$$
\mathbf{A}_{SMg,4} = \left[\begin{array}{c|c|c}
0 & 0 & 0 \\ \hline
0 & 0 & 0 \\ \hline
0 & 0 & 0 \\ \hline
0 & 0 & 0 \\ \hline
0 & 0 & -\frac{\omega_b l_{ad}\left(l_{11d}-l_{f1d}\right)}{l_{SM,d}} \\ \hline
0 & 0 & 0 \\ \hline
0 & 0 & -\frac{\left(l_{11d}l_{ad}+l_{11d}l_l-{l_{ad}}^2\right)\omega_b}{l_{SM,d}} \\ \hline
0 & 0 & -\frac{\omega_b\left({l_{ad}}^2-l_{ad}l_{f1d}-l_{f1d}l_l\right)}{l_{SM,d}} \\ \hline
0 & 0 & 0 \\ \hline
0 & 0 & 0 \\ \hline
0 & 0 & 0 \\ \hline
0 & 0 & 0 \\ \hline
0 & 0 & 0 \\ \hline
0 & 0 & 0 \\ \hline
0 & 0 & 0 \\ \hline
-\omega_{f,SM} & 0 & 0 \\ \hline
-k_{q,SM} & 0 & 0 \\ \hline
-\frac{k_{p,ex}k_{q,SM}}{T_{ex}} & \frac{k_{i,ex}}{T_{ex}} & -{T_{ex}}^{-1}
\end{array}\right] \tag{B.25}
$$